Statistical Shape Analysis of the Human Ear Canal with Application to In-the-Ear Hearing Aid Design

Rasmus R. Paulsen

Kongens Lyngby 2004
IMM-PHD-2004-134

Technical University of Denmark
Informatics and Mathematical Modelling
Building 321, DK-2800 Kongens Lyngby, Denmark
Phone +45 45253351, Fax +45 45882673
reception@imm.dtu.dk
www.imm.dtu.dk

IMM-PHD: ISSN 0909-3192, ISBN 87-88306-23-2

Preface

This thesis has been prepared at the Image Analysis and Computer Graphics group at Informatics and Mathematical Modelling (IMM), the Technical University of Denmark and Oticon Research Center Eriksholm. Furthermore, a large part of the work was done at Institut National de Recherche en Informatique et en Automatique (INRIA), Sophia-Antipolis, France. It is a partial fulfillment of the requirements for the degree of Ph.D. in engineering. The project is the result of a cooperation with Erhvervsforskerudvalget, the Danish Academy of Technical Sciences. The project number is EF915.

The subject of the thesis is statistical shape analysis of the human ear canal with application to the mechanical design of in-the-ear hearing aids. Reading this thesis requires a basic knowledge of image analysis, computer graphics, statistics, optimisation, and linear algebra.

The thesis consists of a report and a collection of four research papers written during the period 2001–2004, and elsewhere published.

Research funding was provided by Erhvervsfremmestyrelsen and the Oticon Foundation.

The project was supervised by Rasmus Larsen (IMM), Søren Laugesen (Oticon), Hervé Delingette (INRIA), and Knut Conradsen (IMM).

Kongens Lyngby, June 2004

Rasmus R. Paulsen

Acknowledgements

This thesis has been prepared at three different locations: Informatics and Mathematical Modelling (IMM) at the Technical University of Denmark, the EPIDAURE group at INRIA, Sophia-Antipolis, France, and Oticon Research Center Eriksholm, Denmark. Hence, I am grateful to a large number of persons for making the last three years, the most fun and interesting part of my academic career.

First, I would like to thank my supervisors Rasmus Larsen (IMM), Søren Laugesen (Eriksholm, Oticon), Hervé Delingette (INRIA), and Knut Conradsen (IMM) for their support and encouragement throughout the project. In addition, Claus Nielsen (Eriksholm, Oticon) deserves special credit for acting as my ear canal supervisor and hearing aid expert.

However, the project would never have been realised without the funding from Erhvervsfremme Styrelsen and the Oticon Foundation. A special thank goes to Claus Elberling (Eriksholm, Oticon) and Knut Conradsen (IMM) for believing in this project, despite the difficult background history.

Thanks to Zenia Lausten, Claus Svendsen, and Jesper Trolle from Oticon A/S for supplying me with data and answering questions on hearing aid production.

Thanks to the past and present members of the Image Analysis and Computer Graphics group at IMM for providing a perfect blend of rewarding discussions and an informal atmosphere. A special thanks to my friends and former colleges Lars Pedersen, Klaus Hilger, and Mikkel Stegmann for reviewing this thesis and many memorable social events. Besides laughing politely of my jokes, Andreas

Bærentzen also reviewed the thesis in great detail.

Furthermore, I enjoyed the time I spent at Eriksholm. It is a privilege to work in a company, where you feel like you are among friends. In addition, my knowledge of good food, Italian wine, and rock-induced hearing loss was vastly expanded.

I am in debt to Nicholas Ayache and the rest of the people at the EPIDAURE group at INRIA, for letting me stay with them. Discovering the beautiful southern France, while working in an excellent academic environment was simply fantastic. Furthermore, my friend and office-mate during the 16 months at INRIA, Mauricio Reyes Aguirre introduced me to the warm hospitality of the local south-Americans.

The Visualization Toolkit (VTK) was used as the basis of all software developed. Thus, it has a great influence on the outcome of the thesis. Thanks to Tim Hutton for several enjoyable meetings and for being my VTK mentor.

My family has supported me in many ways. Especially, my brother and my mother have shared my experience, since we have done our theses simultaneous.

Finally, heartfelt thanks to Maëlle Durey for her love and support during the last year of the thesis and for introducing me to her great family.

Abstract

This thesis is about the statistical shape analysis of the human ear canal with application to the mechanical design of in-the-ear hearing aids.

Initially, it is described how a statistical shape model of the human ear canal is built based on a training set of laser-scanned ear impressions. A thin plate spline based approach creates a dense correspondence between the shapes in training set. In addition, a new flexible, non-rigid registration framework is proposed and used to optimise the correspondence field. The framework is based on Markov Random Field regularisation and is motivated by prior work on image restoration. It is shown how the method significantly improves the shape model.

In the second part of the thesis, the shape model is used in software tools that mimic the skills of the expert hearing aid makers. The first result is that it is possible to learn an algorithm to cut an ear canal in order to produce an optimal in-the-ear hearing aid. Secondly, a framework for component placement using a coupling of stochastic optimisation and the results from the shape model is proposed. It is successfully, used to place the so-called *faceplate* with associated component on in-the-ear hearing aids. In addition, the idea of one-size-fits-most shells is explored.

Resumé

Denne afhandling beskriver brugen af statistisk formanalyse af den menneskelige ørekanal i det mekaniske design af i-øret høreapparater.

Først beskrives det hvordan en statistisk formmodel af den menneskelige ørekanal er lavet på baggrund af et træningssæt af laser-skannede øre aftryk. En *Thin Plate Spline* baseret metode genererer en kompakt korrespondance mellem formerne i træningssættet. Endvidere er en fleksibel, ikke-rigid registreringsmetode foreslået og brugt til at optimere korrespondancefeltet. Metoden er baseret på *Markov Random Field* regularisering og er motiveret af tidligere arbejde vedrørende billedeopretning. Det er vist hvordan metoden signifikant forbedrer formmodellen.

I den anden del af afhandlingen, bruges formmodellen i programmer, der efterligner evnerne hos de bedste af dem der laver høreapparater. Det første resultat er, at det er muligt at lære en algoritme at lægge et snit i en scannet ørekanal for at producere et optimalt i-øret høreapparat. Dernæst, foreslås en metode til placering af komponenter. Metoden bruger en kombination af stokastisk optimering og resultater fra formmodellen. Den er succesfuldt brugt til at placere den såkaldte *faceplate* med komponenter på i-øret høreapparater. Derudover er ideen om en skal af en størrelse og form, som passer de fleste forfulgt.

Papers included in the thesis

[A] Rasmus R. Paulsen, Rasmus Larsen, Søren Laugesen, Claus Nielsen, and Bjarne K. Ersbøll. Building and testing a statistical shape model of the human ear canal. In *Proc. of Medical Image Computing and Computer-Assisted Intervention*, volume 2489 of *Lecture Notes in Computer Science*, pages 373–380. Springer-Verlag, 2002. ([201]).

[B] Rasmus R. Paulsen and Klaus B. Hilger. Shape modelling using Markov random field restoration of point correspondences. In *Proc. of Information Processing in Medical Imaging*, volume 2732 of *Lecture Notes in Computer Science*, pages 1–12. Springer-Verlag, 2003. ([199]).

[C] Rasmus R. Paulsen, Klaus B. Hilger, Rasmus Larsen, and Hervé Delingette Non-Rigid Registration of 3D Surfaces using Markov Random Field Regularisation *Submitted*

[D] Rasmus R. Paulsen, Claus Nielsen, Søren Laugesen, and Rasmus Larsen. Using a shape model in the design of hearing aids. In *Proc. of SPIE – Medical Imaging*, 2004. ([202]).

Additional Papers Produced

[127] K. B. Hilger, R. R. Paulsen, and R. Larsen. Markov random field restoration of point correspondences for active shape modelling. In *Proc. of SPIE – Medical Imaging*, 2004.

[179] R. Larsen, K. B. Hilger, K. Skoglund, S. Darkner, R. R. Paulsen, M. B. Stegmann, B. Lading, H. Thodberg, and H. Eiriksson. Some issues of biological shape modelling with applications. In J. Bigün and T. Gustavsson, editors, *Proc. 13th Scandinavian Conference on Image Analysis*, volume 2759 of *LNCS*, pages 509–519, Gothenburg, Sweden, June 2003. Springer.

[200] R. R. Paulsen, R. Larsen, B. K. Ersbøll, C. Nielsen, and S. Laugesen. Testing for gender related size and shape differences of the human ear canal using statistical methods. In *Proc. Eleventh International Workshop on Matrices and Statistics*, Informatics and Mathematical Modelling, Technical University of Denmark, 2002.

Supervised M. Sc. Theses

[160] Allan R. Kildeby. *Building optimal 3D shape models*, 2002

[115] Peter Graversen. *3-Dimensional Shape Modelling. With Application to Human Ear Canals*, 2004

Contents

CHAPTER 1

Introduction

It is well known that the physical presence of hearing aids can affect observers' attitudes toward the hearing aid wearer. At least that is the experience of certain hearing aid users [153].

Today, the miniaturisation of hearing aid components provides hearing aid users with a variety of choices that can satisfy both their cosmetic and acoustic performance needs. The hearing aid industry has realised, that for the hearing aid user the cosmetics are just as important as acoustic performance [153].

The smallest available hearing aid is a completely-in-the-canal (CIC) hearing aid and it has a number of attractive properties compared to traditional hearing aids. A well-produced CIC is as good as invisible when worn and it has the potential of providing superior acoustic performance [104, 191, 229].

Until very recently, the production of a CIC for a given ear was solely a manual and difficult task and the quality of the finished instrument was dependent on the skill of the operator. Hence, there is a high return rate of CIC instruments that do not meet the expectations of the user.

The production of CIC hearing aids is changing from the traditional manual handcrafting methods to being digital. While the introduction of laser scanning, rapid prototyping, and advanced CAD software has had a tremendous impact on the way CIC instruments are produced, the underlying need of general empirical knowledge and human operator skills has remained relatively unchanged. Consequently, the quality of the finished hearing aid is still dependent on operator skills.

The introduction of digital production methods means that large amounts of digital data are becoming available. The data consists of scanned ear impressions and the associated digitally designed CICs. This type of data was very difficult to obtain before, due to the nature of the processes and the products, and the lack of inexpensive scanning equipment.

Obviously, this opens up for a wealth of new possibilities. Foremost is the idea of learning from experience and using this knowledge in the future CIC production. Hence, one aim of this thesis is to analyse, formalise, and mimic the routines used by the expert operator. Doubtless, the operators have knowledge of the anatomical variation of the human ear canal. Consequently, the initial goal is to develop methods that can analyse and use the anatomical variation of the human ear canal. Luckily, the scanned ear impressions provide an excellent basis for that.

Furthermore, it is becoming increasingly clear, that the mechanical properties of hearing aids can be improved considerably. It is obvious that the space available inside a CIC hearing aid is severely limited. Hence, both the mechanical design of the faceplate and the internal components of the CIC and the placement and orientation of the internal components are critical as to whether it is actually possible to build a CIC for a given ear. Today the aforementioned designs are based on the experience and skills of the mechanical engineers and a general informal knowledge about the anatomy and geometry of the ear.

In the hearing aid industry, it is acknowledged that systematic and accessible knowledge of the geometry of ear canals and the variation thereof potentially could be extremely helpful in the design of CIC faceplates and components. In this respect, accessible means that the geometrical data should be accessible from the CAD software used by the mechanical engineers in the design process.

Finally, it has been known for more than two decades that the ear canal deforms when a person is speaking, chewing, or yawning [195, 196]. This deformation may cause acoustical feedback or physical discomfort to a hearing aid user since the shell is rigid. Again, systematic knowledge of the dynamics of ear canal geometry and tools to apply that knowledge in the mechanical design of hearing aids are greatly in demand.

It is obvious that the systematic description of the shape of the ear canal must be done using statistical methods. In recent years, shape analysis has been used in the description, identification, and segmentation of biological shapes. In shape analysis, the idea is to describe the shape information as being data. The basic idea that changes in biological shape can be described and modelled as a mathematical diffeomorphism was fostered as early as 1917 [246]. The theoretical breakthrough was achieved in 1984 [29, 30, 31], but the relationship between all elements of the shape analysis was not fully understood before the late nineties [61, 83]. The two-dimensional case has been studied in many applications while the three-dimensional (3D) shape analysis is an area under rapid development. It is also obvious that the knowledge and routines used by expert hearing aid designers must be formulated as algorithms, which implies that design rules and criteria should be formulated mathematically.

1.1 Objectives

It is the objective of this thesis to study the feasibility of a statistical shape analysis based approach to improved mechanical design of CIC hearing aids.

Thus, it is not the objective of this project to collect and record data for a true population study. The focus of the project is on the development of prototype tools and the mathematical methods that form the basis of these tools.

In conclusion, this thesis has two goals. The first is to build and test a prototype statistical shape model of the human ear canal. The second is to use this model to develop software tools that imitate the skills of the most accomplished CIC operators.

Finally, we hope that the results obtained in the project can help to improve the general quality of CIC hearing aids and increase the percentage of the population that can be fitted with this attractive hearing aid style.

1.2 Thesis Overview

This thesis consists of two main parts; a part about statistical shape modelling and a part about CIC hearing aid design. Furthermore, four research papers are found in the appendix. The papers present a major part of the work done in this thesis. Consequently, the first part of this thesis is mainly a survey that serves to motivate the choices made in the papers. The papers are self-contained, inevitable resulting in overlaps.

Chapter 2 introduces the background and motivation for this thesis.

Chapter 3 describes the data used in this thesis.

Chapter 4 consists of a commented survey of various shape modelling frameworks.

Chapter 5 discusses the problems in generating correspondence over a set of shapes.

Chapter 6 introduces various algorithms from computer graphics that are used in the component placement framework.

Chapter 7 describes a generic component placement framework. Furthermore, the results of applying this framework to the placement of components in CIC hearing aids are reported.

Chapter 8 contains a description of how to generate a one-size-fits-most shell, an introduction to CIC insertion calculation, and a some ideas regarding automatic quality estimation of CIC hearing aids.

Chapter 9 finalises this thesis with a discussion and a conclusion.

Appendix A describes how the statistical shape model of the human ear canal is built and tested.

Appendix B introduces a Markov Random Field regularisation framework and use it to optimise the shape correspondence.

Appendix C describes how the Markov Random Field framework can be used as a standalone, non-rigid registration algorithm.

Appendix D shows that the shape model can be used to guide the mechanical design of CIC hearing aids by placing a so-called *pure faceplate-plane* in an ear canal.

Appendix E contains descriptions of the software developed as part of this thesis.

1.3 Nomenclature

To ease the reading of this thesis a list of often-used abbreviations and acronyms is given below:

AIC	Akaike's "An information criterion"
AAM	Active Appearance Model
ASM	Active Shape Model
BIC	Bayesian Information Criterion
BTE	Behind-the-ear hearing aid
CAD	Computer Aided Design
CBJ	Cartilage-Bone Junction
CIC	Completely In the Canal hearing aid
GCD	Geometry Constrained Diffusion
ICM	Iterative Conditional Modes
ICP	Iterative Closest Point
ITE	In-The-Ear hearing aid
MAP	Maximum A Posteriori
MDL	Minimum Description Length
ML	Maximum Likelihood
MRF	Markov Random Field
PCA	Principal Component Analysis
PDM	Point Distribution Model
SLA	Stereo Lithography Apparatus
TPS	Thin Plate Spline

Hearing aid specific words:

Expert 1 Claus Nielsen, Oticon Research Center Eriksholm.

Expert 2 Zenia Lausten, Oticon A/S.

Operator The person that makes the hearing aids.

Microphone The device that records the sound.

Telephone or Receiver The loudspeaker that sends the sound into the ear.

Amplifier Receives the signal from the microphone, transforms it, and sends it to the receiver.

Faceplate A plastic disc where the battery compartment, the microphone, and an eventual switch are mounted.

Ventilation Canal Also called the vent. A hearing aid is usually equipped with a vent to ventilate the cavity between the eardrum and the hearing aid or earmold.

Chapter 2

Background

This chapter presents a brief introduction to the anatomical and technological background of the project.

2.1 The Human Ear Canal

The outer ear consists of the pinna formed primarily of cartilage without useful muscles, see Figures 2.1 and 2.2. The deep centre portion of pinna is called the bowl or concha. Cymba concha is the upper part of concha formed by the two folds crus and anti-helix. The rim of the bowl is formed by the anti-helix, crus, tragus, and anti-tragus. About two thirds of the ear canal is cartilaginous and soft, while the inner third is surrounded by the mastoid bone. The soft part contains ear wax glands and is lined with hairs, whereas the bony part of the ear canal is covered by thin skin and is very sore to the touch. An ear canal has two more or less pronounced bends. The first bend is found in the lateral part of the canal near the meatus (opening), while the second bend is placed near the cartilage-bone junction (CBJ). The transition between the first and the second bend occasionally narrows down and this narrow passage is referred to as the isthmus. Finally, the tympanic membrane or eardrum separates the ear canal from the middle ear cavity.

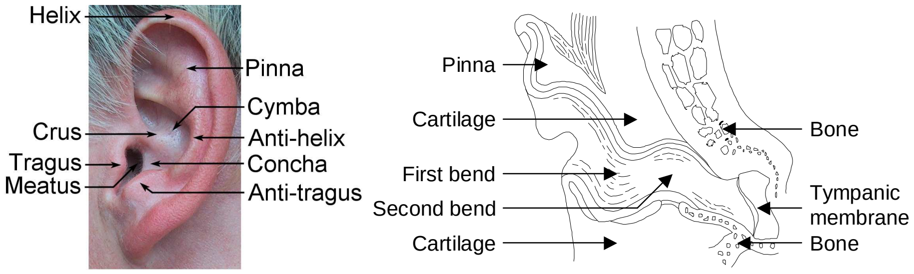

Figure 2.1: Left: Anatomy of the external ear shown on the author's left ear. Right: Medial section of the outer ear and ear canal seen from the top of the head.

The size and shape of the ear and the ear canal has been the subject of some research. An example is the quantification of ear-canal geometry using CT scanning [88]. In another approach, the anatomy is measured using an operating microscope [261]. Stinson uses the geometry of the human ear canal for the prediction of sound-pressure level distribution [234]. The shape variation of ear impressions taken on cadavers is reported in [217]. In addition, ear geometry has an influence on impression taking [227]. Furthermore, Davison generated a realistic looking computer graphics model of the outer ear [78]. Additional descriptions of the anatomy of the human ear canal can be found in [1, 2, 17, 18, 81, 152, 259].

The shape of the ear canal changes when a person is speaking, chewing, or yawning. This has been studied by Oliveira [195, 196] using impressions taken with the jawbone in closed and opened positions. A similar approach is used to map the ear canal movement using data acquired with a reflex-microscope [116].

2.2 Hearing Aids

Hearing aids are characterised as either BTE (behind the ear) or ITE (in the ear). A complete BTE hearing aid consists of a pre-manufactured unit, which contains both transducers and electronics, which are connected by an acoustic tubing system to a custom-made ear mould that delivers the sound output into the ear. For an ITE hearing aid, all components reside in a custom-made shell that sits in the ear of the user; see Figure 2.3 for an example.

ITE hearing aids come in a number of different styles. The smallest of these styles is called CIC (completely in the canal) and it has a number of attrac-

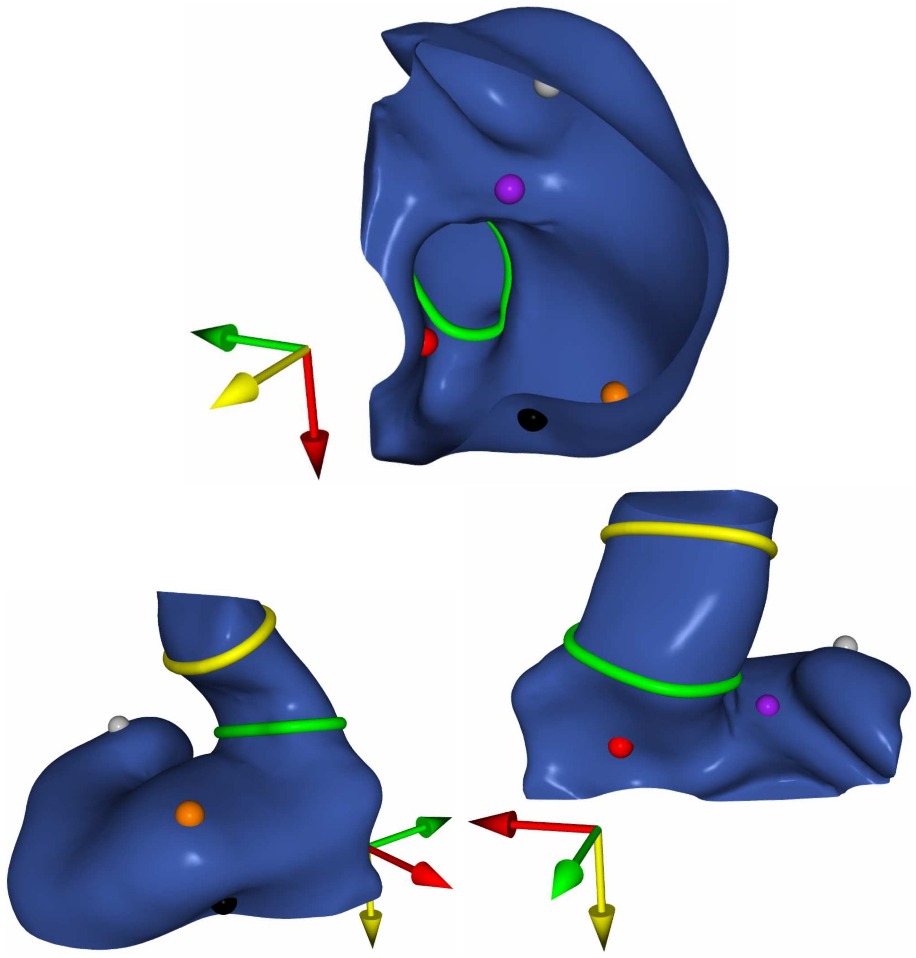

Figure 2.2: The anatomy of the ear shown on the scanned ear impression corresponding to the ear seen in Figure 2.1. The direction out of the ear is shown with a yellow arrow, the forward direction with a green arrow, and downwards with a red arrow. The first (green) and the second (yellow) bend are shown with tubes. The locations of anti-tragus (black), concha (orange), crus (purple), cymba (grey), and tragus (red) are indicated with dots.

(a) Side view (b) Frontal view

Figure 2.3: A CIC hearing aid seen outside and in the author's left ear. The scale is in centimetre.

tive properties. First of all the small size is cosmetically appealing because a well-produced CIC is as good as invisible in-situ [153]. Secondly, the CIC has some acoustic advantages [104, 229]. With the microphone positioned at or even beyond the opening of the ear canal, more of the pinna properties are preserved [54, 117]. Also, the deep insertion of the hearing aid in the ear canal results in a very small residual volume between the hearing aid and the eardrum, which means that a relatively high output level may be produced with a physically small receiver and little electrical power. Finally, the CIC may be able to alleviate the so-called occlusion effect[1] if the CIC shell can be made with a complete seal in the innermost bony portion of the ear canal [105, 161, 191, 205].

---

[1] A hearing aid is a physical object that occludes the ear canal when in-situ. When the hearing aid user speaks, sound propagates through the body and sets the soft part of the ear canal into vibrations. These vibrations generate a sound pressure in the ear canal, which in the open ear condition dissipates out of the ear. However, when the ear is occluded by the hearing aid, a substantial sound pressure is built up in the small cavity between the hearing aid and the tympanic membrane. This increase in own voice sound pressure is termed the occlusion effect. The occlusion effect is often very annoying to the user of the hearing aid.

2.3 The Traditional CIC Hearing Aid Production

The traditional CIC hearing aid production is a manual process. Designs and materials vary, but most CIC instruments are constructed with a faceplate in which the battery compartment and eventually the microphone(s) and switch are mounted from the factory [204]. The principal steps in the production of a CIC instrument are:

1. An ear impression of the hearing-aid user's ear is made by injecting silicone rubber into the ear canal. According to Pirzanski, a well-made ear impression is a true anatomical imprint of the ear canal [206]. A raw impression is seen in Figure 2.4a. Many consider the impression taking as the crucial step in the hearing production [204]. Typically, the operator only sees the impression, not the ear. Hence, it is not possible to produce a well-fitting CIC from a bad impression. Inexperience and sloppy workmanship are the typical causes of bad impressions.

2. The impression is cut and ground to have the correct size and shape for a CIC hearing aid, see Figures 2.4b and 2.4c. Furthermore, voids and artefacts are removed.

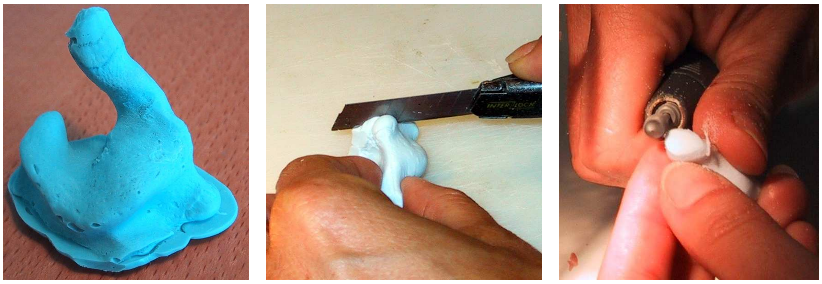
(a) (b) (c)

Figure 2.4: The impression is cut and ground.

3. A gel-form is produced from the cut impression as seen in Figure 2.5a. It is crucial that the gel-form is well-made. An overheated gel-form tends to shrink, causing the final CIC to be to big.

4. The shell is cast by pouring liquid acrylic into the gel-form and hardening it using ultra-violet light, see Figures 2.5b, 2.5c, and 2.5d.

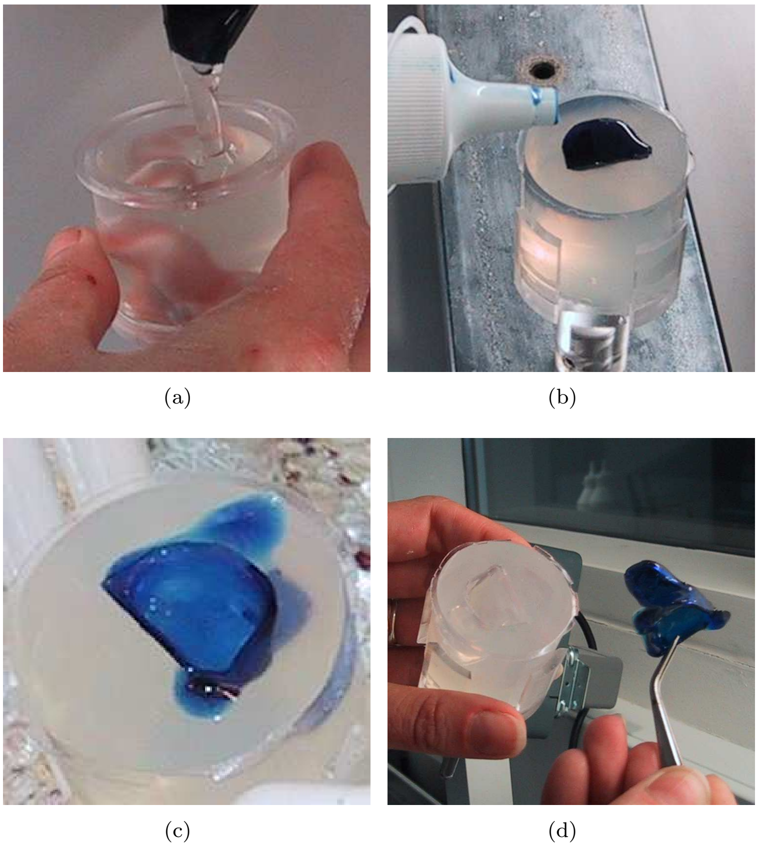
(a) (b) (c) (d)

Figure 2.5: The shell is cast in a hard acrylic material.

5. The shell is ground down to the desired size, see Figure 2.6a. During the processing, the shell is checked against the faceplate as seen in Figure 2.6b. Furthermore, the fit and appearance of the shell is tested in a cast replica of the ear produced from the uncut impression, see Figure 2.6c.

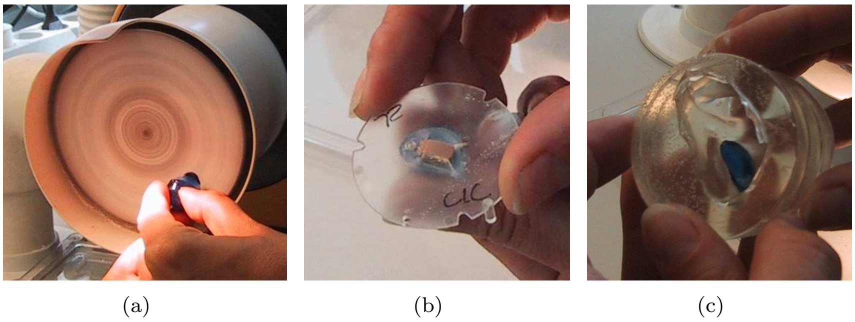
(a) (b) (c)

Figure 2.6: The shell is ground.

6. The internal components of the hearing aid: the receiver, the amplifier, and the ventilation canal are positioned inside the shell. The receiver is installed loosely in the shell by means of a rubber sound tube. All components require adjustment to isolate them acoustically as much as possible. The installation of the ventilation canal can be seen in Figure 2.7a.
7. The shell is glued together with the faceplate and the excess material is trimmed away as seen in Figure 2.7b.
8. Finally, the surface of the hearing aid is polished, see Figure 2.7c.

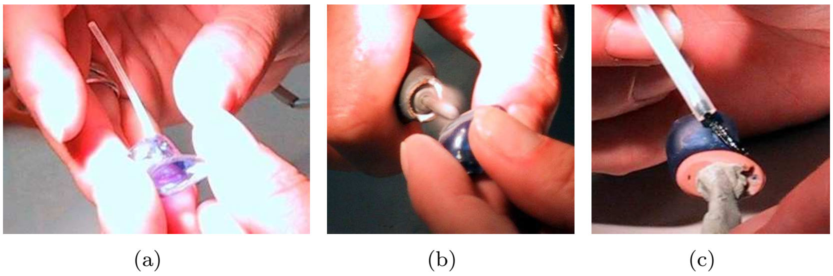
(a) (b) (c)

Figure 2.7: Components are installed and the shell is polished.

As seen, all these processes are done by hand. Obviously, it requires training and skills to produce a CIC hearing aid of high quality. Furthermore, a CIC hearing aid is expensive due to the amount of manual labour involved in the production.

2.4 The Future of CIC Hearing Aid Production

A huge leap in the production technology has occurred during the last two years. This is mainly due to the appearance of sophisticated laser scanners and several commercial packages for the modelling of hearing aids. The steps in the new hearing aid production are explained in the following.

Scanning

Obviously, the geometry of the hearing aid user's ear is still needed. Currently, the geometry is captured by using the traditional impression taking. A high precision 3D replica of the impression is made by a laser scanner. Using one laser and two cameras, the scanner seen in Figure 2.8 generates a 3D model of the impression consisting of approximately 200.000 surface points. In addition, the scanner software generates a triangulated surface from the scanned point cloud.

Modelling

When the scanner has produced a 3D representation of the ear canal, the modelling of the hearing aid can commence.

It is obvious that the modelling process used in the CAD software is adopted from the traditional procedure reviewed in the previous section. The first step is the removal of artefacts and smoothing of the scanned ear impression. This is the digital equivalent of the impression grounding. Furthermore, a shell is created by adding a thickness to the scanning. When the shell is cleaned, the end of the shell is rounded and an appropriate tip is created. The ventilation channel is then created and placed in the shell by the operator. The next step is the placement of electronics. Here the components, represented as 3D models, are placed in the shell. Afterwards, the operator places the faceplate. The shell is then finished and can be visualised in the original ear impression. Finally, the deviations between the finished CIC and the ear canal can be visually examined. More details can be found at the manufacturer's website [254].

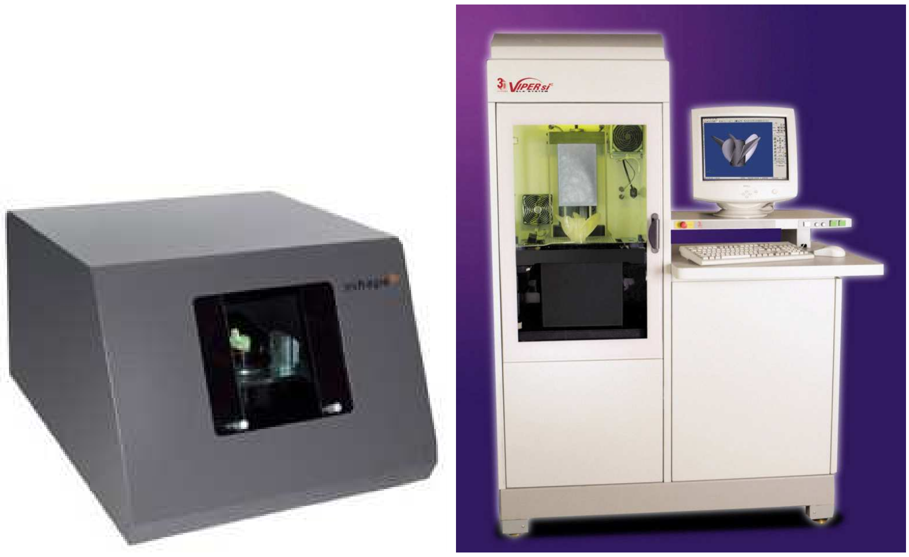

Figure 2.8: To the left a 3Shape S-200 3D Scanner and to the right a 3D Systems Viper Si2 stereo-lithography printer.

Rapid Prototyping

A physical equivalent of a 3D computer model can be build using a rapid prototyping machine. Rapid prototyping machines can produce models in a number of different ways. One example is stereo-lithography (SLA), where a laser beam hardens a liquid monomer (Epoxy), one coating at a time [255]. An SLA machine is seen in Figure 2.8.

A rapid prototyping machine accepts data in the form of 3D volumes defined by triangulated surfaces. For each new coating, the machine calculates a slice of the volume based on the surface, which must therefore be without holes, gaps, and overlaps. A mathematical 2D surface embedded in a 3D space does not have a thickness and can therefore not be printed on a rapid prototyping machine. The process of adding a thickness to a 3D surface is in this context called *shelling*.

Currently, the modelled shells are printed on the SLA machine, while the faceplates are mounted and processed the traditional way. The printer accepts between 80 and 100 shells at a time, with a total production time between five and ten hours.

2.5 Discussion

Switching production methods requires careful consideration and re-education of entire groups of employees. However, many people believe that the advantages of digital production techniques outweigh the inherent organisational changes. Some advantages of the current approach to digital hearing aid production are [254]:

- Improved and consistent quality. The shells produced by the digital system replicate the geometry of the ear more closely than manually produced shells. Furthermore, some of the steps that traditionally required operator-skills have been removed.
- Reduced manual production time.
- Less dependent on human interaction.
- Automated storage and handling of hearing aid user profiles.
- It is easy to remake damaged or lost hearing aids.
- Less remakes. A remake is when the hearing aid user is not satisfied and a new hearing aid is produced for free.

However, hearing aids produced with the new technique suffer from some of the same problems as the traditional shells, for example acoustic feedback and lack of secure fit. We believe this is caused by the considerable variation in the quality of ear impressions and the continued dependence on skilled operators. Currently, the digital design systems are just clever replica of the manual production methodology. Finally, knowledge of the static and dynamic shape variation of the ear canal is not incorporated in the systems.

Part I

Statistical Shape Analysis of the Human Ear Canal

CHAPTER 3

Data

The data initially available for this project consisted of laser scans of 260 ear impressions. The used laser scanner was a prototype laser scanner developed as a part of a master thesis project at DTU [19]. An ear impression and the corresponding laser scan can be seen in Figure 3.1.

Laser scanning produces points that are a sampling of the surface with an arbitrary sampling density. These points can therefore not be regarded as landmarks that can be used in a shape analysis.

Shape analysis is usually based on a set of defined landmarks that are either anatomically defined or based on mathematical properties of the surface. To facilitate the definition of mathematical landmarks or the annotation of anatomical landmarks it is important to reconstruct the surface that the points from the laser scanner represent. When the surface is reconstructed, it is possible to resample it allowing interpolation of points at arbitrary surface co-ordinates. Furthermore, the surface representation is normally needed in order to calculate the differential properties of the sampled surface. Further details on landmark placement and selection can be found in Chapter 5.

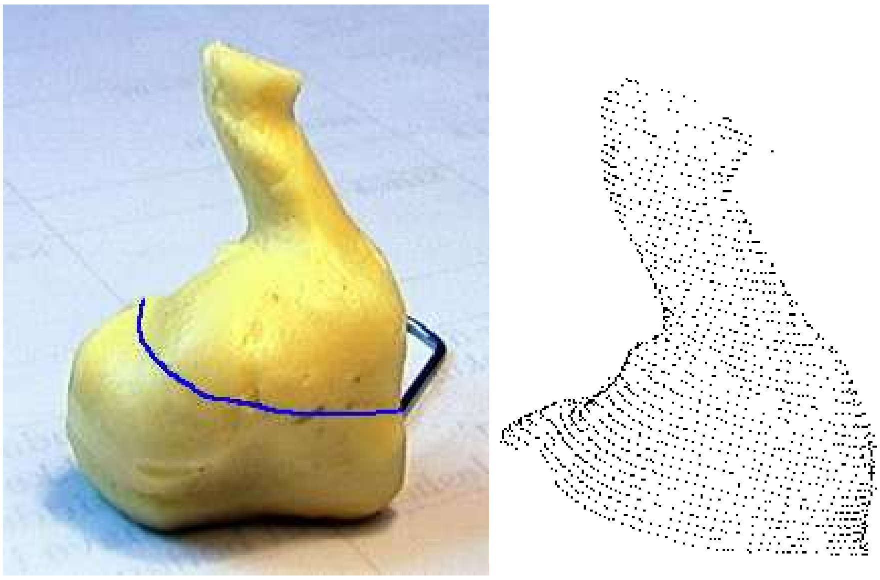

Figure 3.1: An ear impression and the corresponding point cloud. For clarity, only the points on the visible part of the surface are shown. The line on the ear impression corresponds to the lowest samples of the point cloud.

3.1 Surface Reconstruction

The point data from the scanner contains some noise and some outliers. We have developed a simple routine that removes the worst outliers based on neighbour statistics and thereby makes the point cloud better suited for surface reconstruction.

Surface reconstruction from unorganised points has been an active research area for the last decade. Hugues Hoppe developed one of the earliest techniques in 1994 [131]. It is based on a signed 3D-distance transformation of the point cloud. Initially, the point cloud is locally approximated by planes. Hence, the result of the distance transformation is a voxel volume where the value in each voxel is the distance to the nearest plane. Finally, the surface is reconstructed by extracting the zero-value contour of the voxel set. A standard method to perform this contouring is the marching cubes algorithm [183].

In marching cubes, the basic notion is that a cube is defined by the values of the voxels at the eight corners of the cube. If one or more voxels of a cube have values less than the specified value, and one or more have values greater than this value, the cube must contribute some component of the iso-surface. By determining which edges of the cube are intersected by the iso-surface, triangular patches that divide the cube between regions within the iso-surface and regions outside can be created. Connecting the patches from all cubes on the iso-surface boundary makes the surface.

The method has been tested on a number of scanned ear impressions and the results have been evaluated. The reconstructed surface has a very high number of polygons since the number of polygons produced by the marching cubes algorithm is directly related to the sampling resolution of the voxel set used in the distance transformation. The marching cubes algorithm uses no prior knowledge of the surface and therefore no guaranteed geometrical properties of the reconstructed surface are offered. It is observed that the method is sensitive to noise and outliers, which can cause unnatural artefacts in the reconstructed surface. Standard mesh decimation algorithms can be used to reduce the polygon count of the mesh [220], but we experienced that this often resulted in meshes with highly irregular polygons. For rendering purposes, this is not a problem, but for shape analysis and especially collision detection, a more even polygonisation is preferable.

An alternative way of reconstructing surfaces is based on the 3D Delaunay triangulation of the input points. Amenta et al. have developed a novel and sophisticated method called the Power Crust [3, 4]. It is based on the medial axis approximation given by a pruned Voronoi diagram called the power diagram. The Voronoi diagram is computed using the Delaunay triangulation. Given a set of sample points from the boundary of a three-dimensional object, the Power Crust produces a mesh representing the original surface and an approximation to the medial axis of the solid bounded by the points. When the sampling is sufficiently dense, the Power Crust is guaranteed to produce a geometrically and topologically correct approximation to the surface.

The Power Crust has been applied to a number of scanned ear impressions and the reconstructed surfaces have been evaluated. Compared to Hoppe's method the Power Crust surfaces appear better formed and have no artefacts as seen in Figure 3.2. The surface is flat shaded in the Figure to visualise the triangulation. Calculating the normals and using Gouraud shading will give the surface a smooth appearance [99].

Other groups are also working on surface reconstruction from unorganised points. A very high profile project is The Digital Michelangelo Project at Stanford University, where several methods have been developed and used. These methods are mostly aimed at merging data from several views and at being able to manipulate datasets with billions of polygons [181]. A new and promising technique is based on Radial Basis Functions [49, 50]. This method is reported to be able

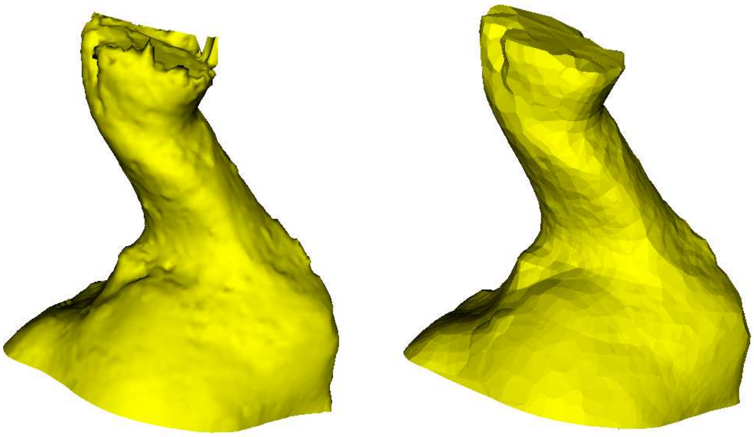

Figure 3.2: To the left a surface reconstructed with Hoppe's method is seen. The surface seen the right side is reconstructed with the Power Crust. It is seen that the surface on the left has some artefacts at the top.

to handle noise data very well. In addition, the level set method [222] has been used as the basis for surface reconstruction [263].

As described in Section 2.4, new and much better scanning equipment has become available during the project, thus reducing the need for advanced surface reconstruction techniques. However, the medial sheet calculated by the Power Crust algorithm plays an important role in the collision detection and path finding algorithms used in the second part of this project. In summary, the surfaces produced by the Power Crust algorithm have been used in this thesis.

A comparison between a scan taken with the original scanner and a modern scanner can be seen in Figures 3.3 and 3.4. The two meshes are first rigidly aligned using the Iterative Closest Point algorithm [25, 262]. Secondly, the difference is calculated by for each vertex in one shape finding the distance to the closest point on the surface on the other shape. It is seen that only a small part of the ear was captured with the first scanner. This area is the most important though. Some deviations exist where the shapes have high curvature. This is probably due to the noise and the surface reconstruction. Nevertheless, we believe that the data captured with the original scanner has sufficient quality for the proof-of-concept that is the goal of this project. Obviously, the modern scanner will be used for future population studies.

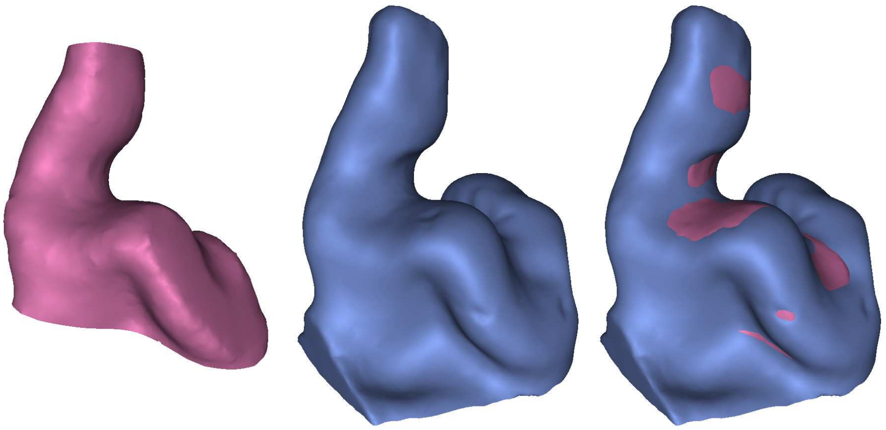

Figure 3.3: From left to right: Original scan, scan with a modern scanner, the two surfaces rigidly aligned.

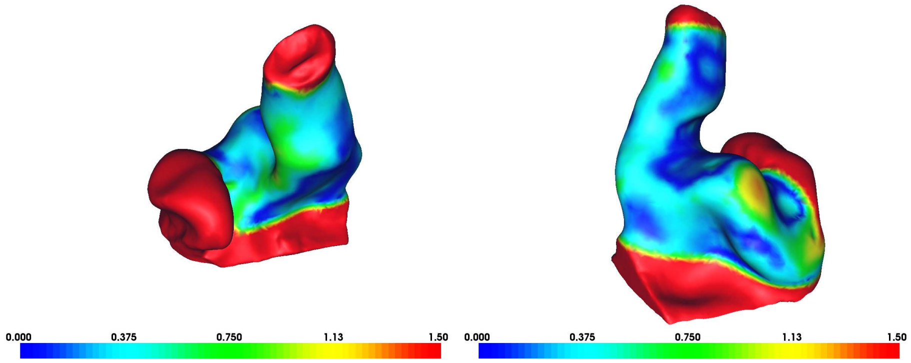

Figure 3.4: The difference between an original scan and a new scan. The distance to the surface of the original scan is calculated for each point in the new scan [mm]. The large red area of the new scan is where the original scanner did not scan the surface.

Chapter 4

Shape Modelling

One goal of this project is to develop data driven methods that can analyse and visualise the anatomical variation of the human ear canal over a population and to be able to use this knowledge in the future design of hearing aids.

We are searching for a method that

- can be applied to 3D surfaces with non-spherical geometry. In this case surface patches that are topologically equivalent to open cylinders,
- can be trained from a set of training shapes,
- has a statistical basis and where the parameters of the model can be used as input to multivariate statistical analysis,
- is suited for the analysis of biological shapes,
- has proven to be implementable.

In the following, various shape model frameworks are discussed and compared to the requirement specification above. The shape model implemented and applied in this thesis is selected on a basis of this survey.

4.1 Shape Models

A popular and commonly used class of models is the *deformable template models*, of which the most well known is the Active Contour Model called *Snakes*. It was introduced by Kass et al. in 1988 [157]. A template model normally consists of an outline defined by landmarks, on which a set of physically related constraints are enforced together with some image related forces. For an overview of deformable models, the reader is referred to the surveys in [27, 96, 150, 151, 187]. However, it does not seem optimal to use deformable models to describe and analyse the shape variation of surfaces in 3D, since they are primarily used for tracking and image searching purposes. Furthermore, this class of models is known to be parameter sensitive, weak on robustness, and often requires operator intervention.

In recent years other methods of representing shapes have appeared, one being the M-Rep model originating from the *University of South Carolina, Chapel Hill* [155, 207, 235, 236, 260]. The shapes are represented using their medial sheets. For each vertex in the medial sheet, a primitive called an atom is defined. The atoms specify, among others, the distance to the surface of the object. Since the medial parameters are not elements of an Euclidean space, standard Gaussian based statistics cannot be directly applied to the analyses of the shape variability. However, recent work on Gaussian distributions on Lie Groups with application to the parameters of the M-Reps [97] seems promising. M-reps have, among others, been used to analyse the morphology of brain structures [109]. Building a complete M-Rep model of a set of training shapes seems to be a very difficult task. Furthermore, we believe that the shape variation found in for example ear canals would induce topology changes in the medial sheet. An example of this is the part of the canal between the first and the second bend, which has an elliptical cross-sectional shape. The axis of this ellipse can be aligned both horizontally and vertically. This causes a flipping of the medial sheet. Examples of medial sheets of ear canals can be seen in Figure 4.1. They have been calculated using the Power Crust algorithm [3, 4]. Further details can be found in Chapter 6. It is not clear how to model these topology changes in a statistical setting. Furthermore, it is not obvious how objects that are not topologically equivalent to spheres should be modelled.

Another parametric surface model that can be used to represent objects of spherical topology is the *spherical harmonics* (SPHARMS) [37, 38, 39, 209]. They have been demonstrated to be able to express shape deformation [159]. It is a smooth and accurate representation based on a basis of spherical harmonics. SPHARMS has been used in the study of the shape of neuro-anatomical structures [108], but it is not suited for modelling the shape of objects that are not topologically equivalent to spheres.

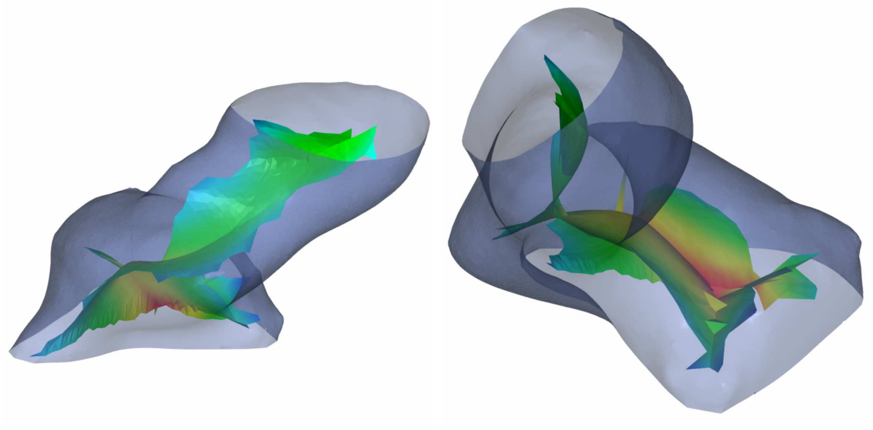

(a) Ear canal A

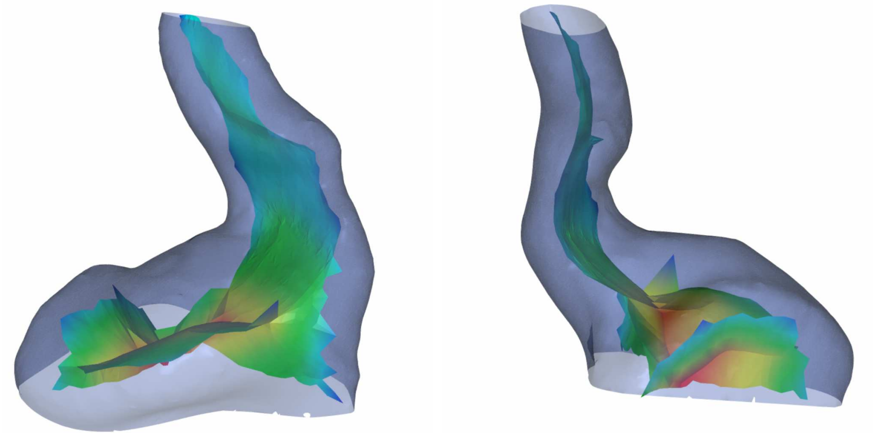

(b) Ear canal B

Figure 4.1: The medial sheet calculated for two different ear canals. The topologies of the two sheets are clearly different. In the middle part of the canal, the sheet is split in three in ear canal A while being a single sheet in ear canal B.

A similar method that supports non-closed surfaces is the Fourier surfaces explored by Staib et al. [230]. For each shape in a training set, the Fourier coefficients are calculated. These coefficients are then modelled over the training set. New shape examples can be synthesised by sampling from the distributions. However, it is not clear how this method can be applied to surface patches where the positions of the borders have no anatomical meaning.

An alternative approach for shape modelling is to generate a physical model of the object, where the variation of the object is calculated based on the physical properties of the tissue. This method has for example been used to model the biomechanical properties of the heart using a volumetric finite element method [221]. The model can be used for segmentation and tracking of time series of for example MRI and SPECT images. It seems that the method is not well suited for analysing the statistical variance of the shape over a population.

Finally, the most appropriate approach to model and analyse the data was found to be the *Active Shape Model* (ASM) approach by Cootes et al. [61]. Initially, this method was derived from the Active Contour model with some additional constraints [62, 66, 69]. Later it was formulated as a complete framework for statistical shape description, synthesis, and recognition [61]. The method has been extended to include multi-resolution searches [70, 71] and a combination with finite element models has been demonstrated [67]. The ASM model deals with contours in 2D and surfaces in 3D, while pixel and voxel values are ignored. The *Active Appearance Model* (AAM) is an extension of the ASM model that includes texture or volumetric grey level information [60, 63, 64, 65, 86]. Modelling 3D voxel intensities requires a very advanced framework and it is first recently that is has proven possible [232]. The AAM framework is not suitable for the ear canal data, since they are pure surfaces with no underlying voxel representation.

The ASM approach has been used in a wide variety of medical applications. A method to build a 3D model of the knee is presented in [98], where a model mesh is warped to each shape in the training set by an octree spline approach. A description of the building of a 3D shape model of the left ventricle of the heart is given in [185] and a 3D model of the spleen and the kidney is described in [168]. The ASM method has also been used in commercial FDA approved applications. An example is found in [245], where a 2D ASM model is used to locate the metacarpal bones in X-rays of the hand. An overview of medical applications can be found in [179].

4.2 Building a Shape Model

An ASM can be built based on a training set of shapes with point correspondences. This means that the points describing the contour or the surface of the training shapes need to be placed on the same locations on all the shapes. Achieving this is a major task in itself and is the topic of Chapter 5.

Due to the excellent online *cook book* by Cootes [58], the implementation, and testing of an ASM framework is relatively straightforward. The method consists of a series of sub-tasks. For each sub-task, there is a choice of methodology bound to the application and the data. These sub-tasks are discussed in the following and the choices made for the analysis of the ear canal data are motivated. The building and testing of the ear canal shape model is described in detail in Appendix A.

For a gentle introduction to the ASM and the associated notation, the reader is referred to these introductory texts [58, 61, 231].

4.2.1 Shape Alignment and Decomposition

The standard method for aligning a training set of shapes represented by homologous points[1] is the Procrustes method [111]. For 2D shapes, an analytical solution exists [83] while for 3D shapes it is usually done in an iterative fashion. The method involves aligning a pair of shapes, for which several methods exist. It has been shown that for *normal* shapes the different alignment algorithms perform equally [87]. If a rigid-body alignment is used, the result is a size-and-shape model and if a similarity-transform is used in the alignment, the model will be a pure shape model [83].

The alignment of the shapes is followed by decomposition of shape variability. An aligned shape is represented as a vector of concatenated coordinates and can therefore be regarded as a point in a 3n-Dimensional space (where n is the number of points on each shape) and a set of shapes as a cloud of points in that space. To be able to synthesise and manipulate shapes it is necessary to parameterise this point cloud in the 3n-D space. A parameterisation should provide a method of moving around the cloud by using only a few parameters. If it is reasonable to assume that the point cloud constitute a hyper-ellipse, the Principal Component Analysis (PCA) known from multivariate statistics can be used to calculate the centre, the axes, and the dimensions of this hyper-ellipse [154]. If the positions of the landmarks can be assumed to follow a

---

[1] Homologous points are points that correspond to the same feature on different shapes.

Gaussian distribution this normally gives a good approximation of the shape point cloud. The region of the space that the point cloud occupies is sometimes called the *Allowable Shape Domain* [61].

In some cases, the hypothesis of the ellipsoid model breaks down. An example with artificial worm shapes can be found in [61]. In that case, alternative approaches to model the point cloud in shape space must be sought. Examples from the literature are the non-linear polynomial point distribution model [228], the non-linear kernel PCA [212], maximal autocorrelation, and maximal noise fractions decomposition [90, 174, 175, 176, 178, 180, 238]. In addition, non-linear Point Distribution Models are treated extensively in [36].

The ellipsoid approximation was found to be efficient in the current project. The evaluation was done by examining the distribution of the PCA parameters. Further details can be found in Appendix A.

4.2.2 Selecting the Number of Parameters

When the shape space has been parameterised, using for example the ellipsoid model from the PCA, the number of important parameters necessary to navigate the shape space needs to be determined.

Obviously, the more parameters, the better fit of the model; the less parameters, the more simple the model will be. Somewhere in between is the optimal number of parameters. To determine this number, there must be a criterion for *optimality*. A large number of criteria exist, ranging from significance tests to graphical procedures. A thorough discussion and testing of the different criteria can be found in [149].

A popular criteria used very often in shape analysis is the proportion of the trace of the covariance matrix that is explained by the principal components in the model. In many applications, the number of components to retain is chosen so they explain 95% of the trace of the covariance matrix. Hence, the corresponding eigenvectors explain 95% of the variation seen in the training data. Jackson strongly advices not to use this method, except for initial explorative data analysis [149]. Suppose that for a model with 20 parameters, the last 15 parameters each explain nearly the same percentage of the trace, and further suppose that the five most important principal components only explain 50% of the trace. Should one keep adding components until the magic number is reached? If so, why should for example component number 17 be excluded while component number 7 is retained, when they explain nearly the same amount of the trace?

An alternative test is the graphical test called the *scree test*, where the eigenvalues of the covariance matrix is plotted against the number of components. A typical scree plot is show in Figure 4.2. The name scree-plot is due to Cattel [51]. The scree is the rubble at the bottom of a cliff. The idea is that the point where the scree starts is located and the number of components is chosen to be at that point. This point is sometimes called an *elbow* [149]. On Figure 4.2 it is not obvious where that point is, probably around mode (component) number 10.

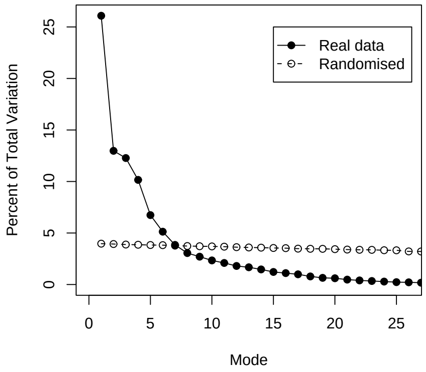

Figure 4.2: A typical scree plot. The scree plot for the same, but randomised data is also shown. The plot is taken from Appendix A.

To avoid the graphical inspection and the inherent operator influence of this approach a group of procedures called *Parallel Analysis* (PA) emerged. In the method of Horn, the eigenvalues are calculated from the same, but randomly scrambled data set and the two scree plots are compared [135]. The number of components is chosen to be where the two lines cross as seen in Figure 4.2. This method has successfully been applied to the ear canal data as explained in Appendix A. Parallel analysis has also been used to truncate the model parameters of an AAM, where the number of components selected where far less than with the *proportion of the trace* method [233]. If the first few roots are so widely separated that plotting can be difficult without losing information about the scree point, the log of the eigenvalues can be plotted instead. This is called a LEV (log-eigenvalue) plot [149] and has been used in parallel analysis.

A simpler method is to retain only the components whose eigenvalues exceed the average of all the eigenvalues. When the PCA is made on correlation matrices, the average root is equal to one, which makes this test very simple.

Moreover, Larsen and Hilger have demonstrated the use of the Bayesian information criterion (BIC) and Akaike's "An information criterion" (AIC) in the selection of model complexity [177, 178].

For a given model the log-likelihood of the data is estimated and penalised using either BIC and AIC. BIC arises from a Bayesian approach to model selection, whereas AIC provides an estimate of a test error curve with a minima at the optimal trade-off between model complexity and performance.

The log-likelihood increases with increasing model complexity, i.e. larger models reconstruct the training data better. In general BIC punishes the log-likelihood harder with increasing model complexity, thus giving preference to simpler models in selection. The optimal balancing of the model complexity and performance depends on whether or not the family of models applied includes the true underlying model.

Furthermore, BIC is regarded as an approximation to the Minimum Description Length despite being derived in an independent manner [123].

As demonstrated in [149] the results of the different methods vary enormously. The choice of method should be based on the application and followed by some kind of *sanity* check.

4.2.3 Multivariate Statistical Analysis

Morphometrics, the multivariate statistics of object shape has advanced greatly over the last decade as described by Bookstein in [34]. Bookstein demonstrates how it is possible to examine group differences of shapes by their outlines [33] and an overview of, and a complete framework for, testing landmark based shape group differences can be found in [34]. In addition, the use of thin plate splines to decompose shape variation is described in [32].

The methods from morphometry can be used to analyse the information contained in the statistical shape models. An example is that it has proven possible to discriminate gender using logistic regression on 2D shape models of human face silhouettes [244] and by regression analysis of the shape space parameters from a full 3D face model [143].

Another example is the analysis of growth. Growth analysis has been performed on human mandibles using a shape model built from the 3D surfaces extracted from CT scans [6, 126] and on human faces captured with a 3D surface scanner [144, 146].

Discriminating between normal or abnormal subjects using shape models is an area that has received much attention in the later years. Examples are the analysis and discrimination of 3D face models of individuals with Noonans [121] and Smith-Magenis syndrome [122]. The characterisation of the shape of neurological structures has also proven to be significant in the analysis of some illnesses [108, 109, 236]. An example is the analysis of the shape of the Corpus Callosum [84].

In this project, it proved possible to perform gender discrimination based on the shape and the size of the ear canals. See Appendix A for details.

4.2.4 Shape Fitting and Recognition

One of the primary abilities of the ASM is the possibility of using it to find and recognise previously unseen shape examples. Using a shape model in the search of 2D structures in images has been widely used. See for example [43, 44, 61]. For 2D image search, ASM is often substituted with the more powerful AAM [58, 60, 63, 64, 65, 68, 86, 231].

Many improvements to the search scheme has been suggested, including multi-scale approaches [70, 71] and ASM with optimal features [110], where in each ASM iteration the optimal landmark displacements are found by locating the optimal features using a nonlinear kNN-classifier. Furthermore, the ASM search can be made more robust against outliers using M-estimators [211].

Fitting a 3D surface shape model to a new example has been done using a combination of the Iterative Closest Point (ICP) algorithm and active shape model searching in [143, 145].

When an ASM has been fitted to a new example shape, it can be used to map features from an atlas to the new example. In this project, a combined ICP/ASM approach resembling the method by Hutton [143, 145] has been used to place faceplates on ear canals as seen in Appendix D. Furthermore, the ASM is used to propagate landmarks to the new ear. These landmarks are, among others, used to calculate paths through the ear canal as demonstrated in Section 6.3.

The shape parameters that describe the new shape can be calculated from the fitted ASM. These parameters can then be used in multivariate classification as explained in Section 4.2.3.

4.3 Evaluating the Quality of a Shape Model

When a shape model of a group of anatomical objects has been built, there is a need for evaluating the quality of the result. An intuitive first approach is the visual validation of the shapes that can be synthesised by the model. In Figure A.2 on page 105 and Figure B.5 on page 120, the major modes of variation of the ear canal shape model are shown. An expert in the anatomy of the ear canal has examined these 3D models and validated that from an anatomical point of view they look plausible. Furthermore, there is no apparent deformation of the structure and no inversions and intersections of the surface. Examples of invalid shape models can be found in for example [73]. In addition to this *sanity* check, measures that are more objective should be computed. Davies [73] and others suggest the following list of optimality criteria for shape models:

Generalisation Ability The capability of the model to represent unseen instances of the class of the object modelled. A model build based on too few examples tends to overfit the data and will not have good generalisation abilities. This ability can be measured by a leave-one-out analysis of the training set, where it is examined how well the model built by the included training shapes approximates the left out object.

Specificity When synthesising artificial shapes by sampling in the learned distribution the results should be similar to the shapes found in the training set. This can be validated by synthesising a range of instances and comparing them to the training set.

Compactness A good model should only need a few parameters to describe the instances in the training set. Furthermore, the variance of the model should be as little as possible. This can be measured by the sum of the eigenvalues of the shape covariance matrix.

These criteria have for example been used by Davies to evaluate the results from the Minimum Description Length (MDL) framework [73]. The MDL method is covered in more in detail in Section 5.2.1.

The above-mentioned criteria do not include one that ensures that each shape in the training set is *well represented*. The landmarks of the shape model constitute a point cloud. In certain cases, there is additional topological information, linking the points in a mesh. To represent an instance of the training data the point cloud should cover the important part of the shape. This is especially relevant when modelling surface patches of larger objects. It seems that a shape model could score very well in the above criteria while at the same time completely ignore an anatomical relevant feature on the shapes in the training set. An example could be a 3D human face model, where the nose would be ignored. To avoid that, we are suggesting an additional performance criterion:

Representation Ability Measures how well the shape model represents each shape in the training set. It can be computed by for each shape in the training set calculating how well the landmark cloud and the associated mesh approximates the target shape. The approximation error is calculated as the average distance from the vertices in the target mesh to the closest points on the approximation surface.

A bad and a more optimal representation of a part of a training shape can be seen in Figure 4.3. This criterion has been used in the evaluation of the MRF method as described in detail in Appendices B and C.

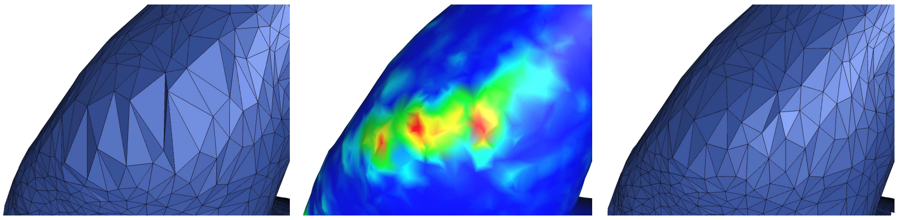
(a) (b) (c)

Figure 4.3: a) The landmark point cloud and the associated mesh do not represent the training shape very well. b) The representation error. c) A better representation of the training shape.

A second quality measure that is used in Appendices B and C is an analysis of the triangular structure of the mesh representing the target shapes. In this case, the mesh structure from a model mesh is applied to all shapes in the training set, and the goal is to keep a good structure of the mesh after the projection to the target shapes. This measure does not measure the quality of the shape model, but tells more about the data used to build the shape model, and in that way provides an indirect quality measure.

The topic of the next chapter is the problem of generating correspondence over the training set. Manual, semi-automatic, and fully automated methods exist. In all cases, the above-mentioned criteria are well suited for validating the quality of the chosen shape correspondence. The generalisation, specificity, and compactness criteria measure the quality of the shape model that results from the set of shapes in correspondence and thus need shape alignment and decomposition to be performed before they can be computed. The representation ability does not need this and is therefore well suited to evaluate pairwise correspondences.

4.4 Discussion

In this chapter, various frameworks and approaches for shape modelling are presented. It is obvious, that no optimal method currently exists. The approach must be chosen based on the application and the available data. In addition, it is advised to adopt an iterative strategy, where the simplest approach is initially tried and later extended if problems arise. An example is the decomposition of shape variance, where the basic Principal Component Analysis should be tried first. However, if the data proves to be insufficiently described by the PCA, more advanced methods should be applied.

This iterative approach was used when the statistical shape model of the ear canal was built. As seen in Appendix A, the simplest approach was often sufficient.

CHAPTER 5

Surface Correspondence

As stated in Chapter 4 the prerequisite for building shape models is shape correspondence. Since manual landmarking is difficult and especially in 3D tedious and error prone, there is a great demand for semi- or full-automatic landmarking and correspondence algorithms. This task is far from easy and is the focus of much research.

This chapter presents a survey of methods used to generate point correspondence. Moreover, some comments on the application of the methods on the ear canal data set are made.

The methods can generally be classified into functional groups. First, there are the manual methods, where each corresponding landmark is placed by an experienced operator. The second group is the semi-automatic methods, where a set of sparse landmarks are placed and from these a dense correspondence is computed. Finally, the most advanced are the fully automated methods, where no prior knowledge is given, and where all landmarks are placed by the algorithm.

The focus is on the semi- and full-automatic methods. These methods can broadly be divided into two groups. The *pairwise* methods where the shapes in the training set are matched two-by-two by optimising a pairwise objective function, and *groupwise* methods, where all the shapes in the training set are matched simultaneous, thus optimising a groupwise objective function [59]. There is not a clear distinction between the two types of methods, since a pairwise method often indirectly optimises a groupwise objective function.

5.1 Pairwise Methods

In a typical pairwise method, a model shape is selected from the training set and then matched to the remaining shapes in the set. Alternatively, the model shape is generated independently or iteratively from the first set of shape matches.

The matching of a model shape to a target shape can be seen as a registration task, where an objective function is optimised. Many registration algorithms are designed to work with voxel data, for example matching MR and CT volumes. An overview of volume registration algorithms can be found in [130, 186]. Less, but still a considerable amount of research has been done on the registration of surfaces. Published methods are ranging from an approach using a combination of superquadrics and spherical harmonics for elastic warping of brain images [247], an algorithm based on matching 3D distance maps [141, 256], a method using surface signatures [257] to a mesh metamorphosis-approach using harmonic mapping [156]. An overview can be found in [14], where it is suggested how to choose the transformation type, the surface features, and the optimisation strategy.

One of the earliest general-purpose surface registration algorithms is the Iterative Closest Point (ICP) algorithm [25, 262]. The ICP algorithm or a variant is a typical choice as a step in a procedure that generates pairwise correspondence. It aligns two shapes by matching points from one shape to the surface of the other, thus generating correspondence between the shapes. This crude and often incorrect correspondence is sometimes used as an initial guess that are later optimised. Furthermore, the ICP algorithm has been extended and used as a basis for more advanced local registration techniques. An example is the extension by Feldmar and Ayache [94, 95], where it is not closest points, but closest *feature vectors* that are sought. Fuzzy extensions to ICP are described in [170] and efficient ICP variants in [214]. In addition, a multi-scale expectation maximisation ICP is described in [114].

Brett and Taylor use a pairwise method to build a 3D model of the cortical sulcal [52]. Initially, a symmetric ICP where the distance measure is weighted by the local geometry of the shapes generates correspondence between the shapes. Secondly, a tree of pairwise matched shapes is built. From this, an average shape is computed and applied to all the shapes in the training set. Finally, a shape model is built from the resulting meshes with dense correspondence. This method has later been extended to use harmonic maps to define a diffeomorphic correspondence between pairs of shapes [42] . In another application, the ICP algorithm is used to register and propagate landmarks on lung surfaces extracted from CT scans [26]. Furthermore, a non-rigid surface registration method, resembling ICP, named Geometry Constrained Diffusion (GCD) has been used to register mandibles in order to analyse the bone growth [5, 6, 7, 8].

An alternative approach is the automated construction of deformation models by Rueckert et al. [213]. Here dense volumetric correspondence is established using a non-rigid registration technique. Thus, the correspondence is found by the maximisation of normalised mutual information. The unusual thing is that the PCA is applied to the dense volumetric deformation field instead of the displacements of the vertices of a surface. However, this method is only applicable to voxel-based data.

Another volumetric approach where landmarks are automatically found on a model shape and propagated to the shapes in the training set is used to build multi-object 3D shape models [101]. In a similar approach, a model shape is automatically fitted to a series of volumetric training images using a deformable model [158]. The set of fitted model shapes is then used to build a shape model of the femur and vertebra.

Face synthesis using a model shape built by creating a one-to-one correspondence to an internal face model has been done [28]. Furthermore, a model shape is used in a pairwise method, where a model of the hip is built and used as a guide for hip operations [89].

A semi-automatic method using a thin plate spline (TPS) warping based on a set of sparse annotated landmarks is found in [184]. A model shape is applied to each shape in the training set. This is followed by a regularisation step where each vertex of the model shape is adapted to the current shape without causing folds. A similar approach is found in [143] with the addition that the method is able to handle surfaces with ill-defined areas. This is done by pruning the model shape so it only includes the vertices that are well defined for all training shapes.

In certain applications, it is desired that the correspondence vector field possess some special properties. It could for example be that the field should constitute a diffeomorphism. This is far from trivial and is the subject of much recent research, for example warping based on Brownian motion [194].

The basic problem with pairwise correspondence methods is that good global properties of the shape model are not guaranteed. However, pairwise methods tend to optimise the global properties indirectly. An example of this can be found in Appendix B, where the compactness of the shape model is increased after a pairwise optimisation and in Appendix C, where the determinant of the covariance matrix indicates a more optimal shape model after optimisation. The properties of the shape model can be evaluated using the criteria described in Section 4.3.

5.1.1 A Landmark and Model Shape Based Approach

In the current project, the data consists of 3D surfaces with non-spherical geometry. In an earlier study, the extremal mesh [242] was calculated for the surfaces of the ear canals and it was realised that it was very difficult to locate stable local features based on differential geometry. Since the goal is to build a shape model and not to invent a new automatic method, we chose a semi-automatic method, where an operator selects a sparse set of pseudo-anatomical landmarks on each ear canal. The method is derived from the methods that use a model shape and thus resembles the methods of Lorenz [184] and Hutton [143]. The landmarks were placed with a custom-made toolkit described in Appendix E.1. A mesh with good properties in terms of triangular regularity and smoothness is selected as a model shape. The set of sparse correspondences are used to warp the model shape to all the shapes in the training set with a TPS warp. Since the TPS transform is only exact for the anatomical landmark locations, the vertices of the warped model shape do not lie on the surface of the target shape. Finally, moving each vertex in the warped model shape to the closest point on the target surface completes the dense correspondence. The method is described in detail in Appendix A.

It was later realised that the initial method suffered from the fact that the *representation* of the shapes in the training set was flawed. In regions of high curvature, the adapted model shape would not cover the target shape in a satisfactory way. This resulted in a representation error where parts of the target shape was not represented very well as seen in for example Figures C.4 on page 140 and C.5 on page 141. The cause of this problem is the non-homogeneous correspondence field generated by the point-to-surface projection technique used in Appendix A. The observation of the ill-represented shapes was the inspiration for the *Representation Ability* criterion presented in Section 4.3.

5.1.2 Markov Random Field Regularisation

A simple way to avoid the non-homogeneousness of the correspondence vector field is to smooth the vector field after the closest point projection. This approach regularise the vector field, but on the other hand completely ignores the surface properties of the model and the target shapes. It turned out that what was started as a simple smoothing method could be formulated in a Markov Random Field (MRF) framework, where surface properties can be incorporated in the model. The details and the results from this method can be found in Appendices B and C. Moreover, a visual interface to the algorithm is described in Appendix E.6.

Using a MRF suffers from a number of difficulties similar to the ones in deformable template models [96]. According to Jain et al. these are [150]: model parameter selection, initialisation, and optimisation. As described in detail in Appendix C these three topics have been treated as following:

Parameter selection The most important parameter weights the smoothness of the vector field contra the correspondence of surface features. This parameter has been found by selecting a value that optimises a global shape model criterion.

Initialisation The vector field is initialised by using a closest point projection. This has proven to be a good starting guess for the optimisation of the correspondence.

Optimisation The correspondence vector field is optimised using either Iterative Conditional Modes, which is a deterministic approach or Simulated Annealing, which is stochastic. The choice of optimisation scheme is based on the complexity of the energy functions governing the vector field.

In conclusion, a framework that both solves the present problem with the correspondence vector field and can be used a stand-alone surface registration algorithm has been developed.

5.1.3 A Hybrid ICP/ASM Approach

In an attempt to avoid the expert landmarking of the training data, a fully automated method was tried. The work was carried out by Peter Graversen for his master thesis and details can be found in [115]. It is based on a combination of the ICP and the ASM algorithm and is inspired by the method of Hutton [145]. The fitting of the shape is similar to the method described in Appendix D.

The steps in the algorithm are:

1. Given a set of unregistered examples and a model shape.
2. Align the model shape with two of the unregistered examples using ICP and insert these two aligned shapes into the training set.
3. Build a shape model from the training set using Procrustes and PCA.
4. Use the average shape from the shape model as the new model shape.
5. Select a new unregistered shape, T.
6. Align the model shape with T using ICP.
7. Deform the model shape using the modes of variation from the ASM to fit T.
8. Repeat from step 6 until convergence
9. Project the points from the aligned and deformed model shape to T thus creating a new instance, S, of a shape with point correspondence.
10. Insert S into the training set.
11. Repeat from step 3 until all shapes in the training set are included in the model.

Since the ICP fitting is often falling into local minima, a pre-registration of all shapes is done using a moment-based method.

It proved possible to build a shape model of the ear canal automatically. A visual comparison of the results from the automatic method with the results from the semi-automatic method presented in Appendix A, shows that the resulting modes of variation from the automatic method are less pleasing. The two models where also compared using the optimality criteria defined in Section 4.3. The compactness as measured by the total variance of the models was 11% less for the automatic method than for the semi-automatic method, which is a marked improvement. This could be caused by the fact that in the semi-automatic method some landmarks force the model to stretch and cover the whole area between the first and the second bend of the ear canal, while it is suspected that the automatic method ignores the area around the second bend. It was also demonstrated that the model built with automatic method has a better generalisation ability than the model built with the semi-automatic method.

The method suffers from some regularisation problems and the pre-alignment is very application specific. Furthermore, the choice of model shape is critical concerning the quality of the final model. The regularisation issue could probably be alleviated by combining the method with the MRF framework presented in Appendices B and C. Secondly, the model shape could be constructed iteratively using the results of the intermediate models as for example done by Brett and Taylor in [40, 41].

In conclusion, it has been shown that it is possible to automatically build shape models of the ear canal and that the resulting model possesses qualities that are comparable or better than the model from the semi-automatic framework. This method will probably be the basis of further statistical analysis of the ear canal shape.

5.2 Groupwise Methods

Prior work on pure groupwise methods is sparse. Probably because the complexity increases drastically when compared to the pairwise methods. Thus, groupwise methods inherently need much more computational power.

Duta et al. present a fully automated method for 2D shape outlines in [85]. It is based on a combined Procrustes and clustering algorithm and has been demonstrated on a set of brain structures. However, it appears that it would be difficult to extend the method to 3D data.

A groupwise method is presented by Hill et al. [128, 129]. Outlines of 2D objects are polygonised and an optimisation scheme is used to optimise correspondence using a measure of *representation error*. Furthermore, it is hinted that the method may be extended to 3D using a combination of the iterative closest point algorithm [25, 262] and a decimation algorithm [220]. It seems that the work later evolved into the MDL method described in the next section.

5.2.1 The MDL Approach

The Minimum Description Length (MDL) solution to the correspondence problem was proposed by Davies et al. in 2001 [74, 75]. Originally, the method was demonstrated on 2D shape outlines, but has later been extended to 3D surfaces [73, 76, 77]. Furthermore, a modification of the MDL framework, where the curvature of 2D silhouettes is used in the optimisation can be found in [244].

Since the MDL method has received so much attention and very good results have been published it was natural to try to apply the method on the ear canal data set. This work was carried out by Allan Reinhold for his Master Thesis [160].

The MDL method consists of three nearly independent parts [73]:

- A method of manipulating correspondence. For the 3D case, this consists of mapping the object to a sphere and then using a re-parameterisation with Cauchy kernels to move the landmarks around.
- An objective function based on the MDL measure.
- A method of optimisation that minimises the objective function by manipulating the correspondence.

In summary, the first step in the implementation of the MDL framework is to find a good way to map a shape to a sphere or another suitable primitive. In previous published work, the 3D objects had spherical topology, which obviously had a great influence on the choice of mapping.

The mapping has to be area preserving to keep a correspondence between the movement of a landmark on the sphere and on the original shape. Davies et al. [73] uses a mapping method proposed by Brechbühler et al. [39]. In this method, the object is initially transformed into a voxel representation and then mapped to a sphere by solving a Laplace equation with Dirichlet boundary conditions. This initial mapping is then optimised to make it approximately area preserving. Moreover, Quicken describes a more efficient, hierarchical optimisation of the method in [209]. The method requires that a *north-pole* and a *south-pole* vertex are selected. However, as explained later, the quality of the mapping is very dependent on the selection of these vertices.

We found this method unsuitable for the ear canal data for two reasons. The data is *born* as 2D surfaces embedded in a 3D space. A voxel representation of the data would cause a significant loss of precision due to the quantification of the polygonal data. Secondly, the ear canals do not have a spherical topology since they are open in two ends. The placement of the openings is arbitrary and therefore they cannot just be closed to form a sphere. Put it in another way, we do not want to model the position of the opening of the ear canals. Therefore, we needed to find an alternative mapping method. This turned out to be more difficult than we had hoped.

Mapping is an active research field with different approaches. Examples are the already mentioned approach by Brechbühler [39], a Laplace-Beltrami operator based method [10, 120], and a circle packing method [142]. Most methods produce a conformal mapping, meaning that angles between oriented curves are preserved [82], but area is not preserved. Some current research on area preserving mapping is presented in [9], where the focus is on mapping of spherical geometry. One suggested solution in [9] is an initial Laplace-Beltrami mapping followed by an optimisation step. Mapping of non-spherical geometries are also the focus of current research. A method for conformal mapping of the colon exists [119, 193]. This method is equivalent to the Laplace-Beltrami method and therefore generates a conformal map of the colon to a plane.

In the chosen approach, a conformal map to the sphere is initially built using the Laplace-Beltrami based method described in [10]. Formulated in physical terms this corresponds to solving the steady state heat equation over the surface, with a heat source placed at the defined north-pole and a heat sink placed at the south-pole. Since this is essentially the same as the method Brechbühler uses [39], we believe that their initial mapping is also conformal. The surface heat equation is approximated by using a finite element method [140] giving a linear system of equations that can be solved by standard sparse matrix operations.

The second step is an optimisation step, where the vertices on the unit sphere is moved to minimise the area distortion of the mapping. A local PCA based method is used to move a vertex so the local area distortion is minimised. This local optimisation is used in a global deterministic relaxation scheme, called Iterated Conditional Modes (ICM), proposed by Besag as part of his Bayesian image restoration framework [23]. Further details can be found in [160]. Opposed to the method by Brechbühler [39] the connectivity of the surface mesh is not changed during optimisation.

With this method, it proved possible to generate an approximate area-preserving mapping of objects with spherical geometry and a modest number of triangles. An example can be seen in Figure 5.1, where the optimisation has been used to map the surface of a human brain to a sphere. However, the quality of the result is dependent of the choice of the north-pole vertex and the quality of the initial conformal map.

The ear canal data comes from a laser scanner and each scanned ear canal contains a large number of triangles. The polygonisation is furthermore very uneven, with large variations in the triangle side length and connection number as seen in Figure 5.2. It proved very difficult to generate a stable mapping of

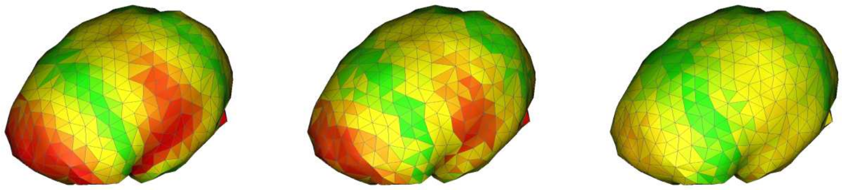

(a) Initial (b) 1 iteration (c) 5 iterations

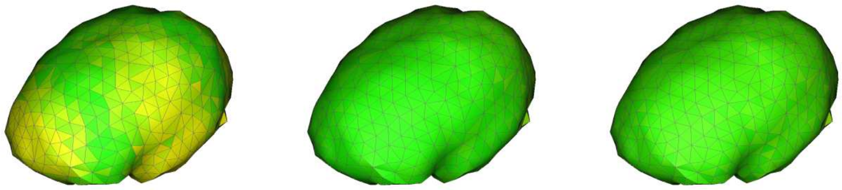

(d) 10 iterations (e) 50 iterations (f) 100 iterations

Figure 5.1: Area distortion minimisation per iteration. Red triangles display a high degree of area distortion as opposed to green triangles. Illustration from [160].

the ear canals, partly because of numerical problems.

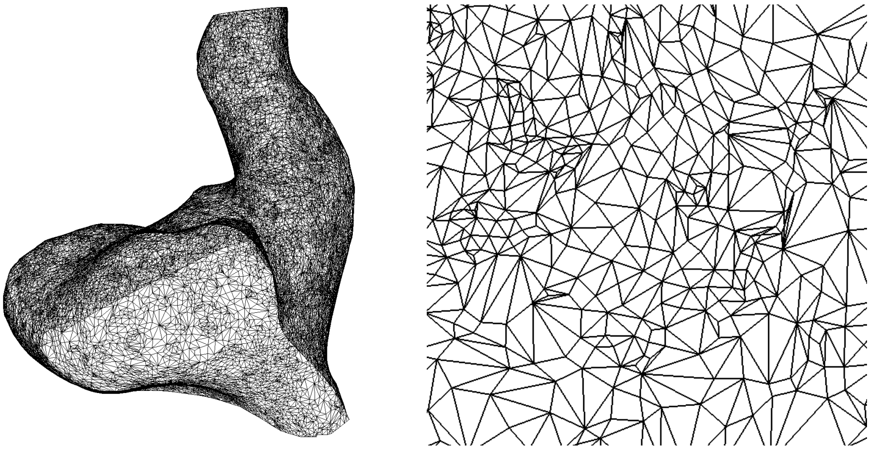

Figure 5.2: Wireframe representation of the surface of an ear canal. It is seen that the triangulation is non-uniform, with triangles of varying sizes and aspect ratios.

In the MDL framework the objective function is obviously the minimum description length or rather an approximation of it. As pointed out by Thodberg [243] the MDL objective function in the later versions of the framework resembles the much simpler objective function used by Kotcheff and Taylor [169], namely the determinant of the covariance matrix. This criterion has successfully been used to evaluate the results of the pairwise MRF framework as seen in Appendix C.

In the initial MDL method, the optimisation was done using genetic algorithms because of the many local minima. Recently it has proved possible to use gradient-based optimisation with the MDL objective function [92, 93].

The choice of MDL as an objective measure is based on the assumption that it indirectly optimises the three optimality criteria described in Section 4.3. This leads to the question of why not construct an objective function, which is based on these measures directly? The answer is probably that it would require horrible computation power and that an alternative method to validate the optimised model would be required. It would also be difficult to weight the three or four optimality criteria in the final objective function.

In conclusion, the use of the MDL framework on the ear canal data requires a good and stable method of area preserving mapping of non-spherical objects and this was not possible to implement. Finally, it was deemed that this task was outside the scope of this thesis.

5.3 Discussion

The task of generating shape correspondence is difficult. First, it is not certain that a diffeomorphic shape correspondence exists.

It is obvious, that the correspondence problem can be formulated as an optimisation task. However, it is also obvious that the objective function and the way of optimising the correspondence must be chosen based on the application and the data.

The idea of optimising the groupwise correspondence seems to be the future. However, the current state-of-the-art approach, the full MDL framework proved very difficult to adapt to our data.

An important aspect is that the objective function and the optimisation scheme are independent. Hence, the MDL measure can be used with alternative point-correspondence generating functions.

Part II

Automated Design of CIC Hearing Aids

CHAPTER 6

Collision Detection, Path Planning, and Offset Surfaces

This chapter introduces a set of algorithms that are used in Chapter 7. The methods come from computational geometry, computer graphics, and dynamic programming.

6.1 Union of Balls and the Medial Axis Transform

Used initially for surface reconstruction, the Power Crust [3, 4] later proved to be even more valuable, since it provided us with a medial sheet of the ear canals.

The definition of the medial axis of an object is commonly given as the locus of centres of maximal balls inscribed into the object. An inscribed ball is maximal if it is not strictly contained in another inscribed ball. Formally, the medial axis transform (MAT) is a representation of an object as the infinite union of its maximal balls. In this thesis, the MAT of a three-dimensional object is approximated with a finite union of balls. The MAT is also called the *medial sheet*.

The exact calculation of the MAT for complicated shapes is currently not possible, but several techniques for calculating an approximation exist. The Voronoi diagram and its complement, the Delaunay triangulation is typically used in these algorithms. In [224] the MAT is approximated using the Voronoi diagram. However, Amenta et al. claim that this approach is not correct and that a weighted Voronoi diagram called a *power diagram* should be used instead [3, 4]. The Power Crust approximates the object with a set of spheres, called *polar balls*. Both the inside volume and the outside volume of the object are approximated. As will be shown later this is very handy. The inner polar balls and the medial sheet calculated for an ear canal can be seen in Figure 6.1. The outer polar balls can be seen in Figure 6.2.

6.2 Collision Detection

Collision detection is a field of much research, but also with a huge number of practical applications. Typical examples of applications are flight simulators, surgery simulation, virtual reality and probably the most significant, computer games. In these applications, real-time performance of the collision detection algorithms is needed. Space partition methods are often used to achieve this kind of performance. Hence, a large number of different ways to present 3D data in performance enhancing hierarchies exist. Examples are octrees [188], kD-trees [20], and binary space partitioning trees (BSP-trees) [102]. These spatial partitioning algorithms are often used to represent fixed environments, in which other objects navigate. In our case, parts of a hearing aid move inside an ear canal. It would therefore be obvious to use some kind of space partitioning of the ear canal.

When the collision occurs between two or more objects a number of ways to represent the object exists. One way is to represent an object using a hierarchy of axis-aligned bounding boxes (AABB-trees) [21] or the slightly more advanced oriented bounding boxes (OBB-Trees) [112]. However, biological objects are sometimes not well approximated by rectangular boxes. Hubbard proposes an alternative method that represents an object as a hierarchy of spheres [137, 138]. The set of spheres approximating an object is calculated using a stable Voronoi diagram method [139]. Another alternative is the discrete orientation polytopes (DOPs) approach [124, 165, 166, 167]. A k-DOP approximates the convex hull of an object, where k indicates the number of planes that are used. Hence, a 6-DOP is equal to rectangular box, while higher order k-DOPs provide a tighter approximation of the convex hull.

Collision detection algorithms are often specially crafted to each application

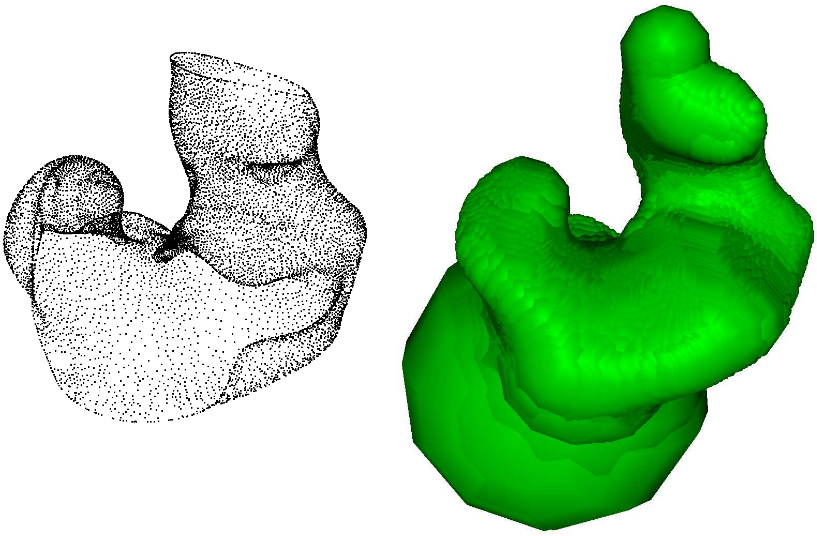

(a) Point Cloud (b) Polar Balls

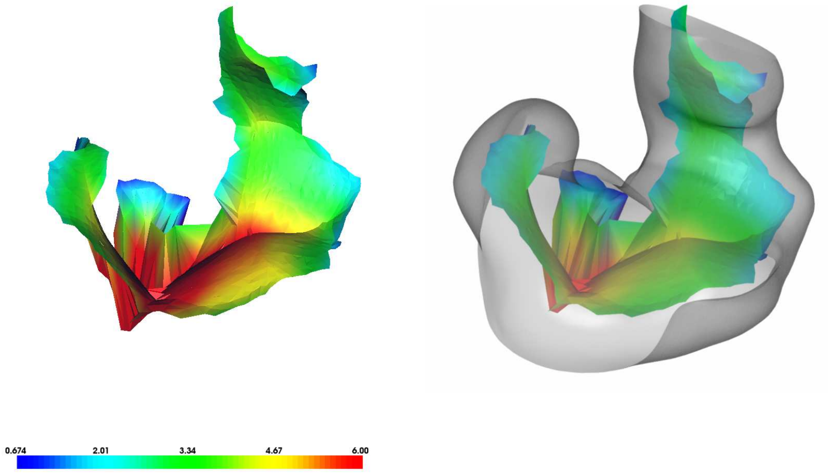

(c) Medial Sheet (d) Medial Sheet and Surface

Figure 6.1: The approximation of the medial axis transformation of an ear canal. It is seen that the collection of polar balls approximates the volume spanned by the point cloud. The medial sheet is colour coded according to the radii of the medial balls. The large ball is placed at the opening of the ear canal. Scale is in millimetres.

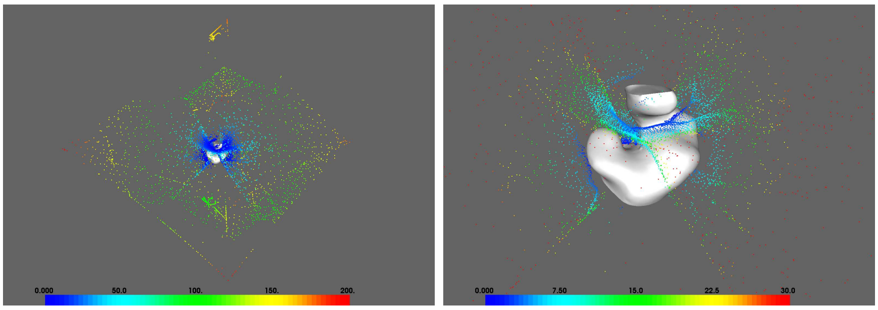

Figure 6.2: The centres of the outer balls colour coded according to their radii. It is seen that the balls are enclosed in a bounding volume much larger than the actual ear canal.

since the nature of the scene determines the optimal approach. Our case is somewhat special since we need to check if a component is completely inside the ear canal. In addition, it is necessary to calculate the amount of penetration so a measure of severity of the collision can be given.

To determine the volume of the intersection a technique known as *constructive solid geometry* (CSG) can be used [91, 136, 171]. One problem using CSG is that it is required that the objects are closed and that is not the case with the ear canal. Tricks can be made to make it a closed object, but that is not optimal. Finally, a combination of methods, were chosen. These are described in the next section.

6.2.1 Collision Detection in the Ear Canal

The chosen approach is customised to the problem at hand. It is based on the spherical decomposition technique [137, 138] and OBB-trees [112].

A component is represented as an OBB-tree as seen in Figure 6.3. To build the OBB, a recursive, top-down process is used. Initially, the root bounding-box is found by calculating the eigenvectors of the covariance matrix of the points from the object. These three orthogonal vectors define the tightest fitting bounding box. The two children of this bounding box are found by a plane that approximately divides the object in half. These two point clouds are then used to compute the two child OBBs. This process continues until the desired tree-depth is reached or no splitting is possible.

As described in Section 6.1, the Power Crust computes a medial sheet consisting

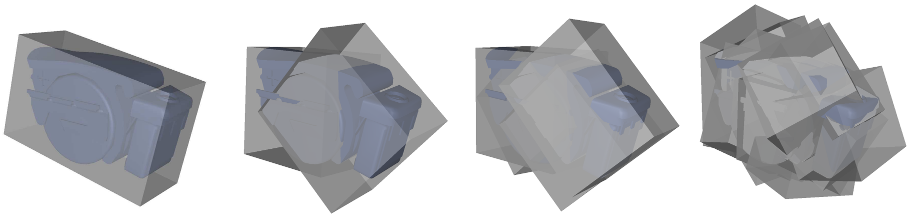

Figure 6.3: OBB-Tree representation of a collection of components. From right to left the OBB-tree level 0, 1, 2, and 4.

of a collection of connected vertices. Each vertex in this sheet also represents a medial ball (also called a polar ball) that touches the sides of the reconstructed surface. The collection of medial balls is thus a very good approximation to the object enclosed by the surface as seen in Figure 6.1. In addition, a medial sheet representing the space *outside* the object is produced. This sheet is bounded by a box much larger than the object as seen in Figure 6.2. Since it is very easy to determine if a point lies inside or outside a sphere, the collection of medial balls can be used to determine if given points lie inside or outside the object approximated by the balls. This method resembles the method by Hubbard [137, 138]. To check if a point from the component is placed inside or outside the shell, there are two possibilities. The first is to examine if the point is contained in any inner medial ball, if not it must be outside. The second is to examine if an outer medial ball contains the point, which would also mean that it is outside. As motivated later, we use the outer medial balls to determine if there is a collision. Moreover, a temporal caching technique is used to speed up collision detection involving objects that only moves a little from frame to frame. A list of medial balls containing colliding points is kept and used to check if the point is still colliding with these balls in the next frame. Furthermore, collisions between balls and points are checked in the order of the size of the balls, with the largest balls being checked first. The level of OBB-tree used to represent the components is chosen dynamically. In the final iterations all the points from the polygonal representation of the component is used. A collision between a CIC and an ear canal detected by this method is seen in Figure 6.4.

The penetration depth is formally defined as the minimum translation distance needed to separate two objects. However, the calculation of the true penetration depth is very difficult [162] and outside the scope of this thesis. Instead, an ad hoc method for the estimation of the penetration depth is adopted. The penetration depth is defined for a point as being the distance to the nearest point on the surface. This distance can be calculated using the technique described in Section 6.4, but this method is very slow. Hence, an alternative method that provides a quick approximation to the distance is used. The penetration depth

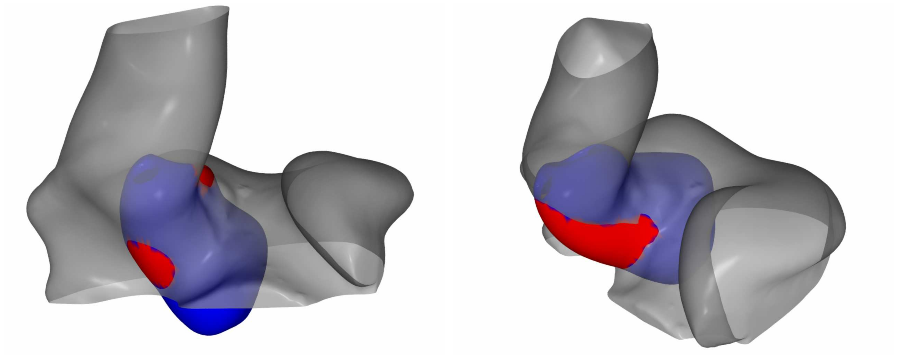

Figure 6.4: Collision between a CIC and an ear canal detected using the medial balls. The red areas of the CIC are where the CIC is colliding with the ear canal.

of a given point is computed using the outer, medial balls. When an outer medial ball contains a point, P, a *collision vector* can be calculated as

$$\mathbf{v}_{\mathrm{col}} = r\frac{(P-C)}{\|P-C\|}, \tag{6.1}$$

where r is the radius and C is the centre of the ball. This is illustrated in Figure 6.5. All collision vectors can be calculated by finding all the balls that contain the point. Averaging these vectors yields an estimate of the direction of the true penetration vector. The penetration depth is calculated as $d = \max\|\mathbf{v}_{\mathrm{col},i} \cdot \overline{\mathbf{v}}_{\mathrm{col}}\|$ and an approximated penetration vector as $\mathbf{v} = d\overline{\mathbf{v}}_{\mathrm{col}}$, where $\overline{\mathbf{v}}_{\mathrm{col}}$ is the normalised, average collision vector. The collision and penetration vectors from a set of vertices can be seen in Figure 6.6. Finally, the severity of a collision between a component and the ear canal is calculated as the sum of penetration depths of all vertices in the component, $\mathcal{F}_{\mathrm{collision}} = \sum_i d_i$.

The method contains several weaknesses. First, it ignores the origin of the points. When a point is part of a larger object, the positions of the remaining parts of the object should be taken into account. Secondly, there is no proof that the method actually estimates the minimum distance to the surface. Nevertheless, the method has proven to work well with our data.

6.3 Path Planning

As will be demonstrated in Chapter 7, it is highly beneficial if a path through the ear canal can be computed. It is intuitive that the path is close to the medial

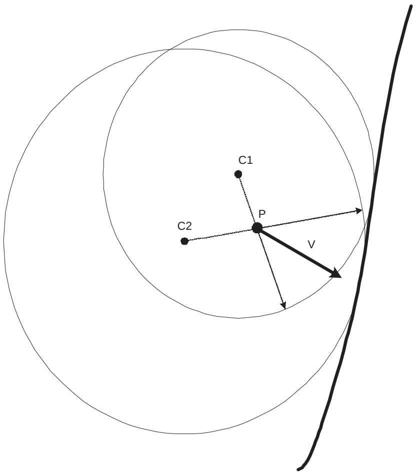

Figure 6.5: Point P is found in two outer medial balls with centres C_1 and C_2. The true penetration vector **v** is estimated based on the two shown collision vectors.

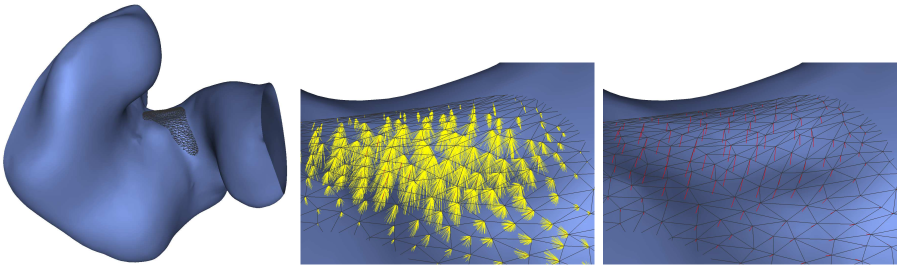

Figure 6.6: Collision between a component and the ear canal. All the collision vectors are shown in the middle and the approximated penetration vectors are shown to the right.

sheet of the ear canal. Furthermore, it is believed that the path should be based on the diameter of the ear canal. Based on this assumption the path through the ear canal is computed as a weighted shortest path on the medial sheet. This approach resembles the technique used to calculate fly-through paths in virtual endoscopy [192, 193].

The medial sheet described in Section 6.1 is represented as a mesh, consisting of connected vertices. A mesh can be seen as either a directed graph or an undirected graph. For use in the shortest path algorithm, the mesh is treated as a directed graph, where all vertices connected in the mesh are connected by two directed edges in the graph. In addition, a weight is assigned each edge in the graph. If the lengths of the edges are used as weights, the result is a geodesic shortest path.

Several techniques to compute shortest paths on graphs exist. A well-known single-source shortest path method is Dijkstra's algorithm [80]. According to Kimmel and Sethian, Dijkstra's algorithm can be inconsistent. If Dijkstra's algorithm is used on a square grid, several shortest-paths exist, since the algorithm uses the Manhattan distance [163]. In contrast, the *Fast Marching Method* is a consistent approximation to the continuous partial differential gradient operator. Since it can use sub-grid resolution, it finds a better approximation of the true shortest path [163, 222, 223]. Moreover, Antiga has demonstrated the use of the Fast Marching Method on medial sheets to calculate centrelines in vascular structures [11, 12]. Nevertheless, we believe that Dijkstra's algorithm provides sufficiently precise results in our case, since the meshes of the medial sheets are densely triangulated. The implemented Dijkstra's algorithm has been made public available and is described in detail in Appendix E.7.

The algorithm finds the shortest path between a start vertex and an end vertex that must be identified beforehand. In this project, the start and end vertices are found by atlas mapping. The shape model is fitted to the new ear canal as described in Section 4.2.4. After the fitting, two landmarks are propagated from the fitted model shape to the new ear. These two landmarks are placed at the entrance to the ear canal and at the tympanic membrane. Finally, the start and end vertices are chosen as the two vertices closest to these two landmarks.

The geodesic shortest path tends to cut corners by design. Hence, it would be convenient if the sizes of the medial balls could be used to guide the path. In summary, we are searching for a path that favours the middle part of the ear, but is still in some sense optimal. The solution was found by treating the graph as a connection of electrical wires. Hence, the path is calculated as the single line of wires connecting the start and the end vertex with the least resistance. We call it the *path of least resistance*. The wire from vertex v_i to vertex v_j has the resistance:

$$R_{ij} = \frac{\rho L}{A}, \tag{6.2}$$

where ρ is the resistivity of the material, L is the length and A is the cross sectional area of the wire. This can be simplified so that the edge from vertex v_i to v_j has the edge cost:

$$w_{ij} = \frac{L}{r_j^2}, \tag{6.3}$$

where L is the length from v_i to v_j and r_j is the radius of the medial ball placed at v_j. A path through the ear canal found with this method can be seen together with a geodesic shortest path in Figure 6.7. It is seen that the path of least resistance has the desired properties, since it follows a path going through the widest areas of the ear canal while still finding a direct path.

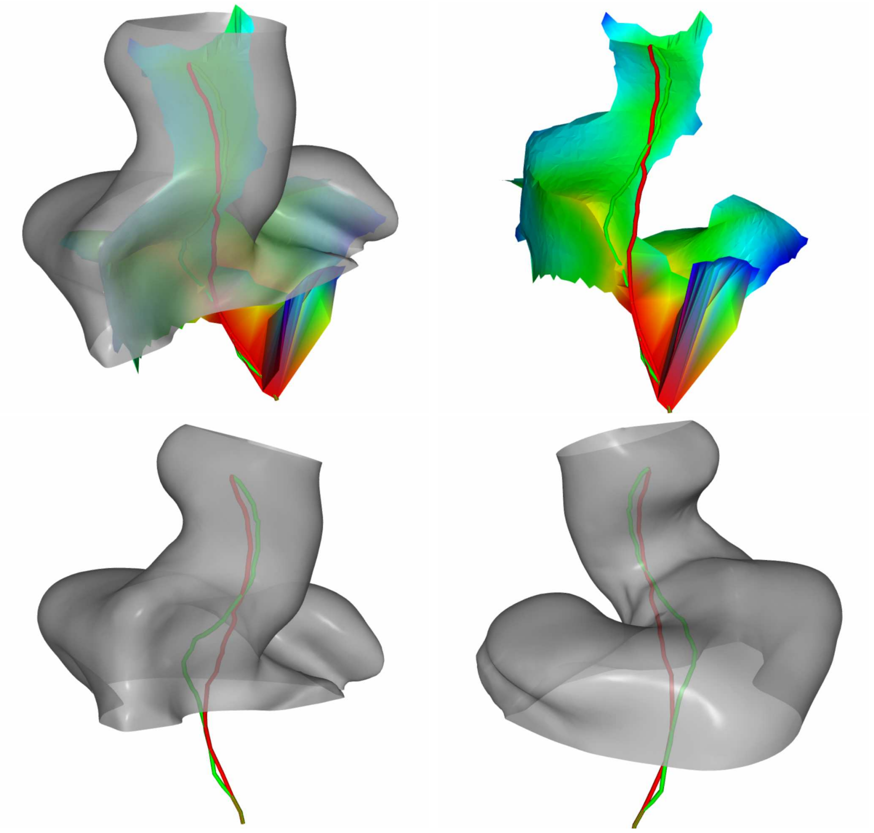

Figure 6.7: The path of least resistance (green) compared to the geodesic shortest path (red).

6.3.1 Medial Distances

Often the question “How deep or how long is the ear canal?” is posed. Since the ear canal is a bending tube, this question is not simple to answer in a consistent manner.

We propose a new distance measure, *the medial distance*, to measure distances in the ear canal. This distance is measured by following the path of least resistance. Initially, the closest point on the path of least resistance is found for both points. Secondly, the medial distance is calculated as the path length between these two points.

6.4 Offset Surfaces and Shelling

An offset surface is a surface that is similar to the initial surface but offset with a positive or negative value [100, 216]. A more formal definition is that an ε-offset surface from F is a surface F', formed by the points x such that the distance from x to the nearest point on F is exactly ε [3]. A simple way of producing an offset surface is to move the vertices of the original surface in the direction of the normals. This works for convex surface with positive offsets, but folds will be generated if the surface is more complex.

According to Amenta, an offset surface can be computed by using the results from the Power Crust algorithm [3, 4]. Manipulating the radii of the inner and outer polar balls and extracting the resulting intersection surface, should give an approximate offset surface. However, we have chosen an approach based on a 3D distance transformation. It is explained in the following.

A distance transformation is a grid where each element contains the shortest distance to the surface [35]. A distance field is signed if the sign of the distance is dependent on the element being placed inside or outside the surface. In the following a 3D distance transformation is used, meaning that an element is a voxel in a voxel-volume. Several algorithms for computing distance fields exist. A method that uses a tree of bounding boxes to store the triangles of the mesh and use this to speed up distance calculations is proposed by Payne and Toga [203]. A case analysis is performed when the distance from a point to a triangle is computed, since it is necessary to know if the closest point on the triangle is a vertex, lies on an edge, or lies on the face itself. A similar approach is presented in [118], where the mesh is represented in hierarchy of simplifications. The distance field is initially computed on a coarse level and then gradually refined. In a recent method for calculating signed distance fields, Bærentzen and Aanæs [16] propose to use an *angle weighted normal* in addition to the case analysis to correctly calculate the sign of the distance.

Since the ear canal is not closed, it is problematic to define what is inside and what is outside. Evidently, there is an inside of the cylinder, but the ambiguity appears near the openings of the canal. In practice, the unsigned distance transform proved to be sufficient for our needs.

The implemented method is similar to the approach presented in [203] and the method used by Hoppe in his work on surface reconstruction [131]. Initially a voxel volume surrounding the surface is created. For each voxel, the distance to the closest point on the surface is calculated using a spatial search tree. The triangles of the mesh are stored in a uniform-level octree [188], where each octant carries an indication of whether it is empty or not, and each leaf octant carries a list of the triangles inside it [219]. However, the method can be optimised significantly by using the bounding box approach proposed in [203] and [16]. In addition, the method can be extended to a signed distance by using the approach suggested in [16].

When a distance transform has been computed, offset surfaces can be extracted as iso-surfaces. The standard method for iso-surface extraction is the marching cubes algorithm [183]. An extracted iso-surface can be seen in Figure 6.8. The unsigned distance transform is used meaning that the iso-surface is wrapped all around the original surface. If the signed distance transform is used a choice must be made for handling the volume surrounding the openings of the ear canal. However, this was not necessary for our purpose.

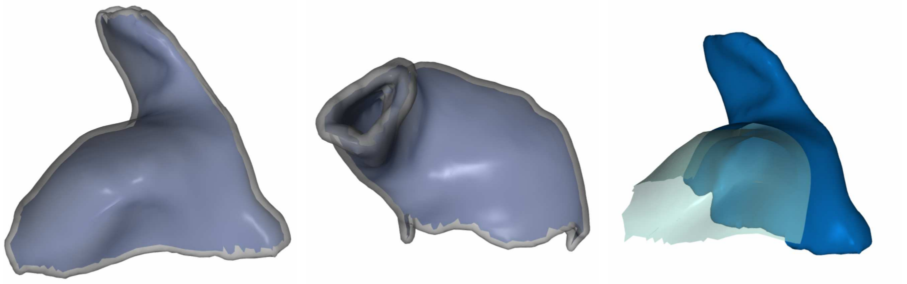

Figure 6.8: Original surface and the 0.6 mm iso-surface. The unsigned distance transform is used.

Shelling is the process of adding a thickness to a surface. Extraction of an iso-surface from an unsigned distance field essentially solves this as seen in Figure 6.8.

Precision is lost when converting a surface to a voxel grid since the precision is dependent on the voxel size. The number of voxels in the volume is cubically dependent on the voxel size, so there is a trade-off between memory usage and precision. However, when using the distance transform some of the lost precision is regained due to the extra information contained in the distance measure. The iso-surface extraction has sub-voxel precision and is able to use the information stored in the distance transform. Still care has to be taken to select the optimal voxel size.

6.5 Discussion

This chapter presented various techniques that are used in the component placement framework. While the methods are well known from computer graphics, some innovation was still needed to adapt them to the problem at hand.

Chapter 7

Component Placement

This chapter presents a framework for automatically placing 3D components in a container. The framework is applied to the problem of placing a faceplate and the associated components in an ear canal.

The problem of component placement is found in many disciplines, and with many names including 3D bin packing, container loading, pallet loading, 3D palletisation[1], and printed circuit board layout [15, 45, 46, 47, 132, 147, 189, 197, 215, 225, 237, 239]. Generally, the problem can be formulated like this [46]:

> Given a set of three-dimensional objects of arbitrary geometry and an available space, find a placement for the objects within the space that achieves the design objectives, such that none of the objects interferes, while satisfying optional spatial and performance constraints on the objects.

Previous approaches are usually tailored to a specific application, thus limiting the problems that can be solved. Printed circuit board layout is an example of a specialised problem, where the components are limited to rectangles aligned

---

[1] The packing of goods on to small wooden platforms, or pallets, for ease of handling in shipment.

in 2D along orthogonal axes [45, 46]. Similar constraints exist for other applications. As a curiosity, it is claimed that the physical placement of neural components in the brain appears consistent with a single, simple goal: minimise the cost of connections among the components [56].

Our problem can be formulated like this

> Given an ear canal and a set of components, place the components
> in the ear canal, as would an expert operator.

Fulfilling this requires both insight in the routines, behaviour, and thoughts of the operator and a flexible framework for component placement. We therefore start by introducing a generic framework and later apply it to the problem stated above.

7.1 A Component Placement Framework

Instead of limiting the framework to a specific application, we formulate it as a set of steps, where each step can be tailored to the problem at hand.

Problem Analysis

The task is often to reproduce or improve results previously made by human operators. This could be the placement of engine parts in a car motor or the packing of a truck. Therefore, it is very beneficial to learn which methods the trained operators are using to solve the task.

Formulation of an Objective Function

Based on the expert operators' experience and practical considerations an objective function can be formulated. Evidently, the objective function should be computable and since it will be evaluated often in the optimisation phase, it is preferable that it is not very complex to compute. An objective function can for example be a combination of *maximisation of packing density*, *minimisation of routing costs*[2], *minimisation of component heating* [48], and *minimisation*

---

[2] Routing means to connect components using for example wires or tubes.

of electromagnetic field interference [46, 147, 215]. Furthermore, an objective function often involves distances and the amount of collision between the components.

A complication is to determine the weights used in the final objective function. That is to select how much each term should influence the final solution. In addition, it can be beneficial to change the weights during the optimisation. For example allowing collisions in the start and penalising them heavily in the end. In certain circumstances, it is possible to determine the weights using a leave-one-out study.

Determination of Hard Constraints

Some states are not acceptable and therefore hard constraints can be specified. One hard constraint is for example that components must not overlap and must not be outside the container. Another example is that a container for liquid should have the opening upwards. It can be useful to formulate the hard constraints so they are solely enforced in the end of the optimisation phase, since finding the global optimum often requires crossing illegal states.

Definition of the State Space and a Move Set

To be able to optimise the placement, it is necessary to define a set of movements for the components and thereby defining the state space that the optimisation algorithm navigates. In previous work, nearly all problems are constrained to finite state spaces meaning that each component is only allowed a finite set of movements [15, 46, 147, 215, 239]. These can for example be a translation of a given length or a fixed angular rotation around one of the coordinate axis, giving the component a limited number of degrees of freedom. Another possibility is to allow the components to move freely. Hence, the position of a component is controlled by six continuous parameters. In summary, there is a drastic increase in the dimension of the state space for each free component.

Initialisation

Normally there is the need for an initialisation step where the components are placed in a start state. This start-state should provide the optimisation algorithm with a starting guess, but does not need to fulfil any constraints.

Optimisation Strategy

Cagan et al. claim that the solution space of 3D layout problems is of fractal nature [47]. Deterministic algorithms are therefore not suitable for locating the global minimum, and stochastic algorithms are usually required for good quality solutions.

In the literature, several different optimisation strategies have been used to solve the problem. If the state space is limited and can be considered as a finite string of states a genetic algorithm approach can be chosen [132, 147]. Another option is the similar A-teams algorithm [215]. A popular optimisation strategy is simulated annealing [46, 57, 164, 172, 248]. A similar problem with a finite state space, where simulated annealing has been used to find approximate solutions is the travelling salesman problem [208].

When the state space is not finite, genetic algorithms and other algorithms that require that the state space can be formulated as a string cannot be used. Instead, simulated annealing seems to be the best solution.

Validation

When the placement of the components has been optimised, there is a need for a validation of the result. In some cases, the final value of the objective function is enough. In other cases, a total sanity check of the final state is needed.

7.2 Hearing Aid Component Placement

In this section, the framework presented in the previous section is applied to the task of placing components in a CIC hearing aid.

It is well known that the single most important factor in the shape of a CIC is the position of the faceplate. This is clearly seen in Figure D.2 on page 149. The faceplate consists of a disk with an attached component package, including a battery. An actual faceplate and the corresponding CAD model can be seen in Figure 7.1.

The placement of the remaining components of the hearing aid is therefore guided by the placement of the faceplate. Naturally, there are situations where the faceplate cannot be placed optimally because there is insufficient space for

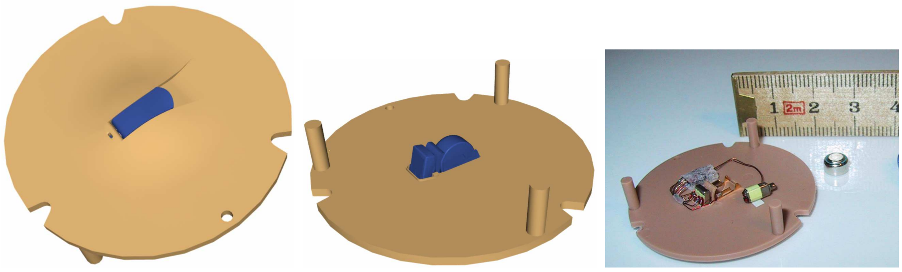

Figure 7.1: The faceplate used in a recent Oticon hearing aid.

the other components in the shell. In addition, the placement of the vent is important. A brief introduction to CIC production can be found in Section 2.3.

Currently, we limit the task to locate the optimal position of the faceplate and the attached components in the ear canal. However, the framework can be extended to include the remaining components. In addition, the vent can be simulated by adding a tube approximated by a thin plate spline to the shell.

The following sections explain each step of the adapted framework in detail.

7.2.1 Problem Analysis

Given a scanned ear canal, the aim is to place the faceplate where it would sit on a CIC hearing aid made for that ear canal. The difference between the ear canal and the CIC shell is that the shell has a thickness. This can be simulated by calculating an inward offset surface of the ear canal and using this when the faceplate is placed. Offset surfaces are treated in depth in Section 6.4.

Since hearing aids are currently made by human operators, the starting point is to gain as much knowledge from them as possible. According to expert 1, a well-made CIC is characterised by

- The components fit in the shell.
- The battery-compartment door points downwards.
- The faceplate is placed approximately where the part of the first bend that is on the concha side has its highest curvature. The bends of the ear canal can be seen in Figure 7.2.
- The faceplate is approximately parallel to the flat part of the concha.

- The faceplate area is as small as possible.

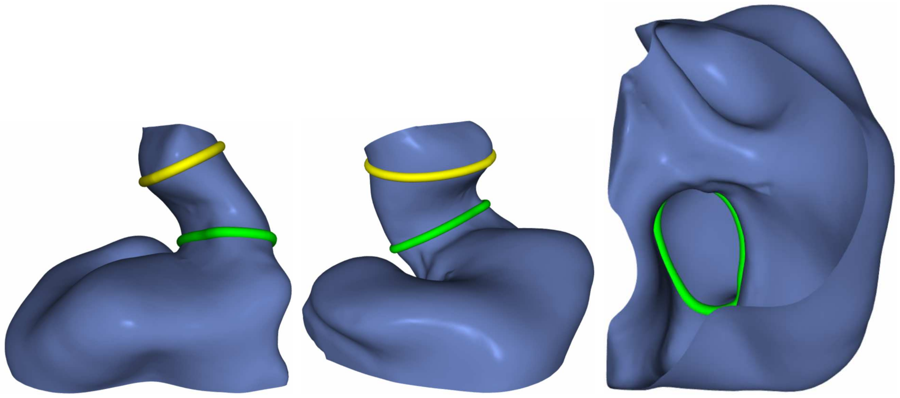

Figure 7.2: The first (green) and the second (yellow) bend on an ear canal. Further description of the ear canal anatomy can be found in Section 2.1.

7.2.2 Objective Function

Inspired by the expert opinion, elements of the objective function are constructed. First, it is necessary to separate the elements of the faceplate that must be inside the shell from the rest. This collection of components can be seen in Figure 7.3. The components are treated as one complex part to facilitate the optimisation.

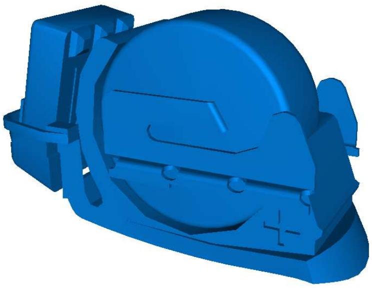

Figure 7.3: The collection of components that must not collide with the shell.

The first term of the objective function, $\mathcal{F}_{\text{col}}$, is the amount of collision between the components and the shell. During the optimisation, the cost of this term is increased, thus it ends as a hard constraint. Collision is not treated as a hard constraint initially, since it has proven necessary to go through illegal states to reach the optimal state. The collision detection algorithm is explained in detail in Section 6.2.

The second term of the objective function, $\mathcal{F}_{\text{area}}$, is the surface area of the part of the faceplate that is inside the shell. It is computed as the area of the closed polygon resulting from intersection the shell with the faceplate plane. A faceplate has a thickness. Hence, the area is calculated based on the visible part of the faceplate. This is seen as the green tube in Figure 7.4.

The third term of the objective function, $\mathcal{F}_{\text{dist}}$, is the distance from the faceplate to the tympanic membrane. Since the data is based on laser-scans of ear impressions, the location of the tympanic membrane is not known, so a qualified guess is used instead. In Section 4.2.4, it is explained how the shape model is used to propagate landmarks from an atlas to a new ear. This way a tympanic membrane landmark is applied from the atlas to the new ear canal. Since the ear canal is bended, the Euclidean distance from the centre of mass of the faceplate to the end of the canal is not optimal. In the optimisation phase, this will result in the faceplate being pulled towards the side of the ear canal. The medial distance introduced in Section 6.3.1 is a better choice of distance measure and is therefore used. The path of least resistance can be seen as the red tube in Figure 7.4. In summary, two points on the path of least resistance are located. The first point is close to the tympanic membrane and the second is close to the centre of mass of the faceplate. Finally, $\mathcal{F}_{\text{dist}}$ is calculated as the path length between the two points.

The fourth term of the objective function, $\mathcal{F}_{\text{align}}$, is the alignment of the faceplate with the path of least resistance. It is computed as the dot product of the normal vector of the faceplate plane and the tangent vector of the closest point on the path of least resistance. Experiments indicate that a better measure of the alignment of the faceplate is the area of the faceplate, even though it is indirect.

Combining these terms gives the total objective function:

$$\begin{aligned}\mathcal{F}_{\text{total}} = \alpha(1-\beta)(1-\gamma)\mathcal{F}_{\text{col}} + (1-\alpha)(1-\beta)(1-\gamma)\mathcal{F}_{\text{dist}} +\\ (1-\alpha)\beta(1-\gamma)\mathcal{F}_{\text{align}} + (1-\alpha)(1-\beta)\gamma\mathcal{F}_{\text{area}},\end{aligned} \tag{7.1}$$

where α, β, and γ weights the individual terms. These weights are currently chosen by trial and error. In addition, they are changed during optimisation. Further details are found in Section 7.2.6.

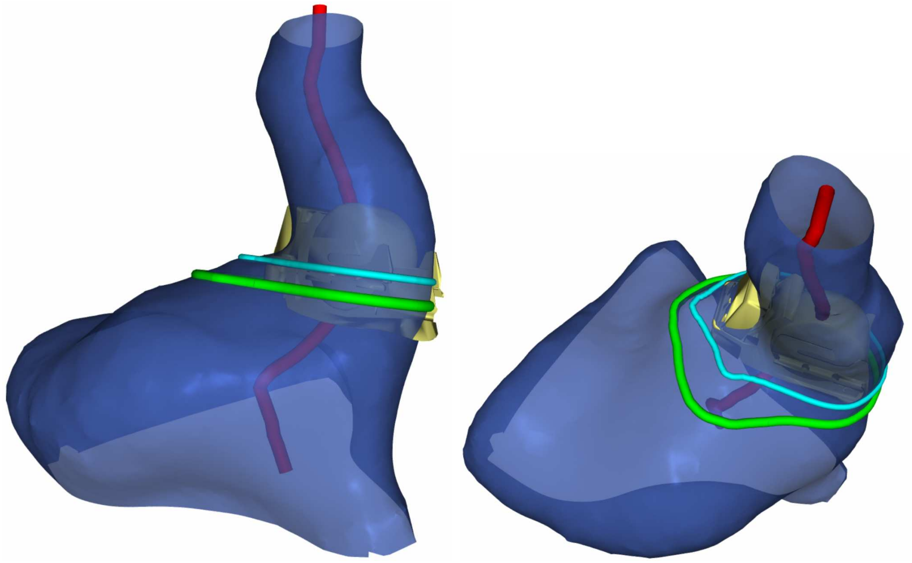

Figure 7.4: Optimisation of placement. The green tube is the intersection between the outer faceplate plane and the shell. The cyan tube is the intersection between the inner faceplate plane and the shell. The red tube is the path of least resistance of the shell.

7.2.3 Hard Constraints

In certain cases, concha is only partly included in the scan, due to the limitation of the used laser scanner. Occasionally, the faceplate is tilted during optimisation, resulting in holes in the intersection between the faceplate plane and the shell. The solution to this problem is to apply a hard constraint. Hence, states that result in holes in the intersection are not accepted during optimisation.

7.2.4 State Space

During the optimisation, the shell is kept in the same position and the collection of components is moved. A movement scheme for the components is therefore needed. Several approaches were considered including limiting the moves to a finite state space, where the components are only allowed to be in certain discrete positions and orientations.

Finally, it was decided that no restrictions should be imposed on the movement of the components. Thus, the state of the component is kept as a six dimensional vector, $\mathbf{s} = (\phi_x, \phi_y, \phi_z, t_x, t_y, t_z)$, where ϕ_x, ϕ_y, ϕ_z are the rotations around the three coordinate axes[3] and (t_x, t_y, t_z) is the translation vector from the origin. A new state is made by adding a vector with random displacements to the current state $\mathbf{s}_{\text{new}} = \mathbf{s} + \Delta\mathbf{s}$, where $\Delta\mathbf{s} = (\Delta\phi_x, \Delta\phi_y, \Delta\phi_z, \Delta t_x, \Delta t_y, \Delta t_z)$.

7.2.5 Initialisation

The initialisation should serve as a good start-state for the following optimisation. We use the method described in Appendix D to give an initial estimate of the placement of the faceplate. This approach places an ideal, component-free faceplate in the ear canal. When the real faceplate is initially placed in the position of an ideal faceplate plane, there is a very high probability that some components of the faceplate will collide with shell. This can be seen in Figure 7.5.

To improve the initial placement some additional steps are taken. The centre of mass of the components is moved to the centre of mass of the intersection between the faceplate and the shell. This intersection can be seen as the green tube in Figure 7.4. Secondly, the components are rotated around the plane normal to locate the rotation that minimises collision. In addition, the

---

[3] Rotations are applied in Y, X, Z order.

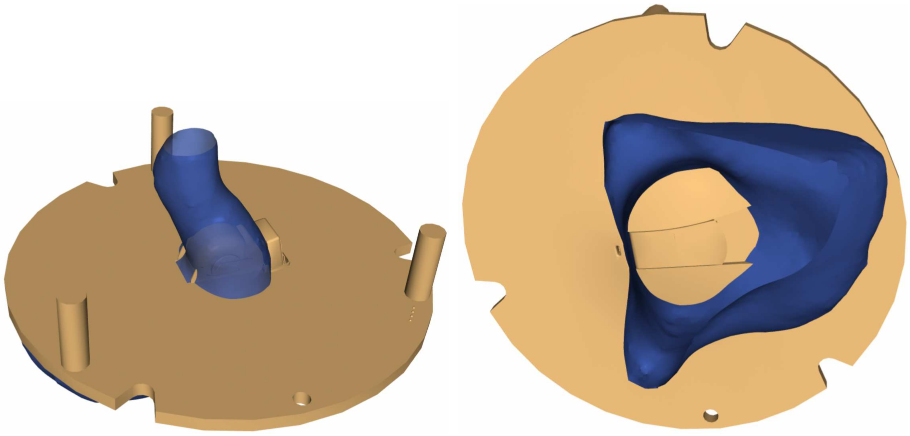

Figure 7.5: The initial placement of a faceplate with components in an ear canal. It is seen that components collide with the shell.

battery-compartment door shall point downwards. To determine if the battery-compartment points downward, the direction of the components are compared to two landmarks. The landmarks are placed at the first bend and indicate the up-down direction of the ear canal. They are located by the shape model using atlas mapping, as explained in Section 4.2.4. The initialisation steps can be seen in Figure 7.6.

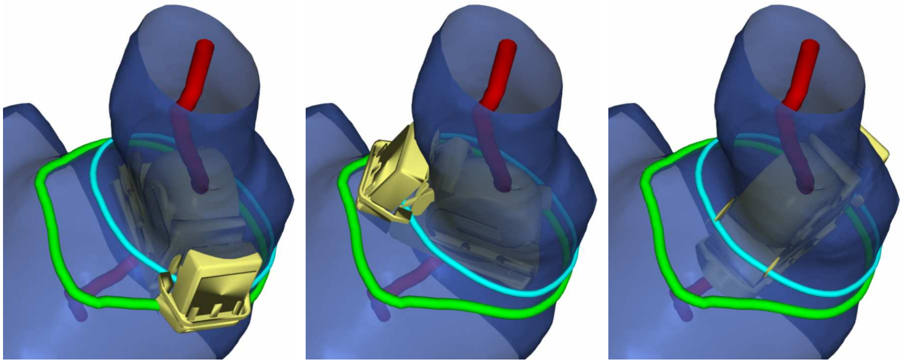

Figure 7.6: The initialisation step. The components are rotated until there is minimum collision and the battery-compartment door points downwards.

7.2.6 Optimisation

The optimisation is performed using simulated annealing [164, 248]. For each iteration, a new component state is generated following the method described in Section 7.2.4 and the objective function is calculated for the new state. The change in the objective function is given by $\Delta\mathcal{F}_{\text{total}} = \mathcal{F}_{\text{total}}(\mathbf{s}) - \mathcal{F}_{\text{total}}(\mathbf{s}_{\text{new}})$. $\Delta\mathcal{F}_{\text{total}}$ is also called the energy of the state. The new state is accepted with a probability given by:

$$P_{\text{accept}} = \min(e^{\frac{-\Delta\mathcal{F}_{\text{total}}}{T}}, 1), \tag{7.2}$$

where T is a parameter referred to as the temperature. The temperature governs the probability of accepting inferior steps. The temperature starts out high and decreases with time following a cooling schedule [57, 172]. Here a simple schedule is chosen where the temperature is dropped by a percentage each N iterations.

In the start where the temperature is high, nearly all states are accepted, also states that are later considered illegal. This allows the algorithm to explore the state space before converging on a minimum. Furthermore, modifications to the basic simulated annealing schedule are made. When a large number of iterations have been performed without the current energy dropping below the all-time-lowest energy, the state is reset to the all-time-best state. The energy is plotted for two optimisations in Figure 7.7. Note, that states with higher energies than the old state are accepted, but the probability of this is lessened as a function of the iteration number. The optimisation terminates after a fixed number of iterations or if the all-time lowest energy has not been changed for a large number of iterations.

The weights, α, β, and γ, mentioned in Section 7.2.2 have been found by trial and error. Moreover, the optimisation step is repeated, each time with a different parameter configuration. A parameter configuration is called an *optimisation mode*. Initially, the optimisation is run until convergence with $\alpha = 0.8$, $\beta = 0$ and $\gamma = 0.1$, giving $\mathcal{F}_{\text{total}} = 0.72\mathcal{F}_{\text{col}} + 0.18\mathcal{F}_{\text{dist}} + 0.02\mathcal{F}_{\text{area}}$. This mode allows minor collision, while focusing on minimising the faceplate area and pulling the faceplate towards the tympanic membrane. The energy plots in Figure 7.7 are generated using this mode. Finally, the state is optimised with a mode that penalises collisions hard : $\alpha = 1$, $\beta = 0$ and $\gamma = 0$, giving $\mathcal{F}_{\text{total}} = \mathcal{F}_{\text{col}}$.

In addition, simulated annealing is used in another context in Appendix C.

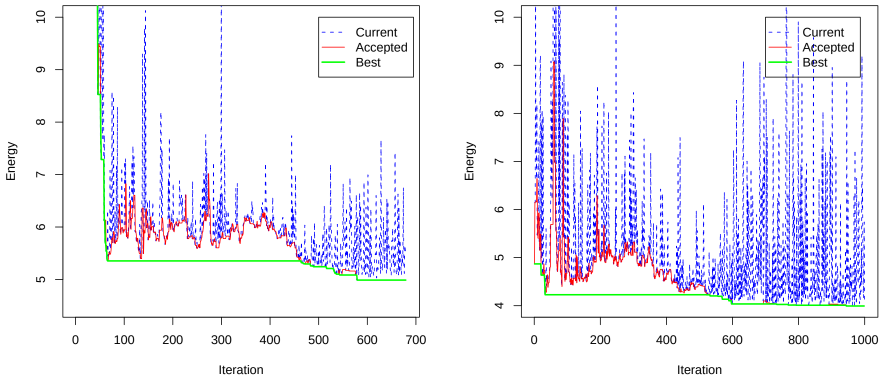

Figure 7.7: The total energy of a state plotted against the iteration number for two different optimisations. The energy for the current state, the energy for the accepted state, and the energy for the all-time-best state are shown.

7.2.7 Validation

Two experienced CIC operators (expert 1 and 2) have placed faceplates on a training set using a custom-made CAD tool. The toolkit is described in Appendix E.2. As an initial validation, the results produced by the algorithm are visually compared to the expert placements. Two examples are seen in Figures 7.8, 7.9, 7.10, 7.11, 7.12, and 7.13. Generally, the algorithm produces results that from a visual standpoint are comparable to a human operator. In example 1, seen in Figures 7.8, 7.9, and 7.10 the algorithm has placed the faceplate nearly in the same position as the two operators. A CIC produced with a faceplate in the computed position would have a high cosmetic quality. First, the shape of the faceplate is nearly oval. Secondly, the battery compartment point downwards. Finally, the faceplate is placed deep in the ear canal. Thus, it would be nearly invisible in-situ.

The algorithm has not performed equally well in example 2 seen in Figures 7.11, 7.12, and 7.13. Compared to the placement of the two operators, the algorithm has tilted the faceplate. The explanation can be found in Table 7.1, where the individual terms of the objective function have been calculated for the expert and computer placements. For example 2, the result of the algorithm is a placement with a smaller faceplate area and a shorter distance to the tympanic membrane than the placements of the two operators. If we assume that the operator placements are the *ground-truth*, it unfortunately indicates that the

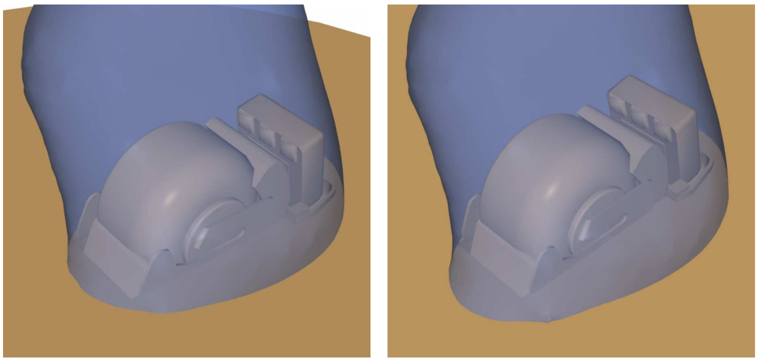

(a) Expert 1

(b) Expert 2

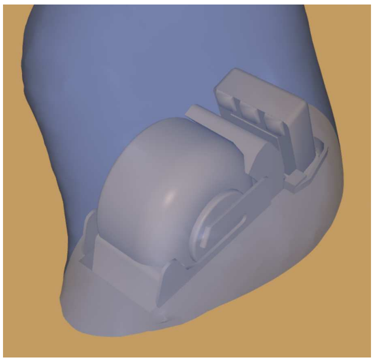

(c) Auto

Figure 7.8: Example 1 component view. The two expert operators and the algorithm have placed the components similarly. As seen in Table 7.1, there are minor hidden collisions between the shell and the components. However, the components are well inside the shell and there is not much excess space. Furthermore, the faceplate is placed nearly perpendicular to the shell. Thus, connecting the faceplate components to the remaining component would not be difficult.

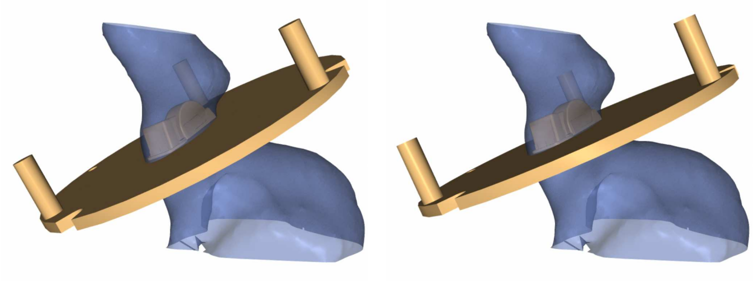

(a) Expert 1

(b) Expert 2

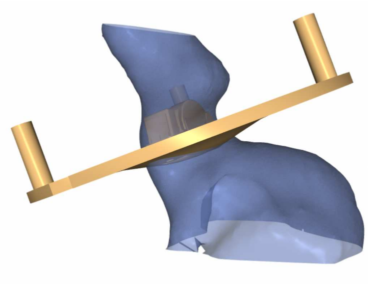

(c) Auto

Figure 7.9: Example 1 side view. Both the algorithm and the two operators have placed the faceplate near the first bend of the ear canal. Thus, the resulting CIC would sit deep in the ear canal.

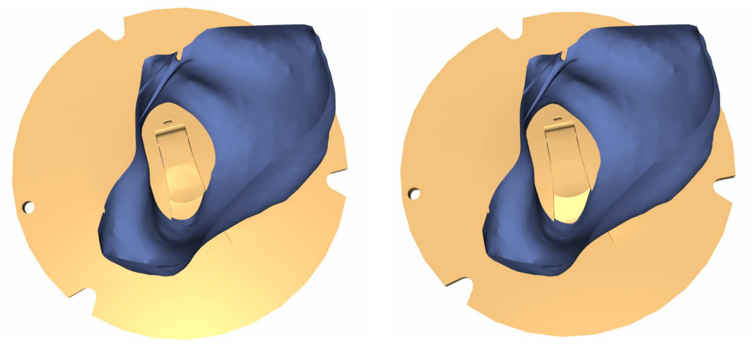

(a) Expert 1 (b) Expert 2

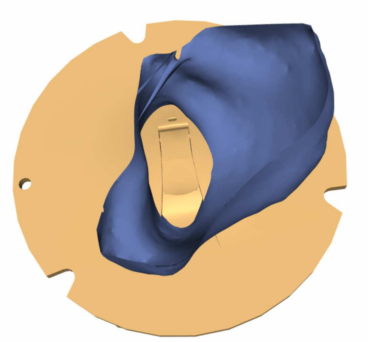

(c) Auto

Figure 7.10: Example 1 entrance view. The three placements are very similar. The resulting instrument would be a very small CIC. Furthermore, the battery-compartment door points downwards and the faceplate outline is oval, giving a cosmetically appealing finish of the hearing aid.

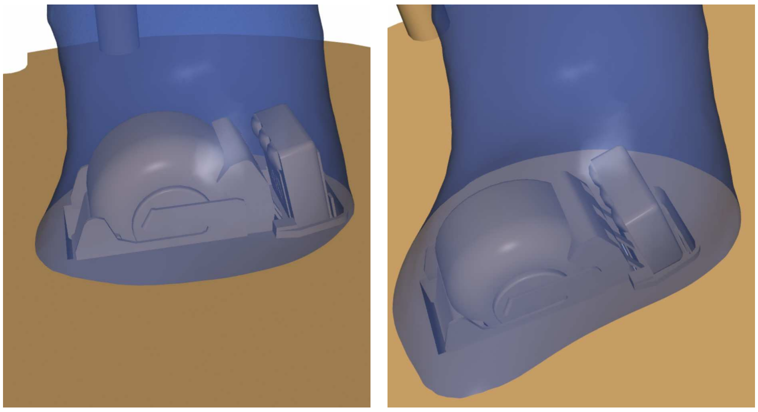

(a) Expert 1 (b) Expert 2

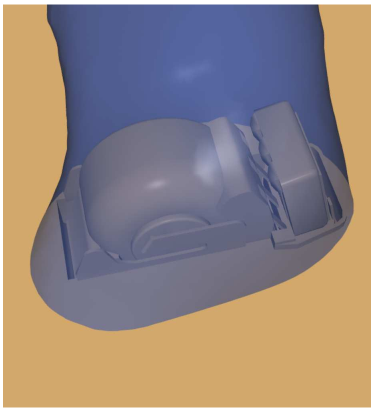

(c) Auto

Figure 7.11: Example 2 component view. It is easy to see the difference between the placements. While expert 1 has placed the component in a satisfactory position, expert 2 has placed them in a tilted position with too much excess space. The algorithm-placement is in between the two operators.

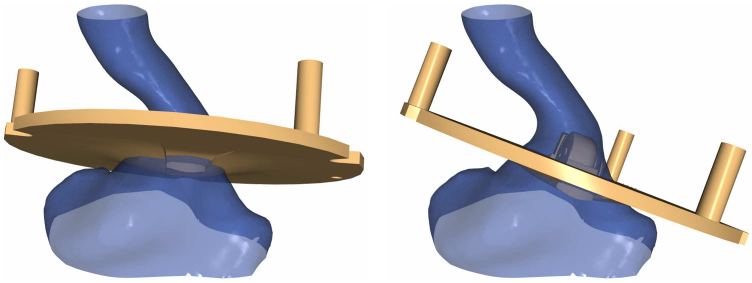

(a) Expert 1 (b) Expert 2

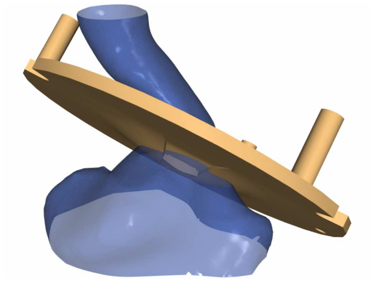

(c) Auto

Figure 7.12: Example 2 side view. From this angle, it is seen that the algorithm has placed the faceplate in a tilted position compared to the operators.

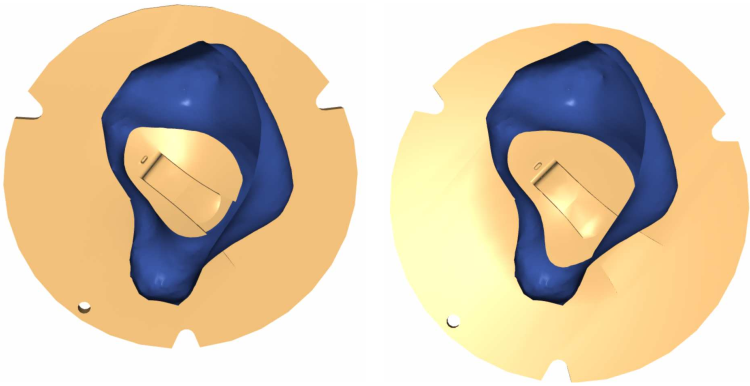

(a) Expert 1 (b) Expert 2

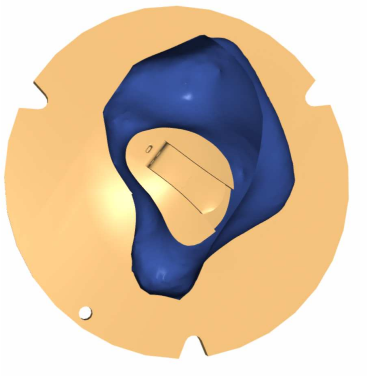

(c) Auto

Figure 7.13: Example 2 entrance view. It can be seen that both the expert operators and the algorithm have problems in placing the faceplate in a position that would result in a CIC with a high cosmetical value. First, the battery compartment points sideways. Secondly, the faceplate outline is not oval and tends to look like a *duck-foot*.

objective function lacks terms that describe more of the operator skills. However, neither the algorithm placement nor the expert placements would result in a CIC with a high cosmetic quality. First, the battery compartment does not point downwards. Secondly, the faceplate outline is not oval, but *duck-foot* shaped. In conclusion, it is not possible to build a good quality CIC for that given ear with this component configuration. The measurement of the cosmetical quality of a CIC is discussed in Section 8.3.

Experiments have shown considerable variation between operator placements. In addition, this is indicated in Table 7.1. However, the data currently available is insufficient to compare the intra-operator variance with the operator-machine variance.

		$\mathcal{F}_{\text{col}}$	$\mathcal{F}_{\text{area}}$	$\mathcal{F}_{\text{dist}}$	$\mathcal{F}_{\text{total}}$
Example 1	Expert 1	1.47	**82.15**	13.59	5.14
	Expert 2	5.20	85.14	13.23	7.83
	Auto	**0**	88.14	**12.46**	**4.01**
Example 2	Expert 1	**0**	109.03	20.23	5.82
	Expert 2	**0**	134.18	21.64	6.58
	Auto	**0**	**108.42**	**20.21**	**5.81**
Example 3	Expert 1	0.04	109.15	16.64	5.21
	Expert 2	**0**	113.43	17.20	5.37
	Auto	**0**	**104.22**	**16.41**	**5.04**
Example 4	Expert 1	0.03	138.80	**14.05**	5.33
	Expert 2	**0**	105.23	15.07	4.82
	Auto	**0**	**96.96**	14.84	**4.61**
Example 5	Expert 1	1.72	115.50	**18.74**	6.92
	Expert 2	**0**	142.82	20.14	6.48
	Auto	**0**	**99.51**	18.75	**5.37**
Example 6	Expert 1	2.56	**87.45**	**15.14**	6.31
	Expert 2	**0**	90.70	15.39	**4.58**
	Auto	**0**	100.12	15.69	4.83
Example 7	Expert 1	0.51	89.94	14.68	4.80
	Expert 2	1.00	**87.75**	14.53	5.09
	Auto	**0**	92.01	**12.72**	**4.13**
Example 8	Expert 1	**0**	78.40	15.73	4.40
	Expert 2	1.82	**78.12**	**7.84**	4.28
	Auto	**0**	79.95	11.96	**3.75**

Table 7.1: Placement scores. The best score in each category is marked with bold. Collision detection was not enabled during the operator placement. Therefore, minor collisions between the shell and the components occur in certain expert placements. For all examples except one, the algorithm finds the placement with the lowest total score.

In conclusion, the objective function is a limited approximation of the thoughts and skills of the operators. Adding terms to the objective function could probably alleviate the problems encountered.

Finally, a visual interface to the placement algorithm has been made. We have used it to validate and tune the optimisation. It is described in Appendix E.3.

7.3 Discussion

In this section, a complete framework for component placement has been presented and applied to the task of placing a faceplate in an ear canal.

The aim was to produce a system that can mimic the craftsmanship of the best human operator. As demonstrated, the algorithm is able to produce results that are comparable to the human results, even though it was realised that the objective function needs additional terms.

Simulated annealing was chosen for the optimisation. Better performance could probably be achieved by merging simulated annealing with a gradient-descent based method.

In-vivo validation of the results would be optimal. However, this is currently not possible, since the method is not yet mature enough to produce the data needed for a rapid-prototyping machine. Furthermore, the remaining components have been ignored in this implementation.

The method is completely automatic. Given a newly scanned ear canal, the algorithm recognises it, places anatomical relevant landmarks, and finally locates an optimal faceplate placement.

In conclusion, we regard the results as a proof-of-concept of automated component placement in the production of CIC hearing aids.

Chapter 8

Other Applications

This chapter presents various applications where the results from the other parts of the thesis have been used.

8.1 A One-Size-Fits-Most Shell

Attempts have been made to produce CIC hearing aids with a fixed design that fits a large percentage of the population [190, 249]. One type of these hearing aids is equipped with a soft disposable outer sleeve [148].

During the thesis, a research project in Oticon required in-vivo testing of a component configuration using several test subjects. Producing a custom CIC for each test-subject would be very cumbersome. Instead, we attempted to produce a one-size-fits most shell using the methods and results from the statistical shape model. The shell should be able to fit into as many ear canals as possible while still providing adequate comfort. The approach is based on the concept of a *minimum shell*. It is not produced with a specific set of components in mind. Hence, in addition to being used in the above-mentioned experiment, it can serve as inspiration for future component design.

The minimum shell is computed based on a training set of scanned ear impressions. The shape model described in Appendix A can synthesise ear canals that exhibit the shape variation found in the population from which the training data come. Thus, the training set used to compute the minimum shell could be composed either of the entire training set or a set of synthetic ear canals. A minimum canal computed using the synthesised ear canals should theoretically fit the percentage of the standard population specified when synthesising the ear canals. The selection of the training set has no influence on the following steps. In the following, the total training set of 29 shapes is used, thus creating a minimum canal that fits into all ear canals in the training set. Hence, the ear canals are represented as dense meshes with point correspondence. The dense correspondence is created using the method described in Appendix A.

Initially, the ear canals are Procrustes aligned [111] as seen in Figure 8.1. We need to calculate the shell that can be placed inside the aligned canals without interference.

The Procrustes average mesh is used as the initial guess of the minimum shell. Obviously, it contains the same number of vertices as the aligned ear canals. The normals are calculated for the mesh by determining normals for each polygon and then averaging them at shared vertices [219]. The mesh is then deformed by pushing the vertices in the direction of their normal vectors. The algorithm can be seen in algorithm 1. Since the normals are pointing outwards, $t_{\min}$ will be negative or equal to zero.

Algorithm 1 Calculating a minimum canal

```
The minimum shape is initially set equal to the Procrustes average shape
The normals for the minimum shape are calculated
for all vertices $\mathbf{p}$ on the minimum shape do
  for all shapes $S$ in the training set do
    calculate the vector $\mathbf{v}$ from $\mathbf{p}$ to the corresponding vertex on $S$
    calculate the projection $t$ of $\mathbf{v}$ on the corresponding normal $\mathbf{n}$ on the minimum shape, $t = \mathbf{v} \cdot \mathbf{n}$
    store the minimal projection value $t_{\min}$
  end for
  move $\mathbf{p}$ to $\mathbf{p} + t_{\min}\mathbf{n}$
end for
```

The resulting minimum shell can be seen in Figure 8.2. The approach is similar to offsetting the initial surface with a non-uniform offset. Using the surface normals to generate offset surfaces tend to create artefacts as further explained in Section 6.4. However, no artefacts were detected on the minimum shell and the result is of a sufficient quality for our use.

Finally, the minimum shell is cut with two planes. The first cut-plane is placed

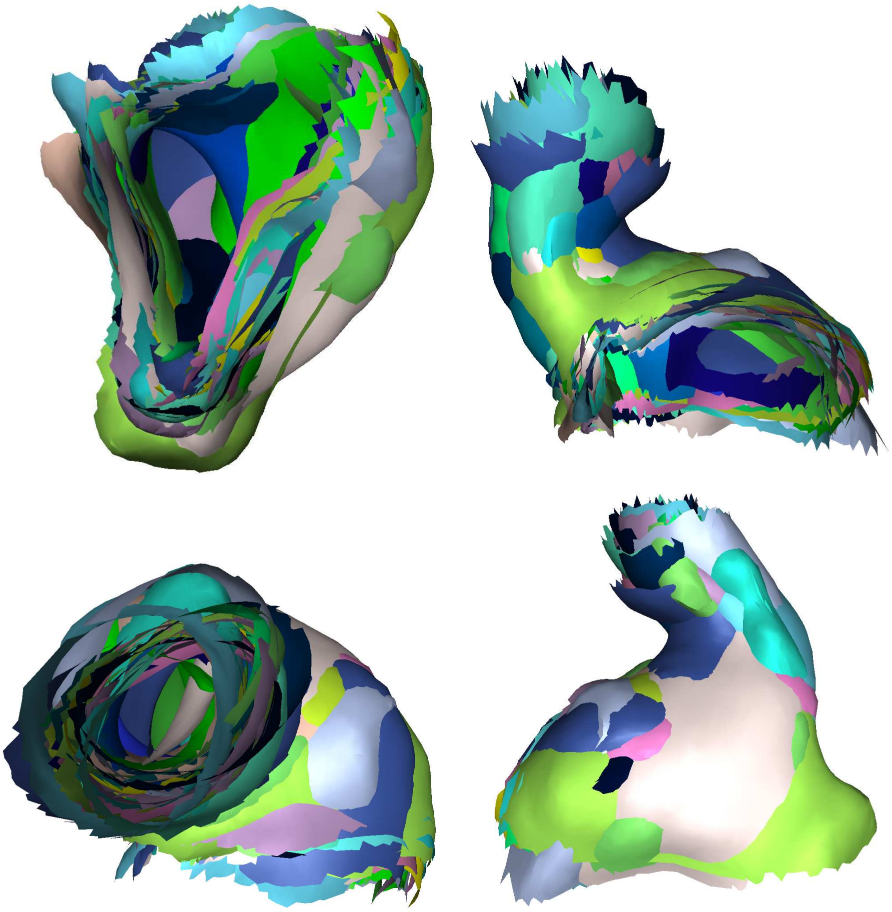

Figure 8.1: Procrustes aligned ear canals.

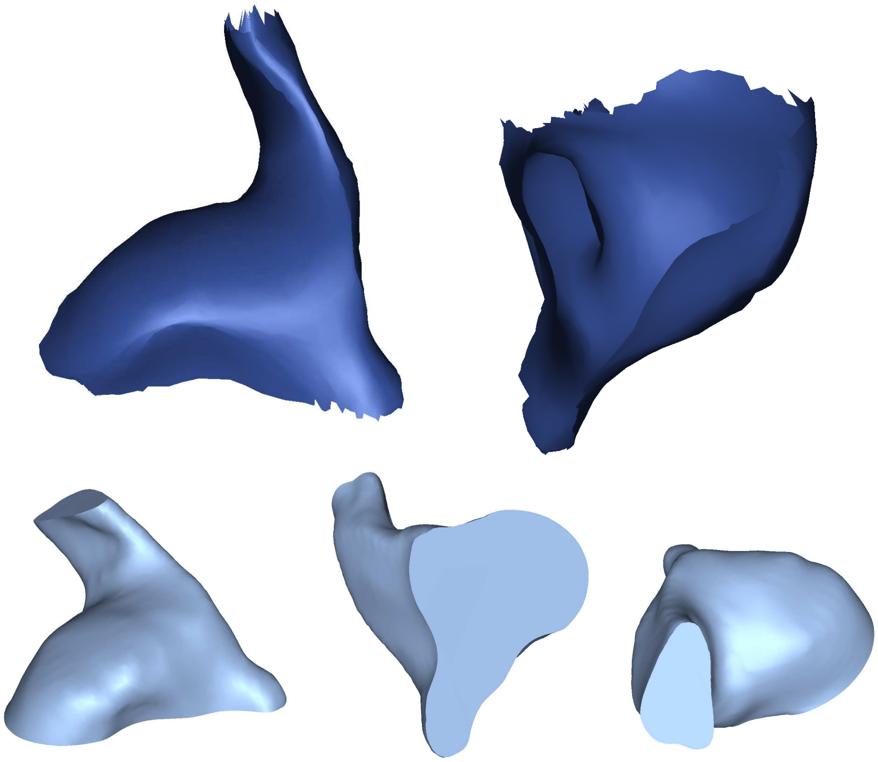

Figure 8.2: The minimum shell represented as a surface and as a solid block.

at the second bend of the ear canal. This position is found by landmark-propagation from the annotated model mesh. This is described further in Section 4.2.4. The second cut-plane is manually placed at the entrance to the ear. The position is chosen so the interior volume of the shell is maximised and there are no gaps in the intersection between the shell and the cut-plane.

The physical minimum-shell has been produced by an SLA machine. Thickness is added to the uncut minimum shell by the shelling algorithm described in Section 6.4 and the result can be seen in Figure 6.8 on page 61. Finally, the shell was cut and printed as seen in Figure 8.3. The shell has been used in experiments with various component configurations. It turned out that a large group of people can use the minimum shell, if it is used in combination with a soft earplug.

In order to produce a CIC from the minimum shell, a custom faceplate is used. In addition, a tipplate is mounted. While it is possible to generate a rounded tip on the shell before printing, the tipplate is used to facilitate the testing of different component configurations.

Figure 8.3: SLA print of the minimum shell with the faceplate, tipplate, and components added.

8.2 Checking Insertability

When a CIC hearing aid is produced using the traditional method, it is continuously checked against a rubber replica of the ear canal. This is illustrated in Section 2.3. Similarly, when a CIC hearing aid is produced using the new digital approach, there is an equal need for testing the insertability of the hearing aid. Thus, a measure of how difficult it is to insert the CIC in the ear canal is needed.

Insertability is related to path planning. Hence, the *path of least resistance* described in Section 6.3 can be used to simulate the insertion of a CIC as seen in Figure 8.4. The CIC follows the path by aligning its principal axis to the tangent vector of the closest point on the path. This alignment allows a rotation about the axis. The rotation that minimises the collision can be found by using the collision detection routine described in Section 6.2. The insertability is evaluated as the amount of collision between the CIC and the ear canal during the insertion.

Due to lack of data, we have not been able to study this problem in depth. However, preliminary results indicate that the method is sound. Achieving a true simulation of the insertion performed by the hearing aid user, would probably require a coupling with the simulation framework presented in Chapter 7.

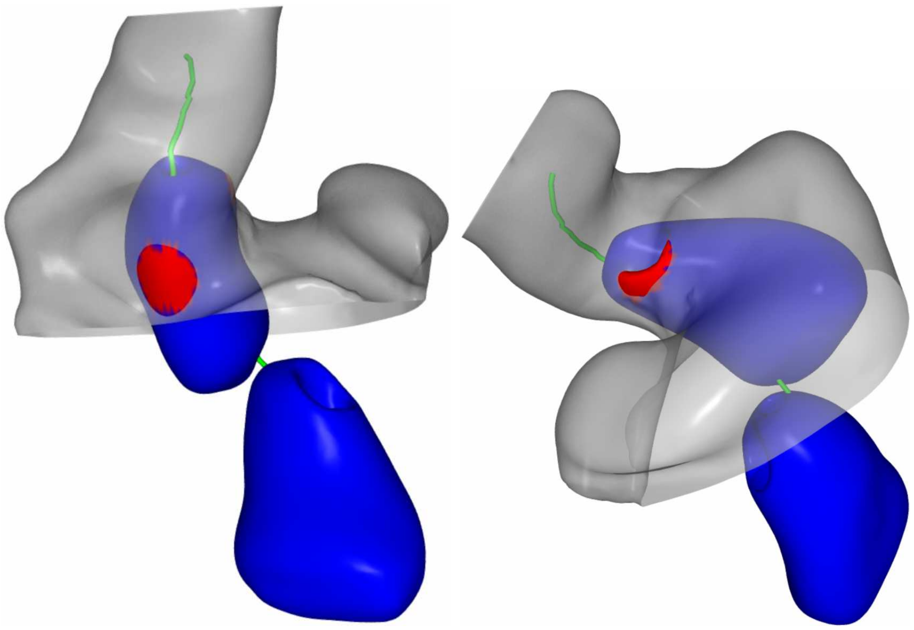

Figure 8.4: Insertion of a CIC in an ear canal. The CIC follows the path of least resistance shown as a green tube. Collisions between the CIC and the ear canal are indicated with red.

8.3 Classification of Hearing Aid Usability

When designing components for a new line of CIC hearing aids, the following question is always posed:

> Given a faceplate and a set of components, what percentage of a population can be successfully fitted with CIC hearing aids, assuming that a custom shell is made for each ear?

Today this would be answered by manually fitting a prototype of the components into a large set of shells. Hence, it is a time consuming and cumbersome task. While the introduction of the digital production technology means that this can be done using software, an operator is still needed to place the components and validate the results.

It is obvious, that the component placement framework demonstrated in Chapter 7 can be useful in this respect. Hence, a prototype faceplate can be automatically placed in an ear canal approximately as an expert operator would. However, an objective measure of *successful fitting* is needed to evaluate if the resulting CIC instrument is acceptable. An example of a succesful fit can be found in Figure 7.10 on page 77 and an example of a non-optimal fit can be seen in Figure 7.13 on page 80.

In summary, we would like to be able to compute a *usability score* (US) for a given component configuration. The US should measure how well the component configuration fits into a single ear. Furthermore, a US should be given for how well the component configuration fits into a selection of ear canals. It can be formulated like this:

> Given an ear and a CIC produced for that ear canal, calculate the usability score for that particular CIC in that ear.

It is obvious, that the US should be based on geometrical measurements of the finished hearing aid. However, it is also obvious that these measurements should be coupled with the anatomy of the actual ear canal. Intuitively, the area of the faceplate is an important factor in the cosmetics of the hearing aid. However, it is not possible to use the raw area as an objective quality measure, since a hearing aid made for a large ear canal, can be very good even though it has a large faceplate.

The general idea in this thesis is that the expert operators posses the needed knowledge. Hence, the goal is again to mimic the decisions made by the best human operators. We are applying learning-based methods to search for the solution. Thus, a training set is needed. Finding a training set consisting of well-placed and not-so-well placed component configurations was not possible. Instead, another approach was used. As described in Chapter 7 a training set with expert placed faceplates exists. This training set is extended to include not-so-well placed faceplates. For each ear canal, two non-optimal faceplate placements that are often seen in the production were made by expert 1. The first is the so-called *duck-foot* position that induces an irregular *duck-foot* shaped faceplate. The second is a tilted position, where the faceplate is tilted when compared to the optimal placement. An example of the three different placements can be seen in Figure 8.5. In summary, the goal is to find a score function that can classify the training set.

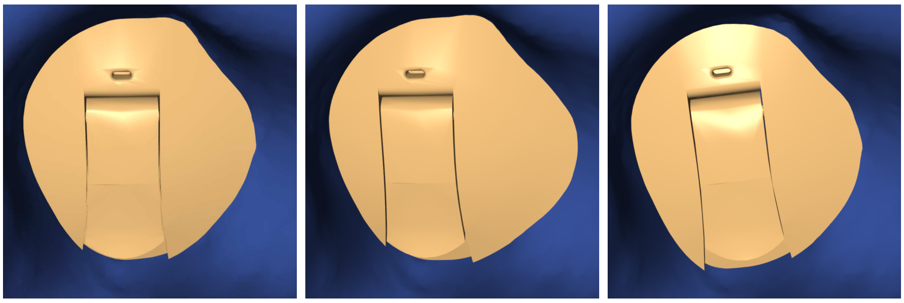

(a) Example 1

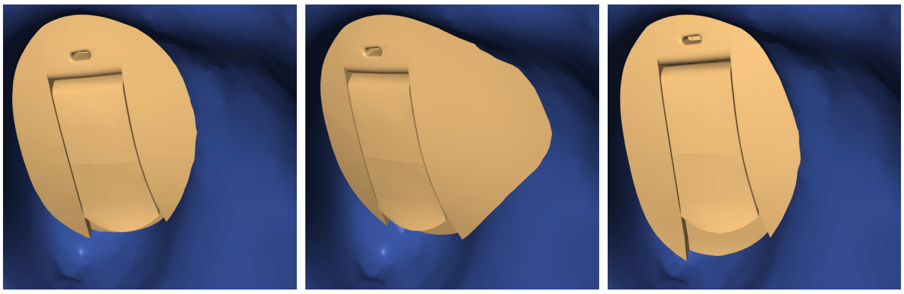

(b) Example 2

Figure 8.5: Faceplate placements for two examples. From left to right: optimal, duck-foot, and tilt.

Initially, the shape and size of the faceplate cut is examined. There is a clear difference in the shape of the faceplate outlines as seen in Figure 8.6. Furthermore, a plot of the faceplate areas for the training set can be seen in Figure 8.7a. While there is a clear difference between the average optimal-faceplate area and the average duck-foot-faceplate area, there is still an overlap. Hence, it is possible to determine if one faceplate position is more duck-foot than another. However, the faceplate area is not enough to determine the level of *duck-footedness* of a single faceplate.

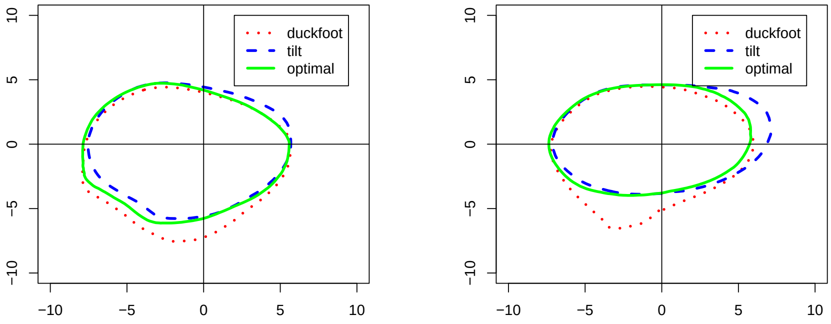

(a) Example 1 (b) Example 2

Figure 8.6: Faceplate outlines for the two examples shown in figure 8.5.

An obvious idea is to compare the faceplate area with the cross-sectional areas of the ear canal. In Figure 8.7b the cross areas for the training set can be seen. They are measured at the first bend, the second bend, and at the position of the pure faceplate. The concept of the *pure faceplate* is explained in detail in Appendix D. Furthermore, the anatomy of the ear canal and the positions of the first and second bend are described in Section 2.1.

However, it has not been possible to find a combined measure with the desired properties. This is mainly due to insufficient time. Nevertheless, we believe that the approach is feasible and that it is possible to find a combination of anatomical and geometric features that provides the solution.

8.4 Discussion

While the methods described in this chapter do not constitute a closed framework, we believe that the underlying ideas are interesting and can serve as a basis for future research.

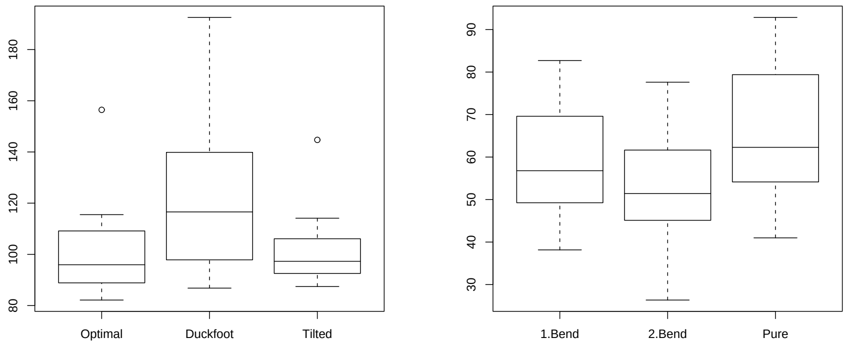

(a) (b)

Figure 8.7: a) Faceplate areas for the training set. b) Cross-areas for the training set. They are measured at the first bend, the second bend, and at the position of the pure faceplate.

The in-vivo testing of the minimal shell gave very positive results. Hence, it is proved that the work done has not solely been an intellectual exercise, but that the results can actually be used in the industry. This is very encouraging.

Part III

Conclusion

Chapter 9

Discussion and Conclusion

This thesis has described the statistical shape modelling of the human ear canal and how this model can be used in the mechanical design of hearing aids. This final chapter summarises the contributions and ends with the conclusion.

9.1 Contributions

The first result of this thesis is the building and testing of a statistical shape model of the human ear canal. It is mainly a proof-of-concept and a specification of a framework, since the model is built and tested with a small dataset. Hence, it is not a population study, but the model can easily be extended with more data.

We realised that the initial shape model contained flaws due to the method used to generate correspondence. Smoothing of the vector field alleviated this problem. Furthermore, it turned out that the approach could be formulated in a Markov Random Field framework. Hence, a new flexible framework for non-rigid registration of 3D surfaces was developed.

The primary focus in this thesis has been to develop software tools that can mimic the craftsmanship of the best completely-in-the-canal hearing aid operators. The first result in that direction is the shape model guided pure faceplate placement. Hence, an initial proof of the usability of the shape model in the hearing aid production was achieved.

Furthermore, a generic component placement framework has also been presented and applied to the placement of the faceplate and the associated components. The results from the shape model were used extensively in this framework. In short, the method was demonstrated to able to reproduce the results of expert operators. Thus, the coupling of shape modelling and stochastic optimisation has proven successful.

We have produced prototype software tools to demonstrate the algorithms. Evidently, the algorithms should be incorporated in an existing commercial framework to maximise the usability.

Finally, a physical proof of the validity of the ideas presented in the thesis was produced in the form of a one-size-fits-most shell.

9.2 Discussion

During the course of this study, several inexpensive scanners, dedicated to the scanning of hearing aids have appeared. In addition, the commercial software tools to design hearing aids digitally have become increasingly more advanced and user-friendly. Hence, the focus of this thesis needed constant adjustment. We have aimed at using results from the commercial packages maximally, and have in this way taken care not to reproduce the methods already implemented in the industry.

While the project progressed and the proof-of-concept of shape modelling of the ear canal was achieved, we got inspiration and motivation for additional studies. An obvious idea is to study the dynamic shape change of the ear canal when a person is speaking, chewing, or yawning. However, this type of data is not yet available, but we are certain that the shape-modelling framework can be applied to this analysis. In addition, the study of the growth of the ear canal is extremely important.

9.3 Conclusion

Oticon celebrates its 100 years anniversary this year. Thus, hearing aid production is a highly refined process that has been gradually improved over nearly a century. Furthermore, many operators have worked with hearing aids for more than 25 years and posses a wealth of accumulated knowledge.

In this light, it would be foolhardy to assume that a single thesis will be able to change and revolutionise this established system. When that is said, we still believe that the outcome of this thesis is a new and original approach to the mechanical hearing aid design and production.

To our knowledge, it is the first example of a system that uses statistically based knowledge about the shape variation of biological objects in product design and manufacturing.

We believe that the introduction of digital production methods will result in a more optimised production and more uniform quality of products. However, operators will still be needed for validation, but the algorithms presented may aid the inexperienced operators to achieve better results.

Appendix A

Building and Testing a Statistical Shape Model of the Human Ear Canal

Rasmus R. Paulsen, Rasmus Larsen, Søren Laugesen,
Claus Nielsen, and Bjarne K. Ersbøll

Abstract

Today the design of custom in-the-ear hearing aids is based on personal experience and skills and not on a systematic description of the variation of the shape of the ear canal. In this paper it is described how a dense surface point distribution model of the human ear canal is built based on a training set of laser scanned ear impressions and a sparse set of anatomical landmarks placed by an expert. The landmarks are used to warp a template mesh onto all shapes in the training set. Using the vertices from the warped meshes, a 3D point distribution model is made. The model is used for testing for gender related differences in size and shape of the ear canal.

A.1 Introduction

Hearing aids come in a number of different styles. The smallest of these styles is called CIC (Completely In the Canal). A CIC hearing aid consists of an acrylic shell containing microphone, amplifier, loudspeaker, and battery. It is placed completely in the ear canal rendering it invisible to an observer viewing the bearer from the front. This is cosmetically appealing, and a number of acoustical advantages are also given. A CIC is produced for the individual patient based on a silicon mold of the ear canal.

It is obvious that the space available inside a CIC hearing aid is severely limited. Hence, both the design of the internal components of the CIC and the placement and orientation of these are very critical as to whether it is actually possible to build a CIC for a given ear. Today the aforementioned designs are based on the experience and skills of the mechanical engineers in the hearing aid industry and a general knowledge about the anatomy and geometry of the ear. It is acknowledged that systematic knowledge of the geometry of ear canals and the variation thereof potentially could be extremely helpful in the mechanical design of new components for hearing aids.

To our knowledge no systematic description of the variation of the human ear canal across a population exists. Measurements of the anatomy of a single ear canal have been made for the purpose of prediction of sound-pressure level distribution [234]. Manufacturers of hearing aids have made initial testing of rapid prototyping of hearing aid shells using laser scans of ear impressions but have not performed statistical analysis of these. It is obvious that the systematic description of the variation of the shape of the ear canal must be done using statistical methods. In recent years shape analysis has been used in the description, identification and segmentation of biological shapes.

A popular method for building shape models is the Active Shape Model method by Cootes et al. [61]. It is dependent of corresponding landmarks placed on the shapes in the training set. Most previous approaches to automated and semiautomated landmark generation and registration of 3D-surfaces use the local surface geometry. Examples of this are the non-rigid registration technique by Feldmar and Ayache [94], the local geometry and surface geodesic approach by Wang et al. [251] and the surface signature technique by Yamany et al. [257]. A method for automatic landmark generation based on a symmetric version of the iterative closest point algorithm is presented in [40]. However, this method is dependent on the global variation of the shape and apparently does not handle boundary areas or areas that are not well defined for all shapes.

In this project the ear canals are represented as 3D-surfaces constructed by a laser scanner. The local surface geometry of the ear canals varies much from one individual to another and therefore only very few ridges and extremal points are stable when comparing groups of ear canals. The surfaces of the ear canals are not closed due to the opening of the ear canal and because the ear impressions are terminated in front of the eardrum. Automatic landmark generation and correspondence is therefore difficult to establish with methods based on surface geometry.

We have chosen to base our method on the assumption that it is possible to place anatomical landmarks on the ear canal. The anatomical landmarks do not constitute an exhaustive description of the surface of the ear canal and it is therefore necessary to generate a more dense set of landmarks describing the shape. Interpolating landmarks is straightforward in 2D, but in 3D no spatial ordering of landmarks is usually defined and therefore the interpolation is much more difficult.

A landmark based approach is found in [184] where a template mesh is deformed to each shape in the training set using a thin plate spline transformation based on the annotated landmarks. This is followed by a regularisation step where each vertex of the template mesh is adapted to the current shape without causing folds. This method is well suited for closed surfaces since it does not incorporate the possibility that patches of the surface are not well defined on all shapes in the training set.

A similar approach is found in [143] with the addition that the method is able to handle surfaces with ill-defined areas. This is done by pruning the template mesh to only include the vertices that are well defined for all training shapes. In this method, the training shapes are warped to a template shape, and the correspondence is then made by projecting the vertices from the template shape to the warped training shapes. This is followed by an inverse warping of the adapted template shape, which gives the dense correspondence between the training shapes.

Our approach is similar to [143] but instead of warping each shape in the training set to the template mesh, the template mesh is warped to each shape in the training set eliminating the need for an inverse warp.

Other methods that could be well suited for the tubular-like ear canals are the spherical harmonics approach by Gerig [108] or the M-Rep approach by Pizer [207]. However, it is not clear how these methods will work on non-closed surfaces. A similar method that supports non-closed surfaces is the Fourier surfaces explored by Staib et al. [230].

A.2 Method

The data were collected by laser scanning of a set of 29 ear impressions taken from 20 male and 9 female subjects. The surfaces are reconstructed using the Power Crust [3]. Each reconstructed surface contains approximately 20,000 vertices and 35,000 triangles. An example of a scanned ear impression is seen in Fig. A.1. An anatomical description of the external ear and a formal naming convention used for ear impressions can be found in [2, 1].

A.2.1 Annotation of Anatomical Landmarks

Using a custom-made surface annotation tool the third author, who is an expert of the anatomy of the ear canal has annotated the 29 ear canals. 18 anatomical landmarks are placed on each ear canal. The landmarks constitute a sparse correspondence between the surfaces of the ear canals in the training set.

The surface of the ear canal is not closed and therefore it is necessary to identify the invalid areas. Planes that separate the valid parts of the surface from the invalid parts are defined for that purpose. In Fig. A.1 an ear canal with the anatomical landmarks and separating planes is seen.

A.2.2 Surface Correspondence Using Thin Plate Spline Warping

The anatomical landmarks do not constitute an exhaustive description of the surface of the ear canal and it is therefore necessary to generate a more dense set of landmarks describing the shape. For that purpose a template mesh is constructed and applied to all shapes in the training set.

The mesh constructed by the surface reconstruction contains far more vertices than needed to give a satisfactory shape description. To construct a template mesh that can be used as a basis for the further shape analysis a well defined ear canal surface is chosen and decimated by a standard algorithm [220].

The anatomical landmarks and the template mesh are used to establish a dense surface correspondence between the shapes in the training set. Since the template mesh is made from one of the actual ear canals in the training set anatomical landmarks of this mesh exist.

The template mesh is applied to each of the shapes in the training set using a Thin Plate Spline (TPS) warp based on the corresponding anatomical landmarks. TPS is a warp function that minimises the bending energy [34].

Since the TPS transform is only exact for the anatomical landmark locations, the vertices of the template mesh will not lie on the surface of the target shape. Finally, moving each vertex in the warped template mesh to the closest point on the target surface completes the dense correspondence. This introduces the risk of so called inversions, where the vertices of the template mesh shift place and cause folds in the mesh. Techniques to avoid this exist [7, 184] but it has not been necessary here.

When the template mesh is warped to another shape, it can happen that some points are placed outside the valid area on the target shape. When warped to each shape in the training set, the template mesh must only cover valid areas. This is accomplished by investigating whether any points from the template mesh are warped into the areas marked as invalid by the separation planes. The template mesh is then pruned to contain only the points that are warped to valid areas for all shapes in the training set. The template mesh contains 3,000 vertices after decimation and pruning.

When the dense correspondence has been established the connectivity of the pruned template mesh can be applied to the points of correspondence on each shape to yield a set of new meshes. It is now possible to dispose of the anatomical landmarks as well as the original meshes of the training set. The set of meshes with dense correspondence is used in the following statistical shape analysis.

A.2.3 Building the Point Distribution Model

The set of corresponding meshes are aligned by a generalised Procrustes analysis [113]. The pure shape model is built by using a similarity transformation in the Procrustes alignment while a rigid-body transformation is used to build the size-and-shape model [83].

Following the approach found in the Active Shape Model [61] a principal component analysis (PCA) is performed on the Procrustes aligned shapes. Each shape is represented as a vector of concatenated x, y and z coordinates $\mathbf{x}_i = [x_{i1}, y_{i1}, z_{i1}, \ldots, x_{in}, y_{in}, z_{in}]^T$, $i = 1, \ldots, s$, where n is the number of vertices and s is the number of shapes. The PCA is performed on the shape matrix $\mathbf{D} = [(\mathbf{x}_1 - \overline{\mathbf{x}})| \ldots |(\mathbf{x}_s - \overline{\mathbf{x}})]$, where $\overline{\mathbf{x}}$ is the average shape. The eigenvectors can be regarded as translation vectors that when added to the mean shape will deform the shape according to the modes of variation found in the training shapes.

A new shape exhibiting the variance seen in the training set is made by adding a combination of eigenvectors to the average shape $\mathbf{x}_{new} = \overline{\mathbf{x}} + \Phi\mathbf{b}$, where $\mathbf{b}$ is a vector of weights controlling the modes of shape variation and $\Phi = [\phi_1|\phi_2|\ldots|\phi_t]$ is the matrix of the first t eigenvectors. An arbitrary shape $\mathbf{x}'$ aligned to the Procrustes average can be approximated by the shape model by projecting the residuals from the average shape onto the eigenvectors $\mathbf{b} = \Phi^T(\mathbf{x}' - \overline{\mathbf{x}})$. The resulting parameter vector $\mathbf{b}$ is used in the statistical analysis below.

A.3 Results

A.3.1 General Observations

The three first modes of variation of the pure shape model are seen in Fig. A.2 and the average shape is seen in Fig. A.1. All the generated shapes look like real ear canals with no deformations or folds in the mesh. It is seen that the mode 1 deformation consists of a bending of the canal and a flattening of the concha part. Mode 2 explains some of shape variation seen in the inner part of the ear canal. Mode 3 is a combination of a flattening and twisting of the inner part of the ear canal and a general shape change of the concha.

The distribution of the modes against each other has been examined using pairwise plots, and no obvious abnormalities were found.

A.3.2 Classification of Surfaces

Testing the validity and usability of the shape model is done by examining its ability to reflect gender related differences in the size and shape of the ear canals.

It is first examined if there is a systematic gender-related difference in the centroid sizes of the ear canals. This test is performed using the centroid sizes of the dense surface meshes of the training set calculated prior to the Procrustes alignment. The centroid size is the square root of the sum of squared Euclidean distances from each landmark to the center of mass (the centroid) [83]. A standard t-test shows a highly significant difference in size between males and females ($p = 0{,}0003$). The gender related difference in size corresponds to 9% of the average centroid size.

Testing for a shape difference between genders is done using the vertices from the Procrustes aligned dense surface meshes from the pure shape model, meaning

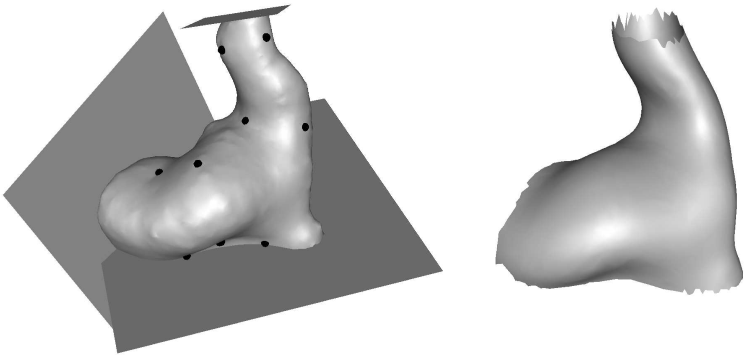

Figure A.1: To the left an example of a surface representation of an ear canal with the anatomical landmarks and the planes that separate the valid areas from the invalid areas. The thin structure in the top is the actual canal. The larger lower part is the concha. Only part of the concha is used and therefore a plane through concha is defined. To the right is the average shape from the pure shape model

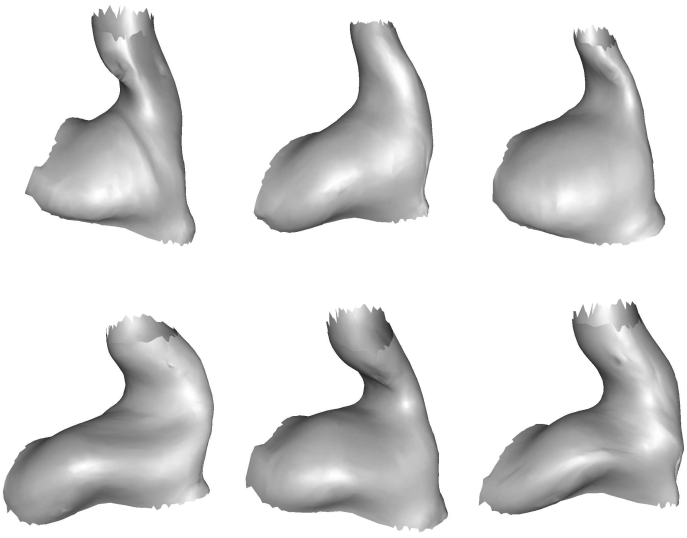

(a) Mode 1 (b) Mode 2 (c) Mode 3

Figure A.2: Pure shape model. Each shape has been generated by varying the first three modes of variation between −3 (top) and +3 (bottom) standard deviations that they are scaled to unit size. In this context, shape is thus unrelated to size. In order to avoid the problem of multiple testing (as would be the case for stepwise selection, for example) the following procedure is adopted. First the dimensionality is reduced by a principal component analysis as described earlier, secondly the number of components to retain is chosen, and finally a multivariate analysis of variance [154] is performed on these components. A typical method for determining the number of principal components to retain is to include just enough components to explain some arbitrary amount (typically 98%) of the variance. This criteria often results in far to many components being included in the further analysis and therefore Horn's parallel analysis [135] is chosen as a more objective way of deciding on how many components to include. The eigenvalues of the shapes are compared to those obtained for equivalent uncorrelated data, obtained by randomly scrambling each row in the shape matrix **D**. In this way, the number of modes to retain is 7 as seen on the scree-plot in Fig. A.3. A multivariate analysis of variance (which in this case is equivalent to Hotelling's T^2) of these 7 principal component scores per shape although not strictly significant (p=0,083) does indicate a shape difference between genders. Univariate analyses on the single principal components show that this is mainly due to the first mode of variation ($p = 0{,}0052$). This is also seen in Fig. A.3 where centroid size is plotted against mode 1 from the pure shape model. The exaggerated male-female mode shape variation is seen as the shape variation of mode 1 in Fig. A.2.

A.4 Summary and Conclusions

In this paper a method to generate dense surface distribution models of the human ear canal has been described. The generated models show consistency, and a large part of the variation found in the training data is explained by a small number of modes of variation. The method is general, and can be applied to all types of surfaces as long as it is possible to mark the valid areas of the surfaces and to place landmarks.

From an anatomical point of view it is interesting that the model is able to differentiate ear canals from males from ear canal from females based on both their size and their shape. The anatomical results based on this small data set are only strong enough to support general conclusions. For more detailed results a larger and more balanced data set is required.

The most important results of this paper are the proof-of-concept regarding the ability to build a meaningful statistical shape model of the human ear canal and that it is possible to describe a complex gender-related shape variation using a

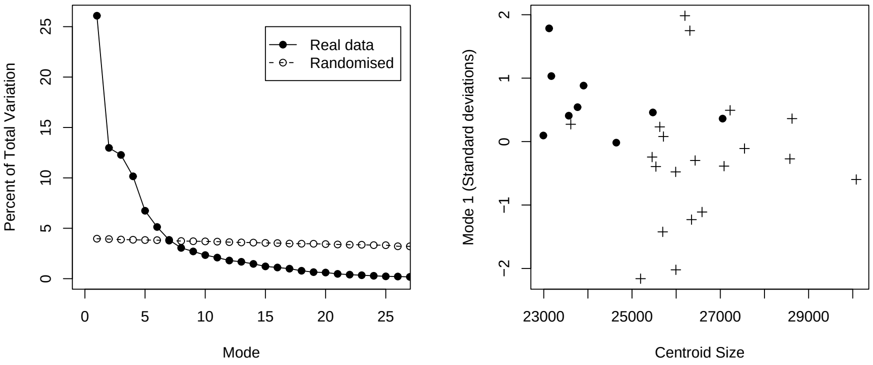

(a) Scree plot

(b) Size and shape plot

Figure A.3: To the left is a plot of the eigenvalues of the shapes from the pure shape model, compared to those for a randomised version of the data (each row of the shape matrix **D** was scrambled). The lines are crossing approximately where mode = 7. To the right is a plot of centroid size versus mode 1 from the pure shape model. The full dots are females while the plus signs are male. It is seen that both size and mode 1 separates males from females single parameter.

APPENDIX B

Shape Modelling Using Markov Random Field Restoration of Point Correspondences

---

Rasmus R. Paulsen and Klaus B. Hilger

Abstract

A method for building statistical point distribution models is proposed. The novelty in this paper is the adaption of Markov random field regularization of the correspondence field over the set of shapes. The new approach leads to a generative model that produces highly homogeneous polygonized shapes and improves the capability of reconstruction of the training data. Furthermore, the method leads to an overall reduction in the total variance of the point distribution model. Thus, it finds correspondence between semi-landmarks that are highly correlated in the shape tangent space. The method is demonstrated on a set of human ear canals extracted from 3D-laser scans.

B.1 Introduction

Point distribution models (PDMs) are widely used in modeling biological shape variability over a set of annotated training data [69, 61]. The generative models are highly dependent on the initial labeling of corresponding point sets which is typically a tedious task. Moreover, the labeling is often erroneous and sparse. A good representation of the training data is particularly hard to obtain in three dimensions. Finding a basis of homologous points is thus a fundamental issue that comes before generalized Procrustes alignment [113] and decomposition [178] in the shape tangent space.

A method for building a statistical shape model of the human ear canal is presented in [201]. An extension to this method is proposed in this paper using Markov Random Field (MRF) regularization for improving the initial set of point correspondences. The new approach leads to a more compact representation and improves the generative model by better reconstruction capabilities of the 3D training data. Related work include the application of Geometry Constrained Diffusion (GCD) [7, 6] and Brownian Warps [194] for non-rigid registration. A more compact model is obtained, since the shape tangent space residuals of the new representation have increased correlation. It thus indicates that a better correspondence field is obtained between the 3D semi-landmarks. Related work on obtaining a minimum description length of PDMs is proposed in [75, 76] based on information theoretic criteria.

The data consists of 29 3D ear canal surfaces extracted from laser scans of ear impressions. The local surface geometry of the ear canals varies much from one individual to another. Therefore, only very few ridges and extremal points are stable when comparing groups of ear canals. A set of 18 anatomical landmarks of varying confidence are placed on each ear canal, and constitute a sparse correspondence between the surfaces of the ear canals in the training set. The surfaces of the ear canals are not closed due to the opening of the ear canal and because the ear impressions are terminated in front of the ear drum. It is therefore necessary to identify the region of interest of each ear canal. Hence, planes are defined, which separates the valid parts of the surface from the invalid parts. In Fig. B.1, left, an ear canal with the anatomical landmarks and separating planes is shown.

The remaining paper is organized in three additional sections. Section 2 describes the proposed statistical method for improving the point correspondences. Section 3 presents the results of applying the extended algorithm. In Section 4 we summarize and give some concluding remarks.

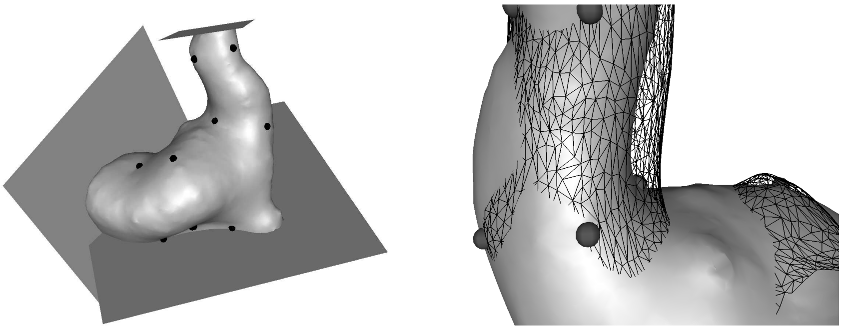

Figure B.1: Left: An example of a surface representation of an ear canal with the anatomical landmarks and the separating planes that defines the region of interest. The thin tubular structure in the top is the actual canal. The larger lower section is the concha, of which only the upper part is of interest. A cutoff plane through the concha is therefore defined. Right: The model mesh, shown by a wireframe, fitted to a target shape using Thin Plate Spline warping.

B.2 Methods

B.2.1 Surface Correspondence Using Thin Plate Spline Warping

The anatomical landmarks do not constitute an exhaustive description of the surface of the ear canal. It is therefore necessary to generate a more dense set of landmarks describing the shape. For that purpose a model mesh is constructed and fitted to all shapes in the training set. The model mesh is chosen as a decimated version of a natural well-formed ear canal labeled with the anatomical landmarks. The model mesh is fitted to each of the shapes in the training set using a Thin Plate Spline (TPS) warp based on the corresponding anatomical landmarks. TPS is a warp function that minimizes the bending energy [34]. Since the TPS transform is exact only for the anatomical landmark locations, the vertices of the model mesh will not lie on the surface of the target shape, see Fig. B.1, right. Projecting each vertex in the warped model mesh to the closest point on the target surface produces a non-rigid deformation field and generates a dense correspondence. However, using the Point to Surface Projection (PSP) introduces a critical risk of inversions, where the vertices of the model mesh shift place and cause folds in the mesh. Another secondary artifact is the non-uniformity of the correspondence vector field shown in Fig. B.2a,b giving rise to poor reconstruction of the target shape. In order to improve the correspondence vector field and avoid the problems inherent in applying point to surface projection a regularization must be included. Lorenz and Krahnstöver [184] propose a method for relaxing a polygonization into a more homogeneous representation, however, such methods are not suited when the polygonization is constrained to an underlying correspondence field. We propose to relax the problem by using a stochastic approach described in the following.

B.2.2 Markov Random Field Regularization

To obtain better reconstruction and correspondences we cast the problem of finding the deformation vector field into a Bayesian framework of MRF restoration. We thus follow the four successive stages of the Bayesian paradigm.

1: Construction of a prior probability distribution $p(\boldsymbol{d})$ for the deformation field $\boldsymbol{D}$ matching the source shape $\boldsymbol{S}_s$ onto the target shape $\boldsymbol{S}_t$.

2: Formulation of an observation model $p(\boldsymbol{y}|\boldsymbol{d})$ that describes the distribution of the observed shapes $\boldsymbol{Y}$ given any particular realization of the prior distribution.

3: Combination of the prior and the observation model into the posterior distribution by Bayes theorem

$$p(\boldsymbol{d}|\boldsymbol{y}) = p(\boldsymbol{y}|\boldsymbol{d})p(\boldsymbol{d})/p(\boldsymbol{y}). \tag{B.1}$$

4: Drawing inference based on the posterior distribution.

We start by some useful definitions from graph theory in order to describe a probability distribution on a spatial arrangement of points.

Given a graph of n connected sites $S = \{s_i\}_{i=1}^{n}$. A neighborhood system $\mathcal{N} = \{N_s, s \in S\}$ is any collection of subsets of S for which i) $s \notin N_s$, and ii) $r \in N_s \Leftrightarrow s \in N_r$, then N_s are the neighbors of s. A clique C is a subset of sites S for which every pair of sites are neighbors. We use $i \sim j$ to denote that i and j are neighbors. Given a neighborhood system $\mathcal{N}$ on the set of sites S we now consider the probability distribution of any family of random variables indexed by S, i.e. $\boldsymbol{D} = \{D_s|s \in S\}$. For simplicity we first consider a finite state space $\Lambda = 1, \cdots, L$ of $\boldsymbol{D}$ but later generalize to continuous distributions. Let Ω denote the set of all possible configurations $\Omega = \{\boldsymbol{d} = \{d_i\}_{i=1}^{n} \mid d_i \in \Lambda\}$. A random field $\boldsymbol{D}$ is a Markov Random Field (MRF) with respect to $\mathcal{N}$ iif i) $p(\boldsymbol{d}) > 0 \ \forall \ \boldsymbol{d} \in \Omega$, and ii) $p(d_s|d_r, r \neq s) = p(d_s|d_r, r \in N_s) \ \forall \ s \in S, \boldsymbol{d} \in \Omega$. The first constraint is the positivety condition and can be satisfied by specifying a neighborhood large enough to encompass the Markovianity condition in the second constraint.

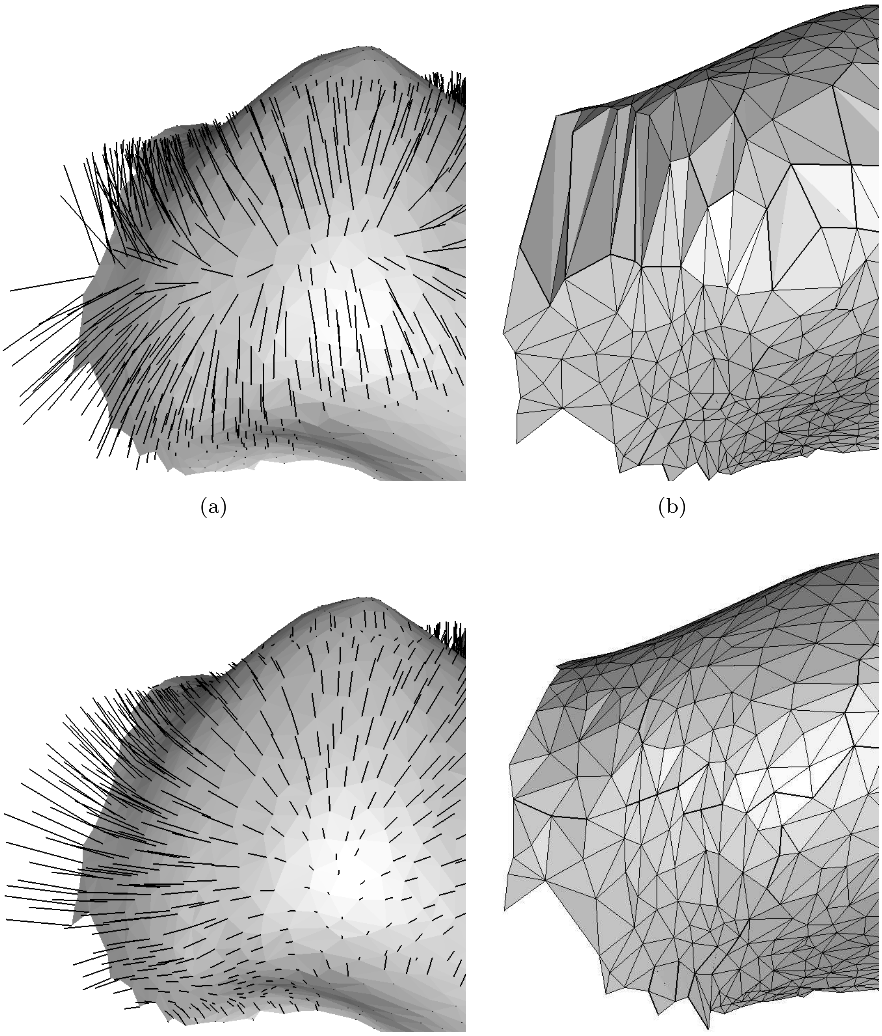

(a) (b)

(c) (d)

Figure B.2: **a**) The correspondence vector field derived using point to surface projection for moving the vertices of the source to the target shape. **b**) The resulting dense mesh representation of the target shape. **c**) The correspondence vector field derived using using the Markov random field restoration of the deformation field for moving the vertices of the source to the target shape. **d**) The improved dense mesh representation of the target shape.

Although the second condition is on the state of neighboring sites only, it does not exclude long range correlations in the probability distribution over the entire graph. Given a neighborhood system $\mathcal{N} = \{N_s\}$ let all cliques be denoted by $\mathcal{C}$. For all $C \in \mathcal{C}$ we assume that we have a family of potential functions V_C. We may now define an energy function of any given configuration of $\boldsymbol{d}$ i.e. $U(\boldsymbol{d}) = \sum_{C \in \mathcal{C}} V_c$. This leads to the definition of the Gibbs measure. The Gibbs measure induced by the energy function $U(\boldsymbol{d})$ is $p(\boldsymbol{d}) = \frac{1}{Z} \exp(-U(\boldsymbol{d})/T)$, where Z is the partition function and T is a parameter referred to as temperature. The Gibbs measure maximizes entropy (uncertainty) among all distributions with the same expected energy. The temperature controls the "peaking" of the density function. The normalizing constant may be impossible to obtain due to the curse of dimensionality but often we need only ratios of probabilities and the constant cancels out. The Hammersley-Clifford theorem gives the relation between MRF and Gibbs random fields and states that $\boldsymbol{D}$ is a Markov random field with respect to $\mathcal{N}$ iif $p(\boldsymbol{d})$ is a Gibbs distribution with respect to $\mathcal{N}$ [22, 106]. Thus the task is to specify potentials that induce the Gibbs measure in order encompass MRF properties of $\boldsymbol{D}$ on the graph.

So far the description only encompasses a one-dimensional finite state space. However, it generalizes to multivariate distributions since any high dimensional process may be recast into a single state space with $\prod_i L_i$ states, where L_i is the cardinality of the ith variable. Furthermore, the description generalizes to the case of continuous distributions in which case $\exp(-U(\boldsymbol{d})/T)$ must be integrable. Since we wish to model correspondence between $\boldsymbol{S}_s$ and $\boldsymbol{S}_t$ the displacements are bound to the surfaces, in effect only posing constraints on the length of the three dimensional displacements at the individual sites. In practice the constraint may be enforced by projection of the displacements onto the closest point of the target surface in every site update of the MRF relaxation.

B.2.3 Prior Distributions

Similar to pixel priors [24] we construct energy functions based on differences between neighboring sites. Extending to the multivariate case we get the general expression of the energy governing the site-priors

$$U_{\text{site}}(\boldsymbol{d}) = \sum_{i \sim j} ||\boldsymbol{d}_i - \boldsymbol{d}_j||_p^p \tag{B.2}$$

where $|| \cdot ||_p$ is the p-norm, $1 \leq p \leq 2$, and $\boldsymbol{d}_i$ represents the multivariate displacement in the ith site.

With $p = 2$ the energy function induces a Gaussian prior on the deformation field. Neglecting regions with strong surface dynamics the local optimization becomes convex and the maximum likelihood (ML) estimate of the displacement at the ith site is taken as the mean of the neighboring displacements. By applying a weighted average

$$\hat{\boldsymbol{d}}_i = \sum_{j \in N_i} w_i \boldsymbol{d}_j / \sum_{j \in N_i} w_j \tag{B.3}$$

and using Gaussian weights, derived from a fixed kernel size, the maximum a-posteriori (MAP) state-estimate of the MRF is similar to the steady state of the algorithm for geometry constrained diffusion (GCD). GCD of $\boldsymbol{D} : \mathbb{R}^3 \rightarrow \mathbb{R}^3$ mapping the surface $\boldsymbol{S}_s$ onto the surface $\boldsymbol{S}_t$ is given in [7] by

$$\partial_t \boldsymbol{D} = \left\{ \begin{array}{cl} \Delta \boldsymbol{D} - \boldsymbol{n}_{S_t} \frac{\boldsymbol{n}_{S_t}^T \Delta \boldsymbol{D}}{||\boldsymbol{n}_{S_t}||^2} & \text{if } \boldsymbol{x} \in \boldsymbol{S}_s \\ \Delta \boldsymbol{D} & \text{if } \boldsymbol{x} \notin \boldsymbol{S}_s \end{array} \right. \tag{B.4}$$

where $\boldsymbol{n}_{S_t}$ is the unit surface normal of $\boldsymbol{S}_t(\boldsymbol{D}(\boldsymbol{x}) + \boldsymbol{x})$. Thus, GCD is numerical scheme for solving a space and time discretized version of the heat equation on the deformation field with certain boundary conditions. Notice that in the MRF formulation we explicitly constrain the correspondence problem on the source and target surfaces, whereas the GCD implementation works on volume-voxel diffusion.

Abandoning homogenity and isotropy of the MRF non-global kernels may be introduced. Thus, adaptive Gaussian smoothing may be applied, e.g. by setting the standard deviation of the kernel to the square-root of the edge length of the closest neighbor of site i on the graph. Moreover, using the $p = 1$ norm induces a median prior, with the ML estimate being the median of the displacements at the weighted neighboring sites. This property makes the MRF attractive for correspondence fields with discontinuities, thus avoiding the smearing of edges attained by the Gaussian prior.

B.2.4 Observation Models

Given a realization of the prior distribution, the observation model $p(\boldsymbol{y}|\boldsymbol{d})$ describes the conditional distribution of the observed data $\boldsymbol{Y}$. By specifying an observation model we may favor a mapping that establish correspondences between regions of similar surface properties. The similarity measures may include derived features of the observed data such as curvature, orientation of the surface normals, or even texture.

The simple dot product between the normals may form the basis for specifying a governing energy function that favors correspondence between regions of similar orientation by

$$U_{\text{norm}}(\boldsymbol{y}|\boldsymbol{d}) = \sum_i ||\boldsymbol{n}_{S_s,i}^T \boldsymbol{n}_{S_t,i} - 1||^q, \tag{B.5}$$

where $\boldsymbol{n}_{S_s,i}$ is the surface normal at location $\boldsymbol{x}_i$ on the source $\boldsymbol{S_s}$, and $\boldsymbol{n}_{S_t,i}$ is the normal of the target surface $\boldsymbol{S_t}$ at the coordinate $\boldsymbol{x}_i + \boldsymbol{d}_i$. The parameter $q > 0$ controls the sensitivity of the energy function.

B.2.5 Maximum a Posteriori Estimates

Normalization of the energy terms from the different prior and observation models is typically chosen such that they operate on the same domain. However, the data analyst may choose to favor some terms over others, e.g. by relaxing the smoothness conditions in favor of correspondences between regions of similar curvature orientation of the surface normals.

The posteriori conditional probability distribution is given by

$$p(\boldsymbol{d}|\boldsymbol{y}) \propto \exp(-U_{\text{total}}/T), \tag{B.6}$$

where we use $U_{\text{total}} = (1-\alpha)U_{\text{norm}} + \alpha U_{\text{site}}$, in which $\alpha \in [0:1]$ weighs the influence of the model terms. In searching for the MAP estimate

$$\hat{\boldsymbol{d}} = \text{argmax}_{\boldsymbol{d}}\ p(\boldsymbol{d}|\boldsymbol{y}) \tag{B.7}$$

The Iterative Conditional Modes (ICM) method is a typical choice of optimization if the objective functional is convex. However, this is often only the case for simple MRFs and ML estimates are not always available. More advanced optimization can be done e.g. by simulated annealing using Gibbs sampling or the Metropolis-Hastings (MH) algorithm, followed by averaging or application of ICM in search of the most optimal state of the random field.

When applying simulated annealing the a-posteriori probability distribution is linked to the prior and the observation model by

$$p(\boldsymbol{d}|\boldsymbol{y}) \propto (p(\boldsymbol{y}|\boldsymbol{d})p(\boldsymbol{d}))^{1/T}, \tag{B.8}$$

where T is the temperature governing the process. At high temperatures all states are equally likely, however, decreasing the temperature increases the influence of the model terms. If the temperature is decreased slowly enough the algorithm will converge to the MAP estimate [107]. See [248, 57] for decreasing temperature schemes.

B.3 Results

Markov random field restoration using the Gaussian site-prior is applied to the training data after the TPS deformation of the model mesh using the PSP for initialization. In Fig. B.2c,d we show a correspondence field after the MRF relaxation and the resulting reconstruction of the target shape. The figure is to be compared to Fig. B.2a,b using the point to surface projection.

Problems in the registration field using PSP are removed by applying the MRF restoration. This is the case in respect to both the regularity of the polygonization, and the reconstruction error in representing the target shape by the deformed model surface. To obtain a measure of the uniformity of the polygonization of the target shape we examine the regularity of its triangular structure. By measuring the coefficient of variance of the edge lengths we obtain a standardized measure of the width of the underlying distribution. Results are shown in Fig. B.3 for all subjects. The left plot shows the coefficients before and after MRF restoration of the correspondence field, and the right figure shows a histogram of the reductions in the coefficients of variance. A rank test shows the significance of the MRF regularization since a reduction in the coefficient is obtained for all subjects. The improvement in shape reconstruction is show in Table B.1. Applying the observation model is performed with $\alpha = 0.5$. This parameter should be chosen using cross-validation in a more exhaustive search for an optimal deformation field. However, since the shapes are relatively smooth and regular the results shows no significant improvement in the reconstruction error by introducing the observational term. In Fig. B.4 the reconstruction error of the target shape of subject 1 is shown using PSP and MRF restoration based on the Gaussian site-prior. Notice the improved reconstruction using MRF.

When the model mesh is warped to another shape, it occurs that some correspondences are placed outside the region of interest on the target shape. Therefore, the model mesh is pruned to contain only the points that are warped to valid areas for all shapes in the training set. The model mesh contains approximately 3000 vertices after pruning. Having established a dense correspondence field it is now possible to dispose of the anatomical landmarks as well as the original meshes of the training set. The set of meshes with dense correspondence is applied in the following statistical shape analysis. The shapes are aligned by a generalized Procrustes analysis [125]. The pure shape model is built using a similarity transformation in the Procrustes alignment while a rigid-body transformation is used to build the size-and-shape model [83]. An Active Shape Model (ASM) [61] is constructed based on a Principal Component Analysis (PCA) of the Procrustes aligned shapes. Let each aligned shape be represented as a vector of concatenated x, y and z coordinates $\mathbf{x}_i = [x_{i1}, y_{i1}, z_{i1}, \ldots, x_{in}, y_{in}, z_{in}]^T$, $i = 1, \ldots, s$, where n is the number of vertices and s is the number of shapes.

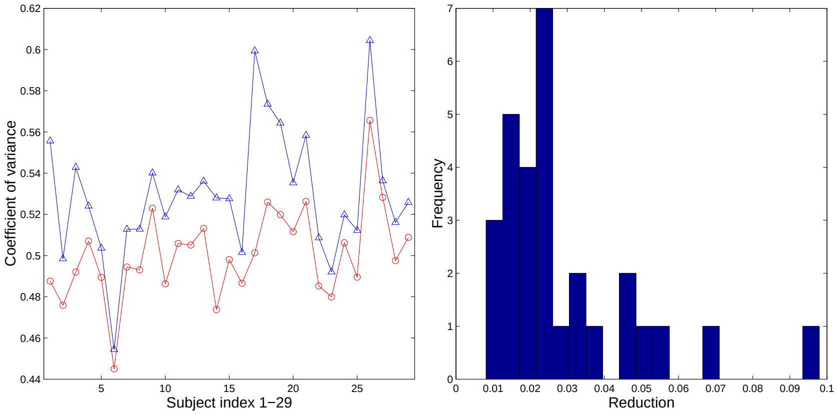

Figure B.3: Left: Comparison between the point to surface projection (upper curve) and the MRF regularization (lower curve) by evaluating the coefficient of variance of the edge lengths of the polygonization of the target surface. Right: A histogram of the reduction in coefficient of variance over the training data.

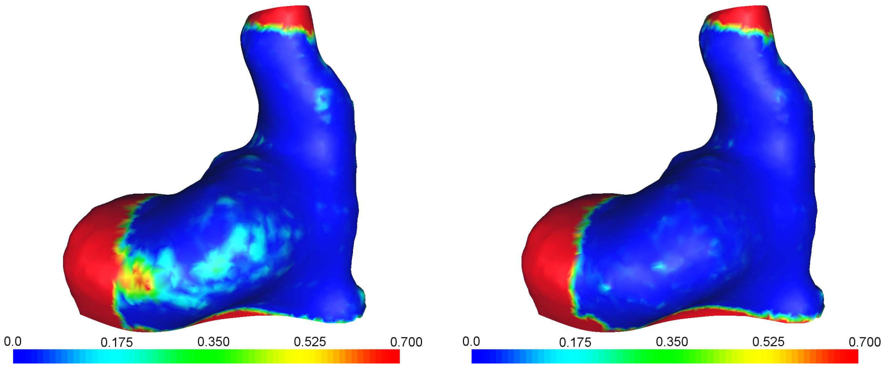

Figure B.4: The reconstruction error [mm] for subject one using the point to surface projection (left) and the MRF correspondence restoration (right).

	Registration Method			
Subject	PSP	MRF$_{p=2}$	MRF$_{p=1}$	MRF$_{p=2,q=1}$
1	0.048 ± 0.013	0.044 ± 0.013	0.049 ± 0.014	0.043 ± 0.013
2	0.046 ± 0.013	0.042 ± 0.013	0.043 ± 0.012	0.040 ± 0.012
3	0.048 ± 0.014	0.042 ± 0.013	0.043 ± 0.013	0.040 ± 0.012
4	0.044 ± 0.012	0.038 ± 0.011	0.040 ± 0.011	0.038 ± 0.012
5	0.045 ± 0.013	0.042 ± 0.012	0.043 ± 0.012	0.040 ± 0.012
6	0.045 ± 0.014	0.046 ± 0.015	0.045 ± 0.015	0.043 ± 0.014
7	0.047 ± 0.014	0.046 ± 0.014	0.046 ± 0.014	0.046 ± 0.015
8	0.040 ± 0.011	0.038 ± 0.011	0.039 ± 0.011	0.050 ± 0.013
9	0.041 ± 0.011	0.039 ± 0.011	0.039 ± 0.011	0.038 ± 0.011
10	0.049 ± 0.015	0.044 ± 0.013	0.045 ± 0.013	0.043 ± 0.013
11	0.046 ± 0.013	0.046 ± 0.014	0.045 ± 0.013	0.055 ± 0.014
12	0.050 ± 0.014	0.043 ± 0.013	0.044 ± 0.013	0.041 ± 0.012
13	0.042 ± 0.010	0.037 ± 0.009	0.039 ± 0.009	0.041 ± 0.009
14	0.048 ± 0.013	0.040 ± 0.011	0.042 ± 0.012	0.040 ± 0.011
15	0.043 ± 0.012	0.041 ± 0.012	0.040 ± 0.012	0.038 ± 0.011
16	0.049 ± 0.013	0.043 ± 0.012	0.044 ± 0.012	0.052 ± 0.013
17	0.064 ± 0.019	0.049 ± 0.014	0.059 ± 0.018	0.064 ± 0.016
18	0.051 ± 0.015	0.042 ± 0.012	0.048 ± 0.013	0.053 ± 0.013
19	0.064 ± 0.020	0.052 ± 0.015	0.058 ± 0.017	0.049 ± 0.015
20	0.053 ± 0.015	0.049 ± 0.015	0.050 ± 0.015	0.050 ± 0.013
21	0.049 ± 0.013	0.041 ± 0.011	0.045 ± 0.012	0.039 ± 0.010
22	0.048 ± 0.014	0.042 ± 0.012	0.044 ± 0.013	0.048 ± 0.014
23	0.040 ± 0.011	0.037 ± 0.011	0.038 ± 0.011	0.042 ± 0.011
24	0.043 ± 0.013	0.041 ± 0.013	0.042 ± 0.013	0.048 ± 0.014
25	0.044 ± 0.013	0.037 ± 0.011	0.039 ± 0.011	0.046 ± 0.012
26	0.056 ± 0.014	0.046 ± 0.011	0.052 ± 0.012	0.058 ± 0.013
27	0.042 ± 0.011	0.039 ± 0.011	0.040 ± 0.011	0.039 ± 0.012
28	0.049 ± 0.013	0.041 ± 0.011	0.045 ± 0.013	0.047 ± 0.013
29	0.048 ± 0.014	0.045 ± 0.014	0.045 ± 0.013	0.047 ± 0.013
Average	0.048 ± 0.013	0.042 ± 0.012	0.045 ± 0.013	0.045 ± 0.013

Table B.1: Reconstruction errors [mm] using PSP and MRF regularization. The mean ± one std. is shown for each method. The site-prior is governed by the p-norm and q controls the sensitivity of the observational energy term dependent on the surface normals.

The PCA is performed on the shape matrix $\mathbf{D} = [(\mathbf{x}_1 - \overline{\mathbf{x}})|\dots|(\mathbf{x}_s - \overline{\mathbf{x}})]$, where $\overline{\mathbf{x}}$ is the average shape. A new shape exhibiting the variance observed in the training set is constructed by adding a linear combination of eigenvectors to the average shape $\mathbf{x}_{\text{new}} = \overline{\mathbf{x}} + \Phi\mathbf{b}$, where $\mathbf{b}$ is a vector of weights controlling the modes of shape variation and $\Phi = [\phi_1|\phi_2|\dots|\phi_t]$ is the matrix of the first t eigenvectors of $\mathbf{D}\mathbf{D}^T$. The three first modes of variation of the size-and-shape shape model derived using Gaussian MRF regularization are shown in Fig. B.5. All the generated shapes look like natural ear canals with no deformations or folds in the mesh. Mode 1 consists of a bending of the canal and a flattening of the concha part. Mode 2 explains some of the shape variation observed in the inner part of the ear canal. Mode 3 is a combination of a flattening and twisting of the inner part of the ear canal and a general shape change of the concha. The distribution of the modes against each other is examined using pairwise plots and no obvious abnormalities were found (results not shown). In comparing the effect of the MRF regularization over the PSP method in the shape tangent space we find a reduction of more than 4% of the total variance of the resulting point distribution model. In Fig. B.6 the variance contained in each principal component is shown together with the pct. reduction of the variance in each subspace. The average reduction of variance in each subspace is approximately 8% and the pct. reduction generally increases for higher dimensions.

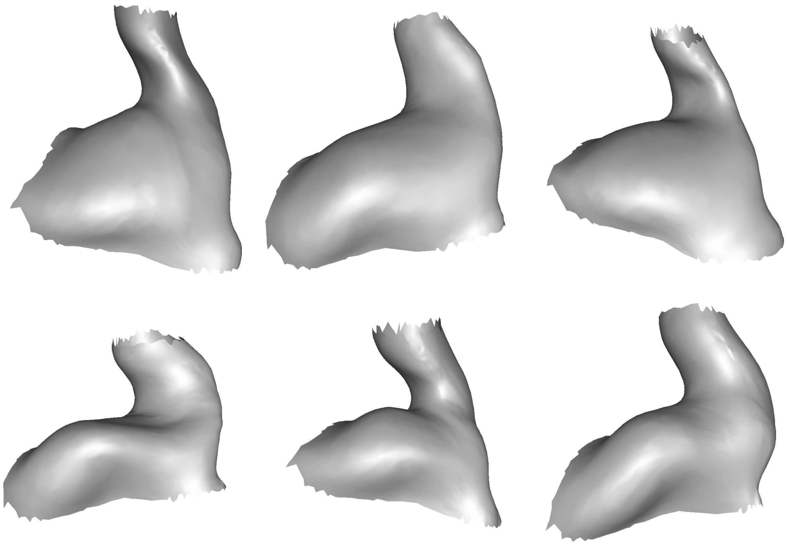

(a) Mode 1 (b) Mode 2 (c) Mode 3

Figure B.5: Size-and-shape shape model. The first three modes of variation shown at +3 (top) and −3 (bottom) standard deviations from the mean shape.

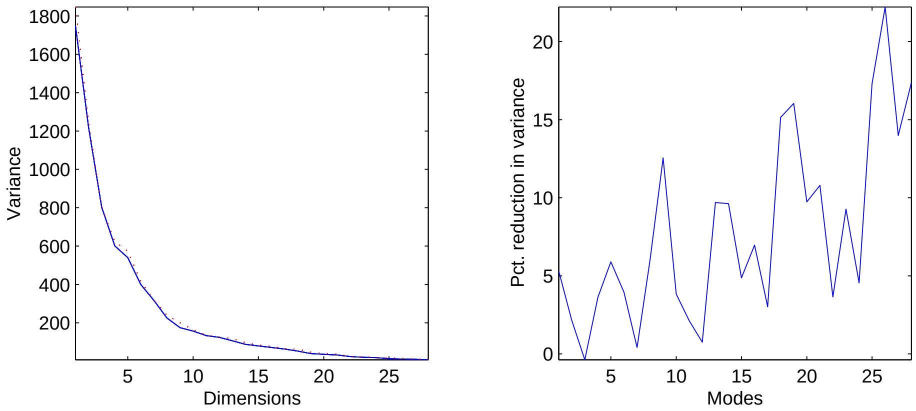

Figure B.6: Left: the variance contained in each principal component, the dotted line using point to surface projection and the solid line applying the MRF regularization step. Right: the reduction in the variance as a function of dimensionally of the model. The average reduction in each subspace is approximately 7% and the reduction of the total variance in the shape tangent space more than 4%.

B.4 Summary and Conclusions

A method is proposed for building statistical shape models based on a training set with an initial sparse annotation of corresponding landmarks of varying confidence. A model mesh is aligned to all shapes in the training data using the Thin Plate Spline transformation based on the anatomical landmarks. From the deformed model mesh and a target shape we derive a dense registration field of point correspondences. Applying the Markov Random Field restoration we obtain a dense, continuous, invertible registration field (i.e. a homeomorphism). The stochastic restoration acts as a relaxation on the TPS constrained model mesh with respect to the biological landmarks. The landmarks are identified with varying confidence and the MRF relaxation allows for a data driven enhancement of the object correspondences. Using the site-prior, the algorithm converges to the most simple deformation field which creates a tendency to match points of similar geometry since the field otherwise must be more complex. Moreover, inclusion of observational models could compensate further where the prior fails in more complex regions. In the present case study of smooth and regular shapes no significant benefit of applying more complex MRF were obtained. In comparison to applying point to surface projection the MRF regularization provides i) improved homogeneity of the target shape polygonization free of surface folds, ii) better reconstruction capabilities, and

iii) a more compact Active Shape Model description of all the training data. The point to surface projection performs reasonably well in representing the target shape over most regions of the ear canals. However, it fails in regions with strong surface dynamics and when the source and target surfaces are too far apart. The fact that the MRF regularization produces a reduction of more than 4% of the total variance contained in shape tangent space is noteworthy. The reduction is explained by increased collinearity between semi-landmarks distributed over the entire shape. It indicates an improvement in the shape representation in terms of homologous point correlation and thus constitutes a better basis for generative modeling.

Acknowledgments

The authors would like to thank Dr. Rasmus Larsen, IMM, DTU, for valuable discussions on MRFs, and Audiology Technician Claus Nielsen, Oticon Research Centre Eriksholm, for annotating the ear canals.

Appendix C

Non-Rigid Registration of 3D Surfaces using Markov Random Field Regularisation

Rasmus R. Paulsen, Klaus B. Hilger,

Rasmus Larsen, and Hervé Delingette

Abstract

A general framework for the registration of 3D surfaces using Markov Random Field Regularisation of the correspondence field is presented. An initial correspondence field is created by a simple projection technique. This correspondence field is regarded as a collection of random variables. Each site assigned an energy function that is based on a prior term and a model term, where the prior consists of scene specific knowledge and the model term is governed by more standard physical considerations concerned with the nature of the shapes. This means that there is a high degree of freedom in designing the local energy functions. Finally, the energy functions are shown to constitute a Markov Random Field using the Hammersley-Clifford theorem. This enables the use of a set of well-known stochastic optimisation techniques including Iterative Conditional Modes and Simulated Annealing.

The framework is used to align synthetic shapes in a way similar to a regularised iterative closest point algorithm. Furthermore, it is used to generate a dense correspondence over a set of laser-scanned ear canals. The set of dense correspondences are then used to build a statistical shape model of the ear canal. This approach leads to a more compact shape model and improves the mesh quality, when compared to a projection-based technique. It is also demonstrated how the parameters of the model can be chosen with regard to an objective function. An efficient method for calculating the mean curvature of triangulated surfaces is also presented.

C.1 Introduction

In a registration, the goal is to establish correspondence between homologous regions in images. In medical imaging, most registration algorithms deal with 3D voxel volumes, as surveyed by Maintz and Viergever [186]. Recently, other modalities such as laser scanners that produce 3D surface data are being used in medical imaging. Voxel based registration techniques are not suited for surfaces and therefore other types of registration algorithms are needed. An overview of surface registration algorithms can be found in [14].

When two or more surfaces come from the same class of objects, it is desirable to establish point-to-point correspondences, where the points correspond across all the surfaces in the data set. In shape-analysis [69, 61], finding a basis of homologous points is thus a fundamental issue that comes before Procrustes analysis [113] and shape space decomposition [178]. It can be desirable to match surface features such as curvature or surface texture, but since the amount of information available varies from data set and data type, it is not possible to find an algorithm that works with all data. It is better to specify a framework that can be adapted to the data and the application. Such a framework is proposed in this paper.

Placing manual landmarks in 3D is difficult and error-prone. Therefore, it is highly desirable to develop automated methods that can find the optimal dense correspondence between the objects. In this work, an initial correspondence vector field is regularised by casting the problem into the framework of Bayesian Markov Random Field (MRF) restoration. The Bayesian paradigm is a framework for incorporating stochastic models of visual phenomena into a very general set of tasks. In this adaptation of the framework, each vertex in the mesh is assigned an energy function that is based on a prior term and a model term. The prior consists of scene specific knowledge about the mesh. For example, some degree of spatial smoothness in the random field. The model term is governed by more standard physical considerations concerned with the nature of the shapes, such that homologous points are lying on surface patches with the same differential characteristics. This means that there is a high degree of freedom in designing the local energy functions. Finally, the energy functions are shown to constitute a Markov Random Field, which enables the use of a set of well-known stochastic optimisation techniques.

The framework presented in this work is thus general enough to allow the use of different surface features and may be adapted to different types of applications. The framework is used to align synthetic shapes in a way similar to a regularised iterative closest point algorithm. Furthermore, it is used to generate a dense correspondence over a set of laser-scanned ear canals. The set of dense correspondences are then used to build a statistical shape model of the ear canal. This approach leads to a more compact shape model and improves the mesh quality, when compared to a projection-based technique. It is also demonstrated how the parameters of the model can be chosen with regards to an objective function.

The remainder of this text is as follows. Section C.2 reviews related work. Section C.3 describes the theory of Markov Random Fields. In Section C.4, the implementation is described. Examples of the framework used on synthetic and real data can be found in Section C.5. In section C.6, we give some concluding remarks.

C.2 Related Work

One of the first general purpose surface alignment algorithms, the Iterative Closest Point (ICP) algorithm [25, 262], generates a point wise correspondence between shapes and can therefore be thought of as a registration algorithm. The ICP framework has later been extended to include surface characteristics, when searching for the optimal correspondence. Feldmar and Ayache [94] do not find the closest points, but searches for closest *feature vectors*, which contains both the coordinates of the point, but also the normal and the principal curvatures of the surface at that point. From the set of matches, a global affine transformation and a set of local affine transformations are calculated. The parameters of the local affine transformations are later spatially smoothed. This method is similar to the one proposed in this article but is difficult to adapt to data with other types of surface features.

Caunce and Taylor [52] also use a variant of the ICP algorithm to generate point correspondences over a set of shapes. In this work, the distance between a point on the source shape and the corresponding point on the target shape is weighted by a factor that depends on a set of properties of the surfaces in the neighbourhood of the points. The final correspondences are used to build a statistical shape model of the cortical sulcal.

Lorenz and Krahnstöver [184] find the correspondence between two shapes by an initial Thin Plate Spline based warp followed by a closest point projection. The correspondence are later regularised using a relaxation technique giving a more homogeneous representation of the target shapes. No structural or shape specific information is used in the regularisation step. A similar method is used by Hutton to generate dense shape models of the human face [143, 145]. In this method, ICP is used when the shape model is fitted to unseen faces. No regularisation of the correspondence field is performed. Another similar method used for atlas-based recognition of the hip prior to surgery is presented in [89].

In geometry constrained diffusion algorithm proposed by Andresen and Nielsen [8] the simplest correspondence field between two shapes is found by an iterative diffusion process where the vector field is projected back on the target surface between each iteration. The method is a simple smoothing of the correspondence field and holds no stochastic elements.

The modern mathematical analysis of shape changes has been influenced by the early work of Bookstein [31, 34] and Dryden and Mardia [83]. A popular method for building shape models is the Active Shape Model method by Cootes et al. [61]. Other methods includes the spherical harmonics approach by Gerig [108], the M-Rep approach by Pizer, Styner, and Gerig [207, 236], and the Fourier surfaces explored by Staib et al. [230].

Since the paper by Geman and Geman [107] on stochastic relaxation, Gibbs distributions, and Bayesian restoration, the literature has exploded with applications of the Bayesian paradigm in image analysis and image processing [173]. A thorough discussion of Markov Random Fields can be found in [106, 182, 253].

C.3 Markov Random Field Regularisation of Correspondences

It is assumed that an initial correspondence field $\boldsymbol{D}$, that matches the source shape $\boldsymbol{S}_s$ onto the target shape $\boldsymbol{S}_t$ exists, where $\boldsymbol{x}_i$ is a point on the source shape and therefore $\boldsymbol{x}_i + \boldsymbol{d}_i$ is the corresponding point on the target surface. This can be created for each vertex in the source mesh by finding the closest point on the target shape. In section C.4.1, it is explained in details how an initial correspondence field is found. The problem of finding the optimal correspondence vector field is then cast into a Bayesian framework of Markov Random Field restoration.

C.3.1 Bayesian Paradigm

The Bayesian paradigm proposed by Besag and others consists of four successive stages [24]. Adapted to the current application they become:

1: Construction of a prior probability distribution $p(\boldsymbol{d})$ for the correspondence field $\boldsymbol{D}$.

2: Formulation of an observation model $p(\boldsymbol{y}|\boldsymbol{d})$ that describes the distribution of the observed shapes $\boldsymbol{Y}$ given any particular realization of the prior distribution. $\boldsymbol{Y}$ is the combined source and target shape.

3: Combination of the prior and the observation model into the posterior distribution by Bayes theorem

$$p(\boldsymbol{d}|\boldsymbol{y}) = \frac{p(\boldsymbol{y}|\boldsymbol{d})p(\boldsymbol{d})}{p(\boldsymbol{y})}. \tag{C.1}$$

4: Drawing inference based on the posterior distribution.

The goal is to find the correspondence field that maximises the posterior probability

$$\hat{\boldsymbol{d}} = \arg\max_{\boldsymbol{d}} \; p(\boldsymbol{d}|\boldsymbol{y}). \tag{C.2}$$

In the following, it is explained how the above-mentioned probability distributions are defined using the theory of Markov Random Fields.

C.3.2 Graphs and Neighbourhoods

To describe a probability distribution on a spatial arrangement of points some useful definitions from graph theory are necessary.

Given a graph of n connected sites $S = \{s_i\}_{i=1}^{n}$. A neighbourhood system $\mathcal{N} = \{N_s, s \in S\}$ is any collection of subsets of S for which i) $s \notin N_s$, and ii) $r \in N_s \Leftrightarrow s \in N_r$, then N_s are the neighbours of s. A clique C is a subset of sites S for which every pair of sites are neighbours. The surface mesh is treated as an undirected graph and $i \sim j$ is used to denote that site i and site j are neighbours.

C.3.3 Gibbs Distributions and Markov Random Fields

Given a neighbourhood system $\mathcal{N}$ on the set of sites S, the probability distribution of any family of random variables indexed by S, i.e. $\boldsymbol{D} = \{D_s | s \in S\}$ can now be considered. In this paper $\boldsymbol{D}$ is the correspondence field and D_s is a 3D vector placed at the vertex with index s.

The Markov property of MRFs is expressed as [107]

$$p(d_s|d_r, r \neq s) = p(d_s|d_r, r \in N_s)\ \forall\ s \in S, \tag{C.3}$$

which means that the probability distribution of each site only depends on the state of neighbouring sites. This does not exclude long-range correlations in the probability distribution over the entire graph though. To be able to specify the conditional probabilities in practice the equivalence between the Gibbs distributions and Markov Random Fields is used.

Given a neighbourhood system $\mathcal{N} = \{N_s\}$ let all cliques be denoted by $\mathcal{C}$. For all $C \in \mathcal{C}$ it is assumed that a family of potential functions V_C exist. An energy function of any given configuration of $\boldsymbol{D}$ can now be defined

$$U(\boldsymbol{d}) = \sum_{C \in \mathcal{C}} V_c. \tag{C.4}$$

This leads to the definition of the Gibbs distribution induced by the energy function $U(\boldsymbol{d})$

$$p(\boldsymbol{d}) = \frac{1}{Z} \exp(-U(\boldsymbol{d})/T), \tag{C.5}$$

where Z is the partition function and T is a parameter referred to as temperature. The Gibbs distribution maximises entropy (uncertainty) among all distributions with the same expected energy. The temperature controls the "peaking" of the density function. The normalising constant, Z, may be impossible to obtain due to the curse of dimensionality but often only ratios of probabilities are needed and the constant cancels out. The relation between the Gibbs distribution and Markov Random Fields are specified in the following theorem

Theorem C.1 *(Hammersley-Clifford). Let $\mathcal{N}$ be a neighbourhood system. Then $\boldsymbol{D}$ is a Markov random field with respect to $\mathcal{N}$ if and only if $p(\boldsymbol{d})$ is a Gibbs distribution with respect to $\mathcal{N}$.*

A proof can be found in [106]. Thus the task is to specify potentials that induce the Gibbs distribution in order to encompass MRF properties of $\boldsymbol{D}$.

Since the goal is to model the correspondence between $\boldsymbol{S}_s$ and $\boldsymbol{S}_t$ the correspondence vectors are bound to the surfaces, in effect only posing constraints on the length of the vectors at the individual sites. In practice, the constraint may be enforced by projection of the end of the correspondence vectors onto the closest point of the target surface in every site update of the relaxation. This is explained in detail in section C.4.2.

C.3.4 Prior Distributions

Similar to pixel priors [24] energy functions based on differences between neighbouring sites are constructed. Extending to the multivariate case the general expression of the energy governing the site-priors becomes

$$U_{\text{site}}(\boldsymbol{d}) = \sum_{i \sim j} ||\boldsymbol{d}_i - \boldsymbol{d}_j||_p^p, \tag{C.6}$$

where $|| \cdot ||_p$ is the p-norm, $1 \leq p \leq 2$, and $\boldsymbol{d}_i$ represents the correspondence vector at the ith site.

With $p = 2$ the energy function induces a Gaussian prior on the correspondence field as used by for example Besag [24] in image restoration. Neglecting regions with strong surface dynamics the local optimisation becomes convex and the maximum likelihood (ML) estimate of the correspondence vector at the ith site is taken as the mean of the neighbouring correspondence vectors. Since the edges of the meshes have not unit lengths, it is necessary to use a weighted average

$$\hat{\boldsymbol{d}}_i = \sum_{j \in N_i} w_{ij} \boldsymbol{d}_j / \sum_{j \in N_i} w_{ij}. \tag{C.7}$$

Here w_{ij} are Gaussian weights derived from a fixed kernel size and calculated on the basis of the Euclidean distance between vertex i and j in the source mesh. A pure prior MRF restoration of correspondences hence solves the aperture problem and the three-dimensional interpolation problem simultaneously by finding the simplest correspondence field.

Using this prior the maximum a posteriori (MAP) estimate of the MRF optimised purely by Iterative Conditional Modes is similar to the steady state of the algorithm for geometry constrained diffusion (GCD) proposed by Andresen and Nielsen [8]. GCD is a numerical scheme for solving a space and time discretised version of the heat equation on the correspondence field with certain boundary conditions. The GCD implementation works on volume-voxel diffusion, while the MRF method described in this paper works with 2D surfaces embedded in a 3D space. Moreover, the GCD approach in essence applies gradient descend optimisation and is directly dependable on a good initialisation of the correspondence field. The MRF formulation provides a natural framework allowing for more advanced optimisation.

Abandoning homogeneity and isotropy of the MRF non-global kernels may be introduced. Thus, adaptive Gaussian smoothing may be applied, e.g. by setting the standard deviation of the kernel to the square-root of the edge length of the closest neighbour of site i on the graph. Moreover, using the $p = 1$ norm induces a median prior, with the ML estimate being the median of the correspondence vectors at the weighted neighbouring sites. This property makes the MRF attractive for correspondence fields with discontinuities, thus avoiding the smearing of edges attained by the Gaussian prior.

C.3.5 Observation Models

The observation model $p(\boldsymbol{y}|\boldsymbol{d})$ describes the conditional distribution of the observed shapes $\boldsymbol{Y}$. A mapping that makes correspondences between regions of similar surface properties may be favoured by specifying an observation model. The similarity measures may include derived features of the observed surfaces such as the curvature, orientation of the surface normals, or even surface texture.

The energy function U_{model} must be specified and depends on the application but typically involves a linear combination of multiple derived measures. In the following a selection of surface features is proposed.

C.3.5.1 Local Surface Orientation

The simple dot product between the surface normals may form the basis in specifying a governing energy function that favours correspondence between regions of similar orientation by

$$U_{\text{norm}}(\boldsymbol{y}|\boldsymbol{d}) = \sum_i ||\boldsymbol{n}_{s,i}^T \boldsymbol{n}_{t,i} - 1||^q, \tag{C.8}$$

where $\boldsymbol{n}_{s,i}$ is the surface normal at vertex i with position $\boldsymbol{x}_i$ on the source surface $\boldsymbol{S_s}$, and $\boldsymbol{n}_{t,i}$ the normal of the target surface $\boldsymbol{S_t}$ at the coordinate $\boldsymbol{x}_i + \boldsymbol{d}_i$. The parameter $q > 0$ controls the sensitivity of the energy function. The normal at $\boldsymbol{x}_i + \boldsymbol{d}_i$ is found by weighting the normals from the triangle in which $\boldsymbol{x}_i + \boldsymbol{d}_i$ is located. This is done by using the points barycentric coordinates as done in for example Phong shading [258, 99]. This energy function is expected to be useful when the source and target shape are roughly pre-aligned since it is not rotation invariant. Results for this energy function can be found in [199].

C.3.5.2 Surface Curvature

The use of second order geometric invariants such as curvature allows matching of homologous surface points despite a slight rotation of the surface. There are at least three types of surface curvatures that can be computed at each vertex: mean, Gaussian and total curvatures [82]. A general setting for the curvature energy is :

$$U_{\text{curv}}(\boldsymbol{y}|\boldsymbol{d}) = \sum_i ||\boldsymbol{c}_{s,i} - \boldsymbol{c}_{t,i}||_p^p, \tag{C.9}$$

where $\boldsymbol{c}_{s,i}$ is a vector containing the differential properties of the source surface at location $\boldsymbol{x}_i$ and $\boldsymbol{c}_{t,i}$ contains the differential properties of the target surface at the coordinate $\boldsymbol{x}_i + \boldsymbol{d}_i$. The differential properties at $\boldsymbol{x}_i + \boldsymbol{d}_i$ is found by interpolating as in section C.3.5.1.

C.3.5.3 Surface Texture

When surface texture is available multivariate locally derived features on the source and target shapes, $\boldsymbol{t}_s$ and $\boldsymbol{t}_t$, may be applied in an energy function operating in the p-norm

$$U_{\text{text}}(\boldsymbol{y}|\boldsymbol{d}) = \sum_i ||\boldsymbol{t}_{s,i} - \boldsymbol{t}_{t,i}||_p^p, \tag{C.10}$$

where $\boldsymbol{t}_{s,i}$ is a vector containing the texture of the source surface at location $\boldsymbol{x}_i$ and $\boldsymbol{t}_{t,i}$ contains the texture of the target surface at the coordinate $\boldsymbol{x}_i + \boldsymbol{d}_i$.

C.3.6 Posterior Probability Distribution

Normalisation of the energy terms from the different prior and observation models is typically chosen such that they operate on the same domain. However, the data analyst may choose to favour some terms over others, e.g. by relaxing the smoothness conditions in favour of correspondences between regions with similar surface characteristics. The total energy is:

$$U_{\text{total}} = (1-\alpha)U_{\text{model}} + \alpha U_{\text{site}}, \tag{C.11}$$

in which $\alpha \in [0:1]$ weights the influence of the model terms and U_{model} is a linear combination of measures as explained in section C.3.5. By combining equation (C.1), (C.5) and (C.11) the posteriori conditional probability distribution is given by

$$p(\boldsymbol{d}|\boldsymbol{y}) \propto \exp(-U_{\text{total}}/T). \tag{C.12}$$

The method used to find the MAP estimate

$$\hat{\boldsymbol{d}} = \arg\max_{\boldsymbol{d}} \; p(\boldsymbol{d}|\boldsymbol{y}), \tag{C.13}$$

is dependent on the complexity of the energy function. In section C.4.2 it is explained how The MAP estimate of the correspondence field can be found using stochastic optimisation.

C.4 Implementation

The implementation of the regularisation algorithm resembles the Iterative Closest Point (ICP) algorithm for rigid registrations [25, 262]. The algorithm thus calculates both a global transformation and a local correspondence. The algorithm is

1. *Initial Alignment:* The source and the target surface are roughly prealigned, using for example a set of sparse landmarks or multiple ICPs.
2. *Initial Correspondence:* Construct an initial correspondence field, $\boldsymbol{D}$.
3. *Optimisation:* Approximation of the MAP estimate of $\boldsymbol{D}$ using stochastic optimisation.
4. *Global Transformation:* Computation and application of the global rigid transformation
5. *Convergence:* Is the change in global transformation sufficiently small? If not go to 2.

Steps 2 to 5 are explained in detail in the following.

C.4.1 Initial Correspondence

The initial correspondence field is made by a closest point projection of the vertices from the source shape to the target shape. The closest point on the target surface is found by the *vtkCellLocator* class found in the Visualization Toolkit [219]. It uses a uniform-level octree subdivision [188], where each octant carries an indication of whether it is empty or not, and each leaf octant carries a list of the polygons inside of it. Therefore, the closest point is found as a point lying on a triangle and not just as a vertex. The barycentric coordinates of the points are also computed and used in the interpolation of surface features.

C.4.2 Optimisation

The maximum a posteriori estimates can be found using e.g. the Iterative Conditional Modes (ICM) [24] method, in which the random variables at each site are set to the value that maximises the conditional probability given the observations, and the current reconstruction elsewhere. The sites are typically visited in random order to avoid propagation of trends. Each correspondence vector is set to the ML estimate based on the prior and the model and then extended to the target surface to complete the surface correspondence. For the pure prior model, experiments have shown that ICM can be used successfully and it is a typical choice of optimisation if the objective functional is convex and a good initialisation is obtained. However, this is often only the case for simple MRFs and ML estimates are not always available.

More advanced optimisation can be done e.g. by simulated annealing [164, 248] using Gibbs sampling or the Metropolis-Hastings algorithm, followed by averaging or application of ICM in search of the most optimal state of the random field. This is needed when the energy term includes curvature or other derived surface characteristics.

When applying simulated annealing the a posteriori probability distribution is linked to the prior and the observation model by

$$p(\boldsymbol{d}|\boldsymbol{y}) \propto (p(\boldsymbol{y}|\boldsymbol{d})p(\boldsymbol{d}))^{1/T} = \exp(-U_{\text{total}}/T), \tag{C.14}$$

where T is a parameter referred to as the temperature. The temperature governs the probability of accepting configurations of higher energy. The temperature starts out high and decreases with time following a cooling schedule [57]. At high temperatures, all states are equally likely. If the temperature is decreased slowly enough the algorithm will converge to the MAP estimate [107]. See [172, 57] for temperature schemes. When a site is visited a new random vector is generated and the change in local energy, ΔU, is calculated based on this vector using equation (C.11). The new vector is then accepted with the probability

$$P_{\text{accept}} = \min(1, e^{\frac{-\Delta U}{T}}). \tag{C.15}$$

In the start where the temperature is high, nearly all configurations are accepted. This allows the algorithm to explore the state space before converging on a minimum.

The optimisation continues until the RMS criterion:

$$\sqrt{\frac{1}{N}\sum_{i}^{N} ||\boldsymbol{d}_{i,n} - \boldsymbol{d}_{i,n-1}||^2} < \varepsilon_1, \tag{C.16}$$

is satisfied. Here $\boldsymbol{d}_{i,n}$ is the correspondence vector at site i in the nth iteration and ε_1 is a user-chosen parameter. A fixed number of iterations can also be chosen or the criterion can be dependent on the temperature.

For each vertex in the mesh, a lookup table with IDs of the neighbouring vertices is computed prior to the optimisation. This is done to speed up the evaluation of the states of the neighbour sites. This is especially useful when more advanced neighbourhood criterions are used. A neighbourhood can for example be defined with respect to the geodesic distance from the vertex. In that case, the fast marching method can be used to calculate the involved distances [222, 163, 223].

C.4.3 Global Transformation

Since the shapes are only roughly pre-aligned prior to the regularisation the correspondence vector field may consists of a translation and a rotation component that can be removed.

When the optimal correspondence field is found each point, $\boldsymbol{x}_i$, on the source shape matches a point , $\boldsymbol{x}_i + \boldsymbol{d}_i$, on the target shape.

A rigid body transformation (rotation and translation), $\boldsymbol{T}$, that in a least-squares sense matches the source shape to the target shape can now be computed using this set of corresponding points. Several methods to calculate this transformation exist, including singular value decomposition [13], orthonormal matrices [134], a unit quaternion method [133], and a dual quaternion method [250]. For real world data, the methods have been shown to perform equally [87]. In this work, the unit quaternion method is used [133]. When the transformation is found, it is applied to the source shape.

C.4.4 Convergence

The algorithm is stopped when the root-mean-square (RMS) of the changes in the positions of the vertices in the source shape is less than a user-chosen parameter:

$$\sqrt{\frac{1}{N}\sum_{i}^{N}||\boldsymbol{x}_{i,n} - \boldsymbol{x}_{i,n-1}||^2} < \varepsilon_2, \tag{C.17}$$

where $\boldsymbol{x}_{i,n}$ are the points on the source surface in the nth iteration. Experiments show that 5-10 iterations are normally sufficient.

C.5 Results

The algorithm has been tried on both real and synthetic data.

C.5.1 Cube Registration

To test the robustness with regard to global alignment and random initialisation a synthetic data set consisting of two cubes has been constructed. The cubes are made by extracting two iso-surfaces from a voxel volume containing a Gaussian smoothed cube, using the marching cubes algorithm [183]. The biggest of the cubes is selected as being the source shape and the smallest as being the target shape. The initial correspondence field is created by for each point in the source shape finding the closest point on the target shape. The energy function consists of the pure prior model with the $p = 2$. Therefore, the local a posteriori conditional probability distribution is given by

$$p(\boldsymbol{d}|\boldsymbol{y}) \propto \exp(-\sum_{i \sim j} ||\boldsymbol{d}_i - \boldsymbol{d}_j||_2^2/T). \tag{C.18}$$

The maximum a posteriori estimate of the correspondence field is found by ICM as described in section C.4.2. Each vector is set to its ML estimate, which is the average of the neighbouring vectors weighted with their Euclidean distance equation (C.7).

After convergence of the ICM algorithm, the global transformation is calculated and applied to the source shape as described in section C.4.3. This is repeated until convergence as explained in section C.4.4. The polygonal structure of the source shape is then applied to the target shape via the correspondence field.

A number of experiments have been performed.

1. *Recovering rotation.* The source shape is rotated around the centre of mass to test the algorithms capabilities to remove global transformations. After convergence the rotational part of the global transformation, $\boldsymbol{T}$ is calculated and compared to the pre-rotating. A series of 216 tests where the x,y,z angle has varied from 0 to 25 degrees in step of 5 degrees has been run. The error is calculated as $|\theta_{x,p} - \theta_{x,f}| + |\theta_{y,p} - \theta_{y,f}| + |\theta_{z,p} - \theta_{z,f}|$, where the θ's are the rotations around the x,y and z axes. Index p is the pre-rotation and f the found rotation. The average error of 2.2° is probably caused by the round corners of the cubes that introduces an ambiguity in the registration. A result can be seen in figure C.1.

2. *Random Initialisation.* All the endpoints of the correspondence vector field is placed randomly on the surface of the target shape. This is done by calculating random positions in the space around the target cube and the projecting the point to the nearest point on the target surface. The correspondence field and the resulting dense mesh approximation of the target shape before and after optimisation can be seen in figure C.2. It is seen that the field converges on a good solution.

No experiments regarding translation have been performed since the shapes can be pre-aligned using the center of mass.

The large cube contains 3300 vertices, which is also the number of vectors in the vector field. The running time for the optimisation of the correspondence field is approximately 1 minute on a 2 GHz Intel Pentium 4 processor.

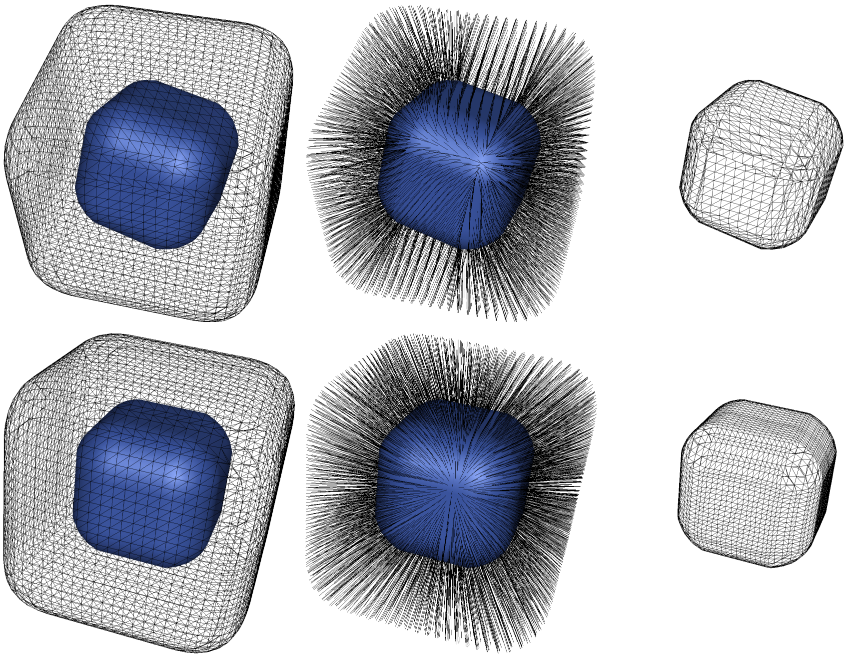

Figure C.1: Recovering rotation. **Top row:** Large source cube and small target cube, initial correspondence vector field and the initial dense mesh approximation of the target cube. **Bottom row:** Cubes after MRF alignment, optimised correspondence vector field and the optimised dense mesh approximation of the target cube.

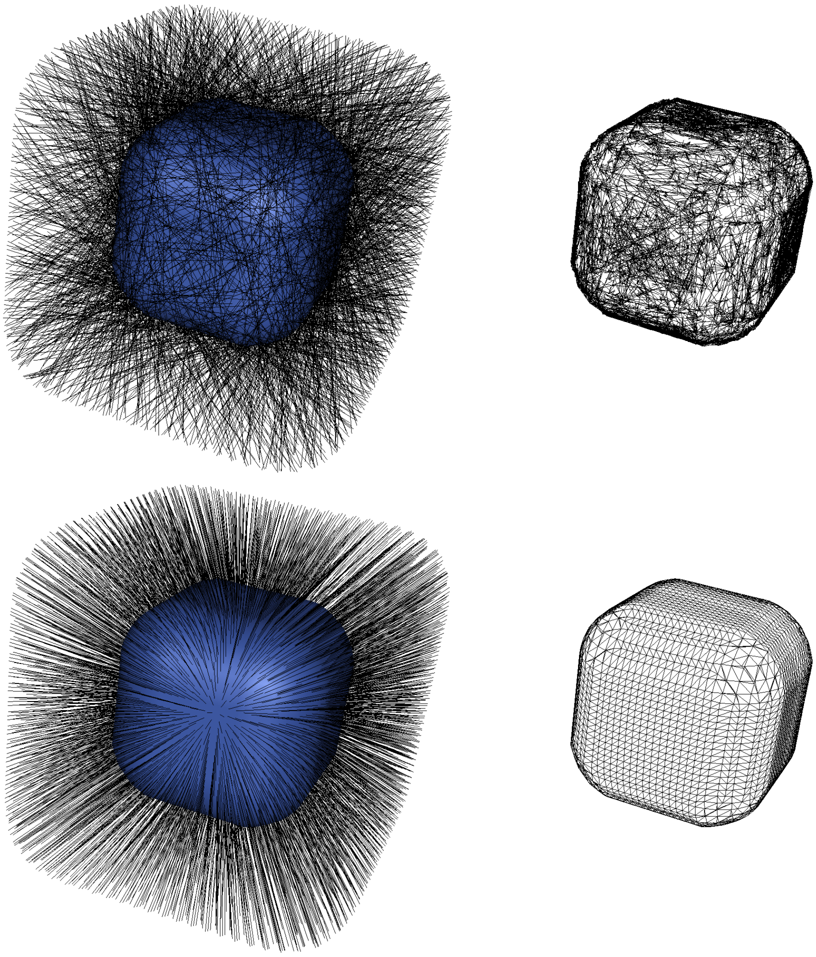

Figure C.2: Vector field unwinding. **Top row:** Initial random correspondence vector field and the resulting dense mesh approximation of the target cube. **Bottom row:** Correspondence vector field and dense mesh approximation after MRF optimisation.

C.5.2 Ear Canal Registration

A method for building a statistical shape model of the human ear canal is presented in [201]. The data consists of 29 3D ear canal surfaces extracted from laser scans of ear impressions. The local surface geometry of the ear canals varies much from one individual to another. Therefore, only very few ridges and extremal points are stable when comparing groups of ear canals. A set of 18 anatomical landmarks of varying confidence are placed on each ear canal, and constitute a sparse correspondence between the surfaces of the ear canals in the training set. The surfaces of the ear canals are not closed due to the opening of the ear canal and because the ear impressions are terminated in front of the ear drum. It is therefore necessary to identify the region of interest of each ear canal. Hence, planes are defined, which separate the valid parts of the surface from the invalid parts. In Fig. C.3, left, an ear canal with the anatomical landmarks and separating planes is shown.

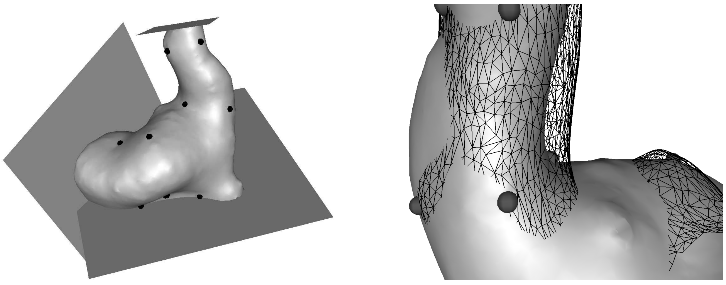

Figure C.3: Left: An example of a surface representation of an ear canal with the anatomical landmarks and the separating planes that defines the region of interest. The thin tubular structure in the top is the actual canal. The larger lower section is the concha, of which only the upper part is of interest. A cutoff plane through the concha is therefore defined. Right: The model mesh, shown by a wireframe, fitted to a target shape using Thin Plate Spline warping.

The anatomical landmarks do not constitute an exhaustive description of the surface of the ear canal. It is therefore necessary to generate a more dense set of landmarks describing the shape. For that purpose, a model mesh is constructed and fitted to all shapes in the training set. The model mesh is chosen as a decimated version of a natural well-formed ear canal labelled with the anatomical landmarks. The model mesh is fitted to each of the shapes in the training set using a Thin Plate Spline (TPS) warp based on the corresponding anatomical landmarks. TPS is a warp function that minimises the bending energy [34]. Since the TPS transform is exact only for the anatomical landmark locations, the vertices of the model mesh will not lie on the surface of the target shape, see Fig. C.3, right. Projecting each vertex in the warped model mesh to the closest point on the target surface produces a non-rigid correspondence field. However, using the Point to Surface Projection (PSP) introduces a critical risk of inversions, where the vertices of the model mesh shift place and cause folds in the mesh. Another secondary artifact is the non-uniformity of the correspondence vector field shown in Fig. C.4 giving rise to poor approximation of the target shape. In order to improve the correspondence vector field and avoid the problems inherent in applying point to surface projection a regularisation must be included. In the following, it is explained how the MRF method is applied to this problem. The aim is to generate a dense correspondence over a set of shapes and use this correspondence in the following shape modelling. It is therefore meaningful to include surface characteristics in the search for an optimal correspondence field. Since the shapes are pre-aligned, using the TPS warping it is assumed that there is no underlying rigid transformation, so the regularisation step only consists of the optimisation of the correspondence vector field. The energy function is therefore composed of a prior model with $p = 2$ and a model term with surface curvature. Combining equation (C.11), (C.12), (C.6) and (C.9) gives the local posteriori conditional probability distribution

$$p(\boldsymbol{d}|\boldsymbol{y}) \propto \exp(-((1-\alpha)\sum_{i} ||c_{s,i} - c_{t,i}||_2^2 + \alpha \sum_{i\sim j} w_{ij}||\boldsymbol{d}_i - \boldsymbol{d}_j||_2^2)/T), \quad \text{(C.19)}$$

where $c_{s,i}$ is the mean curvature of the source surface at location $\boldsymbol{x}_i$ and $c_{t,i}$ is the mean curvature at the coordinate $\boldsymbol{x}_i + \boldsymbol{d}_i$ and w_{ij} is a Gaussian weight. The kernel size of the Gaussian is determined by the distance to the closest neighbour.

C.5.2.1 Surface Curvature

In this application, we chose to base our curvature energy U_{curv} on mean curvature since it is of extrinsic nature (its value depends on the nature of the embedding space) unlike the Gaussian curvature which solely depends on the first order invariants [82].

There exist several methods to compute the mean curvature at a vertex of a triangulated mesh. One way consists in fitting a quadric patch to the neighbouring points, and computing the differential properties directly from this quadric [218]. A recent similar method using polynomial fitting of osculating jets can be found in [53]. Other methods include tensor voting [241, 240].

We propose an alternative approach, which is both efficient and robust. The principle on which is based the algorithm is the following : among all spheres

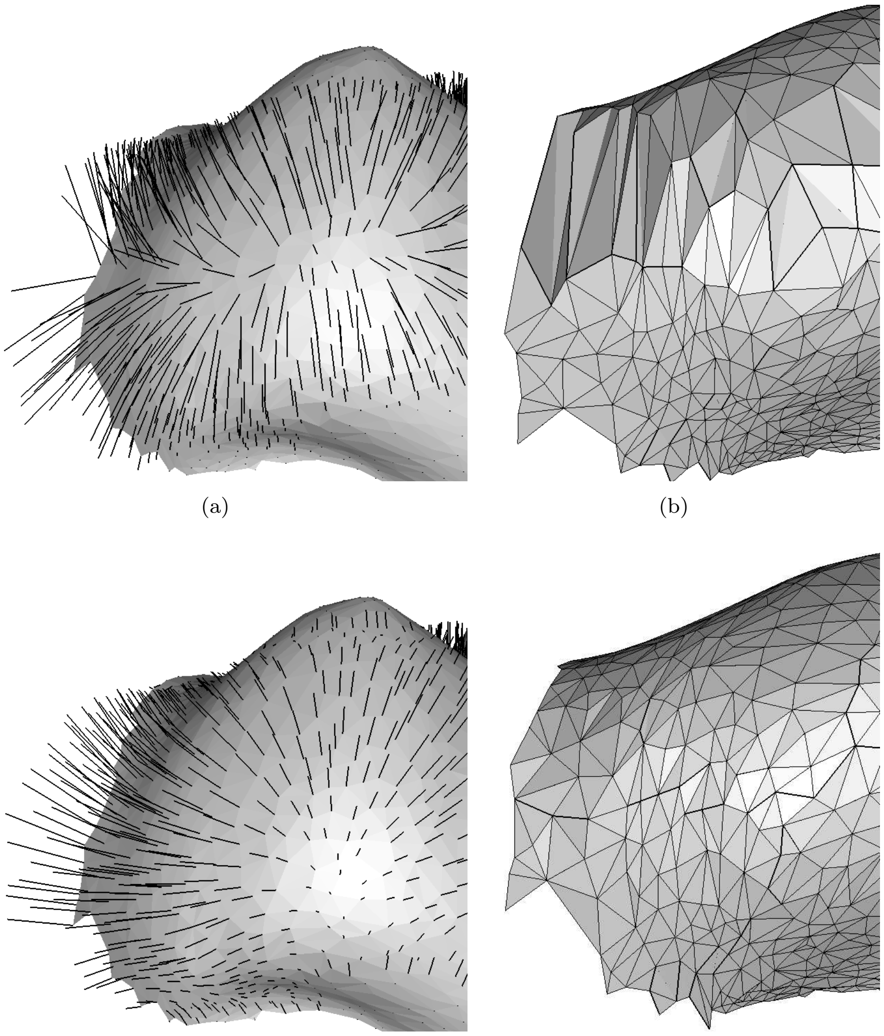

(a) (b)

(c) (d)

Figure C.4: **a**) The correspondence vector field derived using point to surface projection for moving the vertices of the source to the target shape. **b**) The resulting dense mesh approximation of the target shape. **c**) The optimised correspondence vector field ($\alpha = 0.2$) **d**) The improved dense mesh approximation of the target shape.

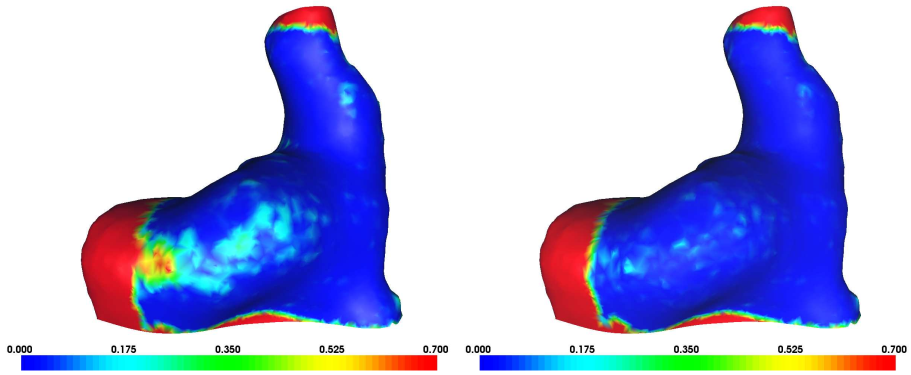

Figure C.5: Approximation errors for the point to surface projection method are seen to the left. To the right the errors after MRF regularisation ($\alpha = 0.2$). The approximation error is calculated by for each vertex in the target mesh finding the distance to the closest point on the approximation surface. The approximation error is only calculated for the part of the target surface approximated by the model mesh.

passing through a point P lying on a smooth surface, the one that minimises its distance to the surface has curvature C_P, the mean curvature at P [79].

For each vertex P, our algorithm consists in finding the curvature of the sphere that passes through P and that best approximates the set of neighbours P_N of P. The neighbour points are found by a region-growing algorithm that stops when the Euclidean distance to the seed point is too high. Alternatively, the geodesic distance could be used as instead of Euclidean distance.

Thanks to an inversion of centre P, we transform the estimation of the closest sphere into the least-square estimation of a plane. Indeed, inversion transforms any sphere passing through P into a plane whose distance from P is easily related to its curvature. More precisely, inversion with respect to the point P associates a neighbour point P_N to its inverse $\mathrm{Inv}(P_N)$

$$(P_N - P) \cdot (\mathrm{Inv}(P_N) - P) = 1. \tag{C.20}$$

The inverse point can be found as

$$\mathrm{Inv}(P_N) = \frac{P_N - P}{||P_N - P||^2} + P. \tag{C.21}$$

The estimation of the plane approximating $\{\mathrm{Inv}(P_N)\}$ is based on the eigenvector analysis of the inertia matrix. The mean curvature C_P at P is then given by $2D$ where D is the distance of P to the estimated plane. Further details and proofs can be found in [79]. The colour coded mean curvature of two ear canals can be seen in figure C.6.

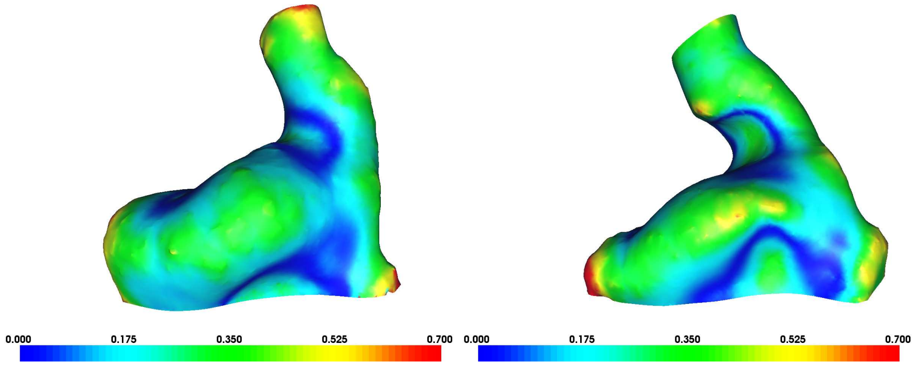

Figure C.6: Mean curvature of two different ear canal surfaces. It is seen that corresponding anatomical regions have mostly the same mean curvature.

C.5.2.2 Optimisation of the Correspondence Field

The MAP estimate of the correspondence vector field is found by the Metropolis-Hastings algorithm. See section C.4.2 for details.

The correspondence vector field consists of 3001 vectors. The running time for the optimisation of the correspondence field is approximately 2 minutes on a 2 GHz Intel Pentium 4 processor.

After the optimisation has converged, the polygonal structure of the model shape is applied to the target shape via the correspondence field.

C.5.2.3 Mesh Quality

Problems found in the initial correspondence field found by closest point projection are removed by applying the MRF relaxation. This is the case in both the regularity of the polygonisation, and in the approximation error in representing the target shape by the deformed model surface. To obtain a measure of the uniformity of the polygonisation of the target shape the regularity of its triangular structure is examined. An optimal mesh should consist of equilateral triangles. The quality of a triangle can therefore be measured by its minimum angle. As a measure of mesh quality the average of the minimum angle of all triangles in the mesh is used $\mathcal{F}_{\text{tri}} = \frac{1}{n}\sum_i \theta_{\text{min}}$, where θ_{min} is the minimum angle in triangle i. An optimal mesh will have a quality measure of $\mathcal{F}_{\text{tri}} = 60^\circ$. The quality of the mesh cannot be better than the quality of the model mesh, but it is still useful to compare the quality of the resulting approximating meshes. A rank test shows the significance of the MRF regularisation since an improvement of $\mathcal{F}_{\text{tri}}$ is obtained for all subjects. The improvement in mesh quality of the approximating mesh and the regularity of the correspondence field can be seen in Fig. C.4. The improvement in shape approximation is shown in Fig. C.5. The approximation error $\mathcal{F}_{\text{app}}$ is the average distance from the vertices in the target to the closest points on the approximation surface. The approximation error is only calculated for the part of the target surface approximated by the model mesh.

C.5.2.4 Shape Modelling

The set of meshes with dense MRF correspondences is used in a statistical shape analysis as explained in detail in [199, 201]. The model mesh is pruned to contain only vertices that are mapped to the legal region on all shapes in the training set. Details can be found in [201]. After the pruning, the model mesh contains 3001 vertices. The shapes are first aligned by a generalised Procrustes analysis [113]. The rigid-body transformation is used to build a size-and-shape model [83]. An Active Shape Model (ASM) [61] is constructed based on a Principal Component Analysis (PCA) of the Procrustes aligned shapes. Let each aligned shape be represented as a vector of concatenated x, y and z coordinates $\mathbf{x}_i = [x_{i1}, y_{i1}, z_{i1}, \ldots, x_{in}, y_{in}, z_{in}]^T$, $i = 1, \ldots, s$, where n is the number of vertices and s is the number of shapes. The PCA is performed on the shape matrix $\mathbf{D} = [(\mathbf{x}_1 - \overline{\mathbf{x}})|\ldots|(\mathbf{x}_s - \overline{\mathbf{x}})]$, where $\overline{\mathbf{x}}$ is the average shape. A new shape exhibiting the variance observed in the training set is constructed by adding a linear combination of eigenvectors to the average shape $\mathbf{x}_{\text{new}} = \overline{\mathbf{x}} + \Phi\mathbf{b}$, where $\mathbf{b}$ is a vector of weights controlling the modes of shape variation and $\Phi = [\phi_1|\phi_2|\ldots|\phi_t]$ is the matrix of the first t eigenvectors of $\mathbf{D}\mathbf{D}^T$.

There exist several methods to estimate the optimality of a shape model including the minimum description length approach discussed in [73, 76, 75]. In the work of Davies et al. a simple objective function is used in the initial optimisation steps [73]. This objective function, also used by Kotcheff and Taylor [169] is the determinant of the covariance matrix, which is equal to $\mathcal{F}_{\text{shape}} = \sum \log(\lambda_i + \epsilon)$, where λ_i are the eigenvalues of $\mathbf{D}\mathbf{D}^T$. $\mathcal{F}_{\text{shape}}$ measures the *volume* that the training set occupies in shape space [73]. The log is taken to avoid dominating roundoff errors and a small value $\epsilon = 10^{-8}$ is added to avoid degenerate minima with small eigenvalues. In an earlier study it was found that 7 modes of variation, is sufficient to describe the training data [201] and therefore $\mathcal{F}_{\text{shape}}$ is calculated based on the first 7 eigenvalues.

C.5.2.5 Parameter Estimation

Finding the optimal relation between the prior and the observation model depends on the data and the application. A sort of objective function is needed to determine the parameters of the model. In this application,x the data is used to build a shape model and therefore an obvious choice of objective function is linked to the optimality of the shape model. In figure C.7 it is seen that the shape model is optimal with respect to $\mathcal{F}_{\text{shape}}$ at $\alpha = 0.2$.

The parameters could also be chosen with respect to the mesh quality measure or the approximation error defined in section C.5.2.3. In figure C.7 box plots of the mesh quality and approximation error as function of α are shown. It is seen that $\alpha = 1.0$ would be optimal with respect to the mesh quality, thus reducing the Markov model to a pure prior model. On the other hand the improvement in mesh quality from $\alpha = 0.2$ to $\alpha = 1.0$ is so small that choosing $\alpha = 0.2$ could be argued to optimise both the shape model and the mesh properties.

C.6 Conclusion

A general framework for non-rigid registration of 3D surfaces is proposed. The method uses the framework of Bayesian Markov Random Field restoration to regularise the correspondence vector field between two shapes of the same class. The method can be adapted to specific data by including appropriate surface features in the model.

Using only the site-prior, the algorithm converges to the simplest correspondence field, which creates a tendency to match points of similar geometry since the field otherwise must be more complex. Moreover, inclusion of observational models compensates further, where the prior fails in regions that are more complex.

The framework is demonstrated on synthetic data, where the algorithm demonstrates the same abilities as a regularised iterative closest point algorithm. The algorithm is also used on real data to create correspondences over a set of shapes. These correspondences are then used to build a statistical shape model. The parameters of the regularisation are chosen so the shape model maximises a defined optimality criterion. This criterion could possible be included directly in the model term of the Markov model, but that is outside the scope of this ar-

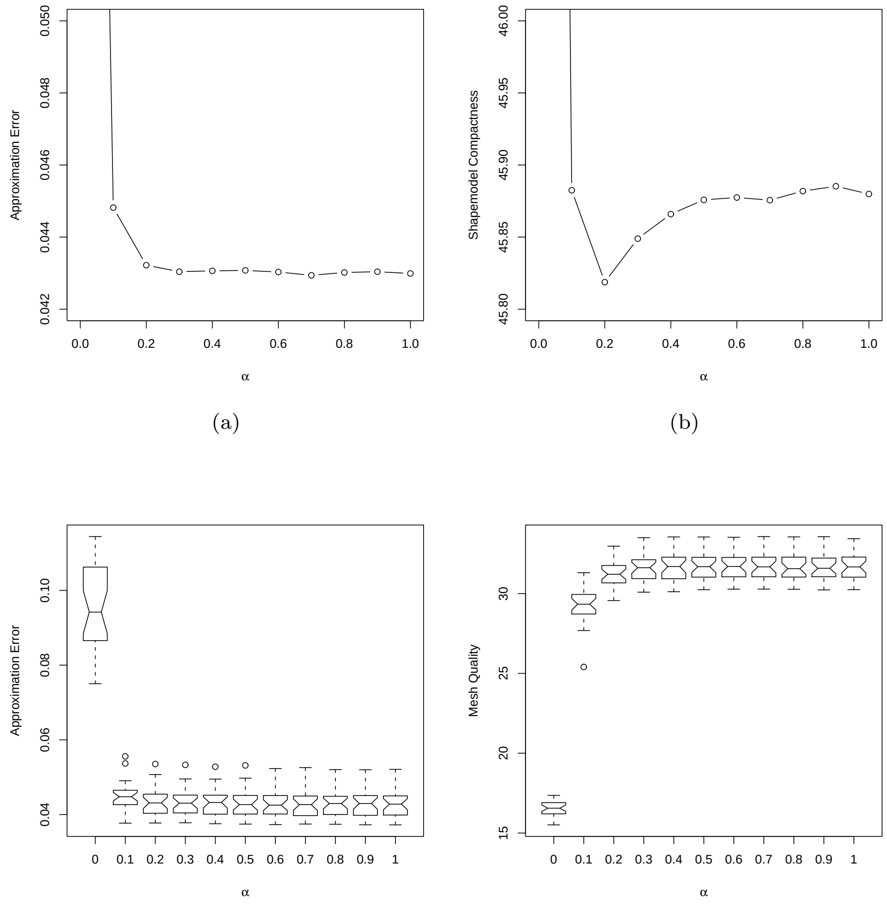

(a) (b)

(c) (d)

Figure C.7: **a**) The average surface approximation error $\mathcal{F}_{\text{app}}$ over all training shape. **b**) Shape model optimality with respect to $\mathcal{F}_{\text{shape}}$. **c**) Box-plot of the surface approximation errors $\mathcal{F}_{\text{app}}$. **d**) Box-plot of the mesh quality $\mathcal{F}_{\text{tri}}$.

ticle. The regularisation also improves the approximation of the training shapes by making the resulting dense meshes more homogeneous.

In the proposed method, the parameters of the model are chosen globally, meaning that the weighting of the prior and the observation model is the same over the entire surface. It is possible that a model with site-specific weighting α_i would provide even better results. The site-specific weighting could be learned from a training set based on multiple expectation-maximisation parameter analysis. This is, however, out of the scope of this article.

Acknowledgements

The work was supported by the Academy of Technical Sciences by grant number EF915. The authors also thank Søren Laugesen and Claus Nielsen from Research Centre Eriksholm, Oticon A/S for guidance and data. The Visualization Toolkit (`http://www.vtk.org/`) was used as software platform and for visualisations.

APPENDIX D

Using a Shape Model in the Design of Hearing Aids

Rasmus R. Paulsen, Claus Nielsen,
Søren Laugesen, and Rasmus Larsen

Abstract

Today the design of custom completely-in-the-canal hearing aids is a manual process and therefore there is a variation in the quality of the finished hearing aids. Especially the placement of the so-called faceplate on the hearing aid strongly influences the size and shape of the hearing aid. Since the future hearing aid production will be less manual there is a need for algorithms that mimic the craftsmanship of skilled operators. In this paper it is described how a statistical shape model of the ear canal can be used to predict the placement of the faceplate on a hearing aid made for a given ear canal. The shape model is a point distribution model built using a training set of shapes with manually placed landmarks. An interpolation method is used to generate dense landmark correspondence over the training set prior to building the shape model. Faceplates have also been placed on the training shapes by a skilled operator. These faceplate planes are aligned to the average shape from the shape model and an average faceplate plane is calculated. Given a surface representation of a new ear canal, the shape model is fitted using a combination of the iterative closest point algorithm and the active shape model approach. The average faceplate from the training set can now be placed on the new ear canal using the position of the fitted shape model. A leave-one-out study shows that the algorithm is able to produce results comparable to a human operator.

D.1 Introduction

Today the production of custom completely-in-the-canal (CIC) hearing aids is a manual process. For a CIC hearing aid, all components reside in a custom-made shell that sits in the ear of the user. The shell is cast in a hard acrylic material based on an ear impression and then ground down to the desired size. The shell is then glued together with the so-called faceplate in which the battery compartment and the microphone are mounted from the factory. The remaining internal components of the hearing aid: the loudspeaker, the amplifier and the ventilation tube are positioned inside the shell. All these processes are done by hand and this induces a variation in the quality of the final products. See [55] for a more thorough introduction to CIC hearing aids. An actual faceplate and the corresponding CAD model can be seen in figure D.1.

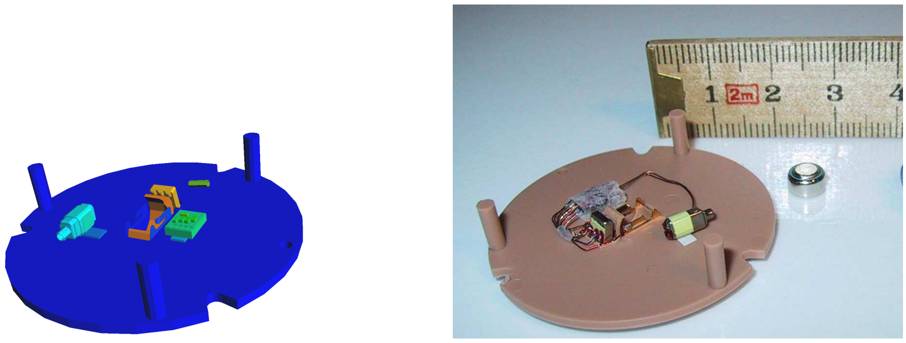

Figure D.1: The faceplate used in the Oticon Adapto CIC hearing aid.

In Fig. D.2 two CIC hearing aids made for the same ear canal are seen. It is seen that the left CIC is smaller than the one to the right. The size difference is mainly due to the placement of the faceplate. The placement of the faceplate also influences the visual appearance of the finished CIC in the ear. These two hearing aids come from the *Eriksholm clinic* and are made following the standard procedure. Since they are not made for any special purposes, they reflect the standard variance seen in the shapes of final CIC hearing aids. Even though a large part of the elderly population suffers from hearing loss there is a social stigma associated with having a hearing aid. One way to alleviate that problem is to convince people that it is acceptable to wear a hearing aid. Another way is to design hearing aids to be as discreet as possible.

Manufacturers of hearing aids have made initial testing of rapid prototyping of hearing aid shells using laser scans of ear impressions [254, 210]. In this process the hearing aid is designed using a custom computer aided design program. This means that the quality of the final product is still dependent of the intuition and skills of the human operator. Thus, an automatic method capable of mimicking the craftsmanship of the best skilled operators would be useful in the design process.

In this paper it is described how a statistical shape model of the human ear canal is used to predict the placement of the faceplate on a custom CIC hearing aid. The input data consists of expert placements of faceplates and the goal is to generate a system that is able to mimic the expert placements based on the assumption that the expert placements are related to the anatomy of the ear canals.

Figure D.2: Two CIC hearing aids made for the same ear canal. It is seen that the left CIC is smaller than the one to the right. The size difference is mainly due to the placement of the faceplate. It is seen that the visual appearance of the hearing aid in the ear is strongly influenced by the size.

The statistical modelling of shapes has in recent years been heavily influenced by the development of learning based models. A fairly sophisticated learning based deformable template model is the Active Shape Model developed by Cootes et al. in 1995, which uses principal component analysis of the shape space [61].

This method has previously been used to build a full 3D statistical shape model of the human ear canal [201]. The model is based on a set of 29 laser scanned ear impressions. Anatomical landmarks were placed on the surfaces of this training set and an interpolation method was used to generate a dense surface description. The method is similar to the methods described in [184] and [143]. The method has later been extended to include a Markov Random Field restoration step to remove artifacts arising due to a closest point correspondence step used in the original method [127, 199]. A thorough description of the anatomy of the human ear canal can be found in [17].

D.2 Method

D.2.1 Expert Faceplate Placement

Using a custom-made surface annotation tool the second author, who is an expert in the anatomy of the ear canal has placed faceplates on the 29 ear canals used in the previous study [201]. The surface of the ear canal is here thought of as being equal to the acrylic shell used in the production of CIC hearing aids. This means that the faceplate is placed on the ear canal where the acrylic shell would have been cut off if a faceplate should be mounted. In this study the faceplate is treated as an infinite plane and it is placed where it is optimal from a cosmetical point of view without taking the components on the faceplate into account. In this respect optimal means that if the faceplate is placed at the entrance of the ear canal around the first bend, the CIC will be practically invisible. A deeper placement will not make it less visible but will only make the CIC more difficult to manipulate for the user. Two ear canals with faceplate planes are seen in Fig. D.3a.

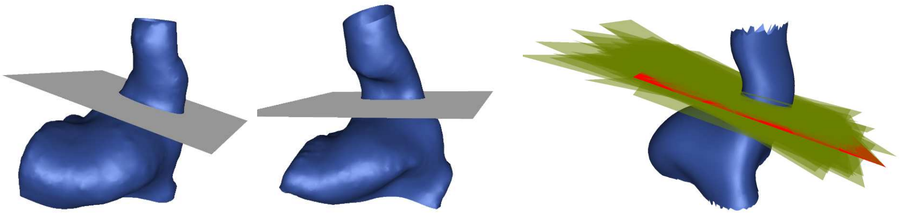
(a) (b)

Figure D.3: **a)** The faceplate plane placed in two ear canals. **b)** Planes from all canals in the training set aligned to the average ear canal. The estimated average plane is shown with red.

D.2.2 Statistical Shape Model

An ear canal is approximated using a surface mesh containing 3001 vertices. In the shape analysis the ear canal is represented as a vector of concatenated x, y and z coordinates $\mathbf{x}_i = [x_{i1}, y_{i1}, z_{i1}, \ldots, x_{in}, y_{in}, z_{in}]^T$, $i = 1, \ldots, s$, where n is the number of vertices and s is the number of shapes. The statistical shape model of the ear canal basically consists of an average ear canal $\overline{\mathbf{x}}$ and a set of orthogonal translation vectors arranged in a matrix $\Phi = [\phi_1|\phi_2|\ldots|\phi_t]$. The average ear canal is calculated on the basis of the Procrustes [113] aligned training ear canals and Φ is found by a principal component analysis of the Procrustes aligned shapes. It was found that $t = 7$ modes of variation was enough to sufficiently explain the variation seen in the training data [201]. A new shape exhibiting the variance seen in the training set is synthesised by adding a combination of eigenvectors to the average shape $\mathbf{x}_{\text{new}} = \overline{\mathbf{x}} + \Phi\mathbf{b}$, where $\mathbf{b}$ is a vector of weights controlling the modes of shape variation. In this article a size-and-shape model of the ear canal is used meaning that the size variation of ear canal is included in Φ [83].

D.2.3 Alignment of Faceplates

The rigid body transformation, $\mathbf{T}_i$, that in a least squares sense aligns ear canal $\mathbf{x}_i$ to the average ear canal is also applied to the faceplate plane of that shape, thus transforming the faceplate plane to the average ear canal. All the faceplate planes from the training set transformed to the average canal and the average ear canal can be seen in Fig. D.3b.

A plane can be defined as the set of points satisfying:

$$P = \{\mathbf{x} \in \mathbb{R}^3 | F(\mathbf{x}) = \lambda Ax + \lambda By + \lambda Cz + \lambda D = 0, \lambda \neq 0\}, \tag{D.1}$$

where the normal vector of the plane is $\mathbf{n} = (A, B, C)$ and $\mathbf{x} = (x, y, z)$ is a point. This means that a plane can be represented as a parameter vector, $\mathbf{p} = (A, B, C, D)$, which is defined up to a normalising factor $\lambda \neq 0$, and that can be normalised to have unit length, $\|\mathbf{p}\| = 1$. After normalising, all planes in the training set are now lying on the 3 Dimensional hypersphere.

Using this representation, planes can be looked upon as points of $P^3\mathbb{R}$, the real projective space of dimension 3 [103]. A metric can now be established in this differential manifold and thus it is possible specify a distance between two infinite planes, $\mathbf{p}_i$ and $\mathbf{p}_j$; namely the arc-length on the hypersphere, $d_a = \min(\arccos(\mathbf{p}_i, \mathbf{p}_j), \arccos(-\mathbf{p}_i, \mathbf{p}_j))$. Note that it is necessary to handle that a plane $\mathbf{p}$ is equal to the plane $-\mathbf{p}$. An approximate distance measure is $d_e = \min(\|\mathbf{p}_i - \mathbf{p}_j\|, \|\mathbf{p}_i + \mathbf{p}_j\|)$. An average plane $\overline{\mathbf{p}}$ can be determined from:

$$\overline{\mathbf{p}} = \arg\min_{\mathbf{p}} \sum_i d(\mathbf{p}, \mathbf{p}_i), \;\; \|\overline{\mathbf{p}}\| = 1, \tag{D.2}$$

and is found by gradient descent optimisation with d_e as the distance function. Planevectors not pointing into the same hemisphere as the current estimate of $\overline{\mathbf{p}}$ are negated prior to each iteration of the optimisation algorithm. The average ear canal and the estimated average faceplate plane can be seen in D.3b. For visualisation purposes the planes are represented as finite planes limited to the proximity of the ear canal. From an anatomical viewpoint the placement of the average plane in the average ear canal looks sensible.

D.2.4 Shape Fitting and Recognition

The statistical shape model built previously can be fitted to new ear canals not included in the training set following the approach used in the active shape models (ASM) [61]. The following method is similar to the method described in [143]. Given a sampled surface of an ear canal not included in the training set, $\mathbf{x}_{\text{target}}$, the goal is to fit a model mesh, $\mathbf{x}_{\text{model}}$ to $\mathbf{x}_{\text{target}}$. The fitting procedure consists of a combination of the iterative closest point transformation (ICP) [25, 262] and a shape deformation using, $\mathbf{x}_{\text{deform}} = \bar{\mathbf{x}} + \Phi \mathbf{b}_f$. In each stage the model mesh is therefore represented by a global transform, $\mathbf{T}_f$, and a set of deformation parameters, $\mathbf{b}_f$: $\mathbf{x}_{\text{model}} = \mathbf{T}_f(\bar{\mathbf{x}} + \Phi \mathbf{b}_f)$. The size-and-shape model is used and therefore $\mathbf{T}_f$ is a rigid-body transform [83]. Initially the average ear canal ($\mathbf{b}_f = \mathbf{0}$) is placed in the scene and then iteratively transformed and deformed to fit the target ear canal. In each iteration $\mathbf{T}_f$ is found by ICP. The ICP algorithm initially aligns the centre of mass of the model mesh to the centre of mass of the target mesh and then the closest point on the target surface is found for all points in the model mesh. The surface of the target ear canal is typically acquired using a laser scanner and therefore consists of a large number of points and triangles. The closest point on the target surface is found by the *vtkCellLocator* class found in the Visualization Toolkit [219]. It uses a uniform-level octree subdivision [188], where each octant carries an indication of whether it is empty or not, and each leaf octant carries a list of the polygons inside of it. Therefore the closest point is found as a point lying on a triangle and not just as a vertex. $\mathbf{T}_f$ is found as the transformation that minimises the distances between the model mesh and the closest points on the target mesh in a least squares sense [133].

After the model mesh has been rigidly aligned to the target mesh the closest point on the target shape is found for all points in the model mesh. The collection of closest points yields a new shape, $\mathbf{x}'$. This new shape is transformed back to alignment with the shape model using the inverse transformation: $\mathbf{x}'' = \mathbf{T}_f^{-1}(\mathbf{x}')$. The model shape is now deformed to look as much like $\mathbf{x}''$ as possible, but still being in the allowed shape space. This is done by finding the parameter vector, by back-projecting $\mathbf{x}''$ on the eigenvector space: $\mathbf{b}_f = \Phi^T(\mathbf{x}'' - \bar{\mathbf{x}})$. The parameters found are then clamped to three standard deviations and the new model mesh is synthesised using $\mathbf{x}_{\text{deform}} = \bar{\mathbf{x}} + \Phi \mathbf{b}_f$ and used in the next iteration.

The quality of the fit is defined to be the square root of the summed squared distances from all the points in the model mesh to the closest point on the target mesh

$$\mathcal{F} = (\sum_{i}^{N} d^2(p_i^m, p_{\text{closest}}^t))^{1/2}, \tag{D.3}$$

where $d^2(p_i^m, p_i^t)$ is the squared Euclidean distance from point i in the model shape to the closest point on the surface of the target shape. The iteration stops when the change in $\mathcal{F}$ is sufficiently small. The parameter vector describing the approximated target shape, $\mathbf{b}_f$, can be used to test if the found shape belongs to the same class of shapes as the training set [61].

The algorithm described previously does not handle local minima very well and tends to get stuck if the initial orientation of the model is very different from the orientation of the target shape. To overcome this problem a guess of the starting placement is made by starting ICP with the model pre-transformed in 24 different configurations and then selecting the ICP with the best initial fit, $\mathcal{F}$. The 24 configurations are made by an initial rotation around the x-axis followed by a rotation around either the y- or the z-axis. The allowed rotations are 90,180 and 270 degrees. So it is equal to the object first being rotated around itself and then rotated to lie on one of the 6 axis of symmetry of a cube. This is a primitive and brute-force approach, but it works very well. Examples of ICP fits with different pre-rotations can be seen in Fig. D.4. It is seen that the pre-rotation used in the top row is ideal.

D.2.5 Prediction of Faceplate Placement

The fitting procedure described above can also be used to place a faceplate plane on a new ear canal. The average faceplate plane, $\overline{\mathbf{p}}$, associated with the average ear canal $\overline{\mathbf{x}}$ can be fitted to the new ear canal using the transform used to fit the model shape to the new ear canal. The fitting consists of a rigid body transform $\mathbf{T}_f$ and a deformation expressed with $\mathbf{b}_f$. It would be ideal to use both the rigid transformation and the shape deformation in the prediction of the faceplate placement. In this work the prediction is limited to the rigid transformation meaning that the predicted plane is calculated by applying $\mathbf{T}_f$ to $\overline{\mathbf{p}}$. A faceplate plane placed by the algorithm in a new ear canal can be seen together with the fitted model mesh in Fig. D.5.

The fitting and faceplate plane prediction algorithm is outlined in algorithm 2.

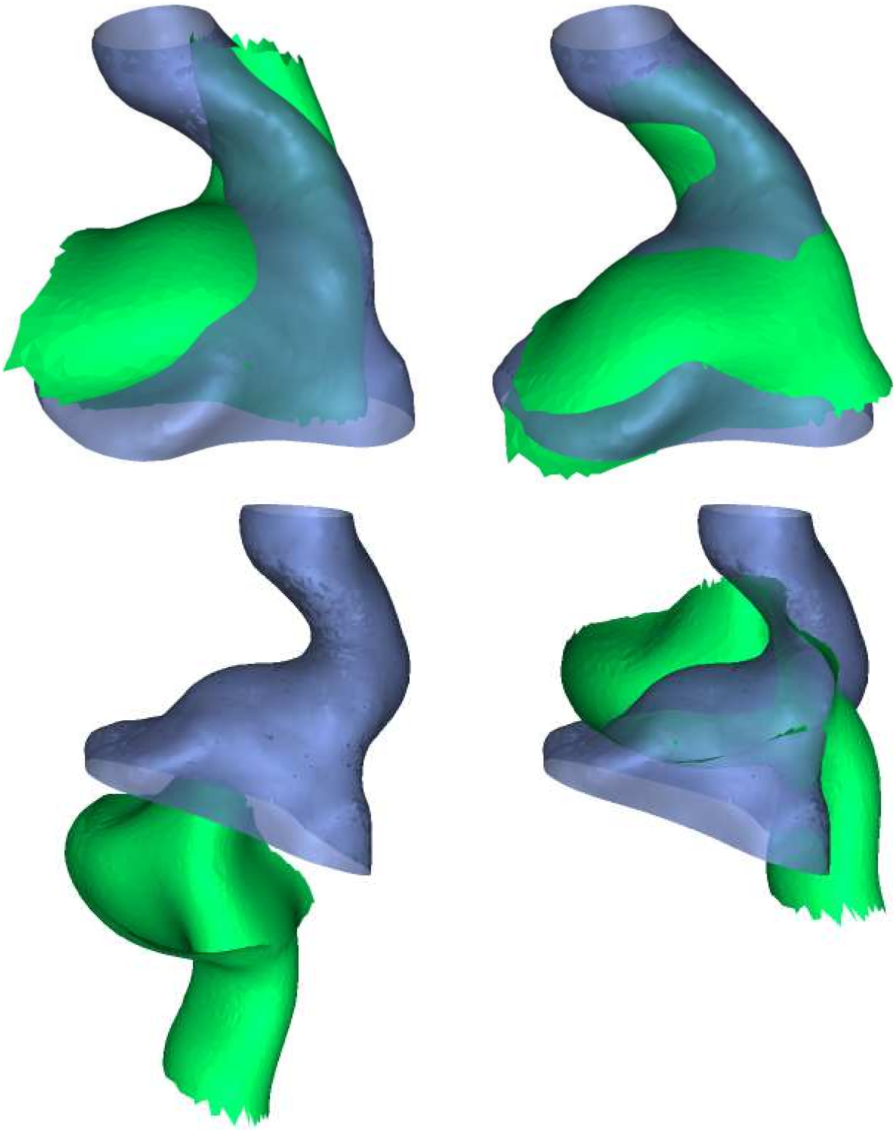

Figure D.4: ICP fitting. Here the green model ear is fitted to the blue target ear canal. The initial placement of the model ear is seen to the left and after ICP to the right. The fit quality after the converged ICP shown in the top row is $\mathcal{F} = 0.722$ and $\mathcal{F} = 2.50$ for the one in the bottom row.

Algorithm 2 Fitting the Shape Model to a Target Surface, $\mathbf{x}_{\text{target}}$, and Predict Faceplate Placement

```
$\mathbf{b}_f = \mathbf{0}, \mathbf{T}_f = \mathbf{I} \rightarrow \mathbf{x}_{\text{model}} = \overline{\mathbf{x}}$
Determine pre-transformation $\mathbf{T}_f$ by multiple ICP
while Not convergence do
    $\mathbf{x}_{\text{model}} = \mathbf{T}_f(\bar{\mathbf{x}} + \Phi\mathbf{b}_f)$
    Determine $\mathbf{T}_i$ using ICP so $\mathbf{x}_{\text{model}}$ fits $\mathbf{x}_{\text{target}}$.
    Update $\mathbf{T}_f$ with $\mathbf{T}_i$ and update $\mathbf{x}_{\text{model}}$
    For each point in $\mathbf{x}_{\text{model}}$ find the closest point on the surface of $\mathbf{x}_{\text{target}}$
    Generate a new shape $\mathbf{x}'$ of these closest points
    Apply $\mathbf{T}_f^{-1}$ to $\mathbf{x}'$ generating $\mathbf{x}''$
    Set $\mathbf{b}_f = \Phi^T(\mathbf{x}'' - \bar{\mathbf{x}})$
    Convergence if $\Delta\mathcal{F}$ is small
end while
Final fitted model: $\mathbf{x}_{\text{fit}} = \mathbf{T}_f(\bar{\mathbf{x}} + \Phi\mathbf{b}_f)$
Apply $\mathbf{T}_f$ to $\overline{\mathbf{p}}$ to get the predicted faceplate plane for $\mathbf{x}_{\text{target}}$
```

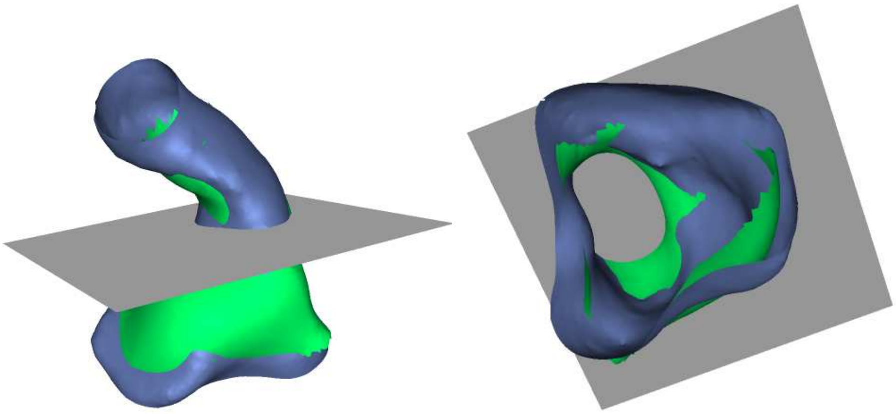

Figure D.5: The shape model fitted to a new ear canal and the predicted faceplate plane. The target shape is blue and the fitted model is green.

D.3 Results

D.3.1 General Observations

In Fig. D.6 there is a visual comparison between the expert placed faceplate and the predicted faceplate placement. The three cases shown are the worst, the best and a an average case. From a visual point of view all three results are satisfying.

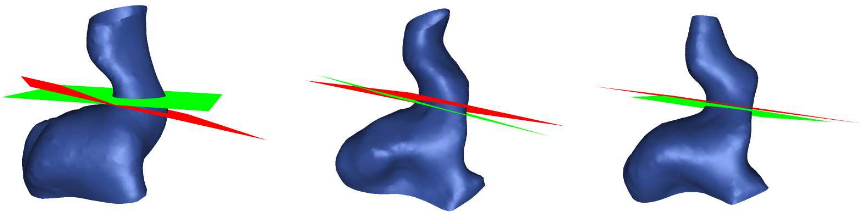

Figure D.6: Predicted faceplate planes (red) and expert placed faceplate planes (green). From left to right the worst, an average and the best predictions are shown. Quantitatively, the prediction errors evaluated from Eq. (D.4) are 11.8°, 5.2°and 2.1°, respectively.

D.3.2 Leave-One-Out Analysis

To supplement the visual validation of the results a leave-one-out study has been performed. In this study the faceplate placement is predicted for the i-th ear canal using Alg. 2, where the statistical shape model has been built using the 28 other ear canals. In order to compare the predicted faceplate placement $\mathbf{p}_a$ with the expert placement $\mathbf{p}_e$ a candidate distance measure is $d(\mathbf{p}_a, \mathbf{p}_e) = \|\mathbf{p}_a - \mathbf{p}_e\|$. This distance measure is not practical because it is difficult to compare the distance to a known reference. An alternative approach is to calculate the angle, α, between the predicted and the expert placed plane using the plane normals:

$$\arccos \alpha = \frac{A_a A_e + B_a B_e + C_a C_e}{(A_a^2 + B_a^2 + C_a^2)^{1/2}(A_e^2 + B_e^2 + C_e^2)^{1/2}} \tag{D.4}$$

The angle differences between the expert placements and the predicted placements are shown in Fig. D.7. The average angle difference is 6.3°and the practical consequences of these prediction errors can be judged from Fig. D.6.

Using the angle in the cross validation is not optimal. A better difference measure would be the volume of the part of the ear canal delimited by the expert and the predicted faceplate plane. This is, however, not used due to its computational complexity.

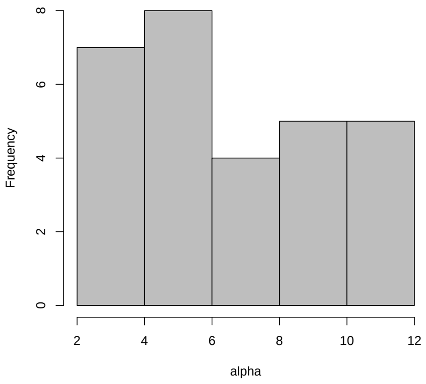

Figure D.7: Histogram of α values for the training set.

D.4 Summary and Conclusions

The present study has two main outcomes. First, a proof-of-concept has been presented regarding automated, cosmetically motivated CIC faceplate placement based on a statistical shape model of the ear canal shape. Secondly, the expert faceplate placements and the resulting model consider the placement of a faceplate without components (microphone, battery drawer, etc.). Hence, the resulting faceplate placements may serve as inspiration for the component layout of future faceplates.

The presented method places the plane using a rigid transformation based on the translation and orientation of the transformed and deformed model ear canal. It does not take into account the anatomy of the target ear canal contained in the shape model. It should be examined if a multivariate correlation can be found between the shape vector and the faceplate plane parameters.

Acknowledgements

The work was supported by the Academy of Technical Sciences, grant number EF915. All software is developed using The Visualization Toolkit[219]. The Procrustes analysis and the Principal Component Analysis algorithms have been co-developed with Tim Hutton [143] and added to the official VTK release. Thanks to the EPIDAURE group at INRIA Sophia-Antipolis for letting me stay at their group and for numerous good discussions.

Appendix E

Software

The Visualisation Toolkit (VTK) [219] has been used as the basis for the software developed in this thesis. VTK is an open source, freely available software system for 3D computer graphics, image processing, and visualisation. It consists of a C++ class library, and several interpreted interface layers including Tcl/Tk, Java, and Python. The applications are developed using VTK, C++, and TCL/TK [252, 198].

E.1 IMM Surface Annotation Toolkit

A simple tool for placing landmarks on the surface of 3D objects. Landmarks can be placed, moved, and deleted. Finally, the landmark coordinates can be saved in VTK format. A screen-shot can be seen in figure E.1.

E.2 Faceplate Placement Toolkit

This application is an extension to the annotation toolkit. A CAD model of a faceplate can be placed in the ear canal. It is possible to clip the ear canal

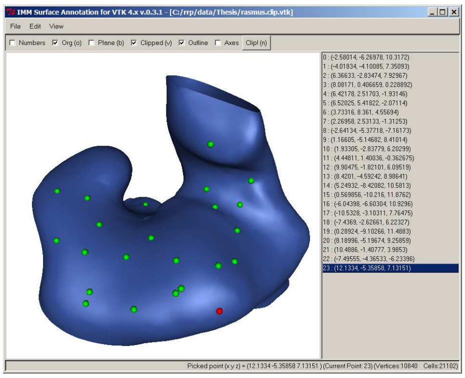

```
0 : (-2.58014, -6.26978, 10.3172)
1 : (-4.01834, -4.10085, 7.35093)
2 : (6.36633, -2.83474, 7.92967)
3 : (8.08171, 0.406659, 0.228892)
4 : (6.42178, 2.51703, -1.93146)
5 : (6.52025, 5.41822, -2.07114)
6 : (3.73316, 8.361, 4.55694)
7 : (2.26958, 2.53133, -1.31253)
8 : (-2.64134, -5.37718, -7.16173)
9 : (1.16605, -5.14682, 8.41014)
10 : (1.93305, -2.83779, 6.20299)
11 : (4.44811, 1.40036, -0.362675)
12 : (9.90475, -1.82101, 6.09519)
13 : (8.4201, -4.59242, 8.98641)
14 : (5.24932, -8.42082, 10.5813)
15 : (0.569856, -10.216, 11.8762)
16 : (-6.04398, -6.60304, 10.9296)
17 : (-10.5328, -3.10311, 7.76475)
18 : (-7.4369, -2.62661, 6.22327)
19 : (0.28924, -9.10266, 11.4883)
20 : (8.18996, -5.19674, 9.25859)
21 : (10.4886, -1.40777, 3.9853)
22 : (-7.49555, -4.36533, -6.23396)
23 : (12.1334, -5.35858, 7.13151)
```

```
Picked point (x y z) = (12.1334 -5.35858 7.13151 ) (Current Point: 23) (Vertices:10840    Cells:21102)
```

Figure E.1: Landmarks are placed on an ear canal using the annotation toolkit.

with the faceplate, to give an idea of the size of the shell. Furthermore, it is possible to make the different objects more or less transparent. Finally, the faceplate position can be stored in VTK format. The application can be seen in figure E.2.

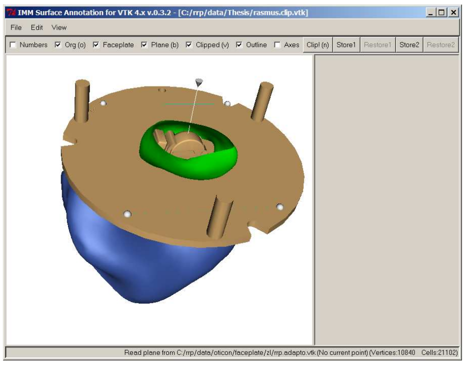

```
Read plane from C:/rrp/data/oticon/faceplate/zl/rrp.adapto.vtk (No current point) (Vertices:10840    Cells:21102)
```

Figure E.2: The CAD tool used by the operators to place faceplates.

E.3 Faceplate Placer

Given an ear canal, this application places a faceplate. The application mimics the routines used by expert operators. As seen in figure E.3, the visual interface makes it possible to see the evolution of the objective function over time. In addition, the outline of the shell can be seen on the faceplate.

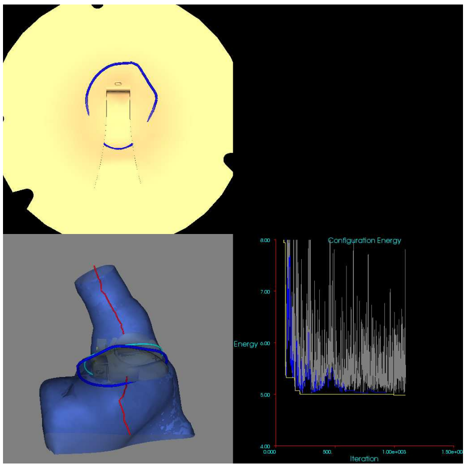

Figure E.3: The visual interface to the faceplate placement algorithm.

E.4 3D Model Viewer

A viewer for 3D surface models has been co-developed with Per R. Andresen [8]. It is possible to load several 3D models into the same scene and customise their appearance. The application contains several features including movie creation and the ability to export the scene to a RenderMan file[1] . Furthermore, advanced scripting is available via the inbuilt TCL/TK interface. A scene with several 3D objects can be seen in figure E.4.

E.5 Shape Model Viewer

An application that can visualise the modes of variation of a 3D surface shape model has been co-developed with Karl Skoglund [226]. The modes of variation are controlled by sliders as seen in figure E.5.

---

[1] A number of illustrations in this thesis are produced with the Blue Moon Rendering Tools, which are a collection of programs that render 3D scene models. The file format used is specified by Pixar and called the RenderMan Interface Specification.

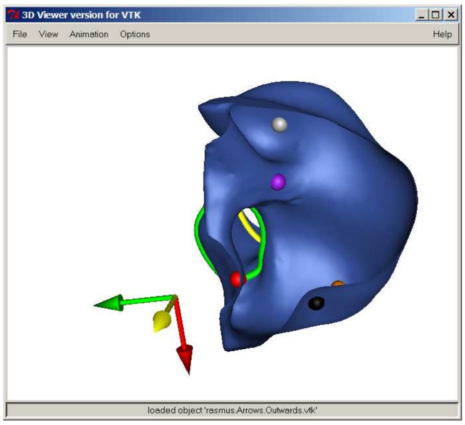

loaded object 'rasmus.Arrows.Outwards.vtk'

Figure E.4: Various 3D models shown in the viewer.

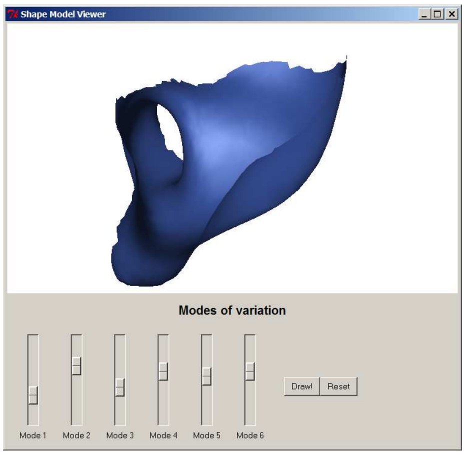

Figure E.5: The modes of variation of a 3D shape model are visualised.

E.6 Markov Random Field Visual Interface

A visual interface to the Markov Random Field algorithm described in appendix C has been created. As seen in figure E.6 it is possible to view the change in representation ability and polygonisation of the target shape.

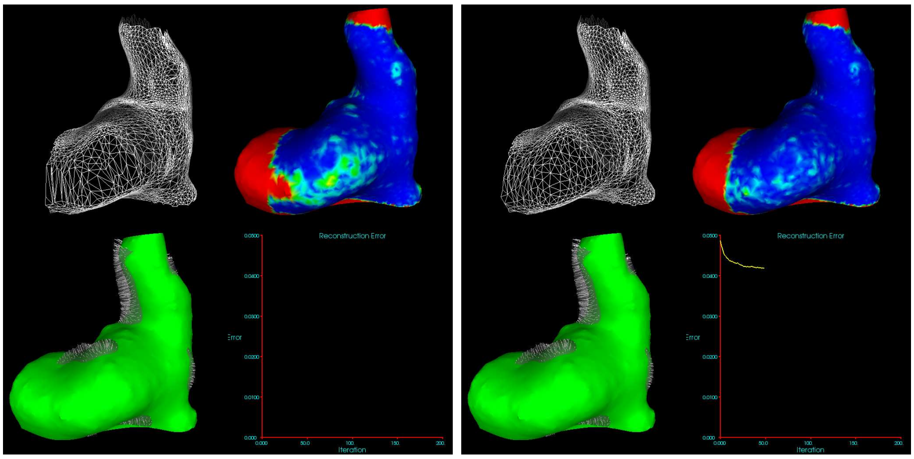

Figure E.6: Markov Random Field Regularisation Visual Interface.

E.7 VTK classes

A number of VTK classes have been developed during the thesis. They are available from the author's website.

vtkPolyDataSingleSourceShortestPath

vtkPolyDataSingleSourceShortestPath is a filter that takes as input a polygonal mesh and performs a single source shortest path calculation. Dijkstra's algorithm is used. The implementation is similar to the one described in [72]. Some minor enhancements are added though. Not all vertices are pushed on the heap at start; instead, a front set is maintained. The heap is implemented as a binary heap. The output of the filter is a set of lines describing the shortest path from the start vertex to the end vertex.

vtkPrincipalAxisTransform

vtkPrincipalAxisTransform generates a transform that scales, translates, and rotates a given object to the principal axis of the input data. If the input data is a Gaussian distributed point cloud and the transformation is applied to a unit sphere, the transformed sphere will show the covariance structure of the point cloud. It is possible to specify if the transform shall include rotation, translation, scaling, or all of them.

vtkProcrustesAlignmentFilter

vtkProcrustesAlignmentFilter is a filter that takes a set of pointsets and aligns them in a least-squares sense to their mutual mean. The algorithm is iterated until convergence, as the mean must be recomputed after each alignment. vtkProcrustesAlignmentFilter is an implementation of [113]. This class was co-developed with Tim Hutton [143] and has been added to the official VTK distribution.

vtkPCAAnalysisFilter

vtkPCAAnalysisFilter is a filter that takes as input a set of aligned pointsets and performs a principal component analysis of the coordinates. This can be used to visualise the major or minor modes of variation seen in a set of similar biological objects with corresponding landmarks. vtkPCAAnalysisFilter is designed to work with the output from the vtkProcrustesAnalysisFilter. vtkPCAAnalysisFilter is an implementation of (for example) [61]. This class was co-developed with Tim Hutton [143] and has been added to the official VTK distribution.

List of Figures

List of Tables

Bibliography

[1] L. S. Alvord and B. L. Farmer. Anatomy and orientation of the human external ear. *J. Am. Acad. Audiol.*, 8:383–390, 1997.

[2] L. S. Alvord, R. Morgan, and K. Cartwright. Anatomy of an earmold: A formal terminology. *J. Am. Acad. Audiol.*, 8:100–103, 1997.

[3] N. Amenta, S. Choi, and R. Kolluri. The power crust. In *Proc. ACM Symposium on Solid Modeling*, pages 249–260, 2001.

[4] N. Amenta, S. Choi, and R. Kolluri. The power crust, unions of balls, and the medial axis transform. *Computational Geometry: Theory and Applications*, 19(2–3):127–153, 2001.

[5] P. R. Andresen. *Surface-bounded growth modeling applied to human mandibles.* PhD thesis, Informatics and Mathematical Modelling, Technical University of Denmark, DTU, 1999.

[6] P. R. Andresen, F. L. Bookstein, K. Conradsen, B. K. Ersbøll, J. Marsh, and S. Kreiborg. Surface-bounded growth modeling applied to human mandibles. *IEEE Transactions on Medical Imaging*, 19(11):1053–1063, November 2000.

[7] P. R. Andresen and M. Nielsen. Non-rigid registration by geometry constrained diffusion. In *Proceedings of Medical Image Computing and Computer Assisted Intervention*, volume 1679, pages 533–543. Springer-Verlag, 1999.

[8] P. R. Andresen and M. Nielsen. Non-rigid registration by geometry-constrained diffusion. *Medical Image Analysis*, 5(2):81–88, 2001.

[9] S. Angenent, S. Haker, A. Tannenbaum, and R. Kikinis. On area preserving mappings of minimal distortion. In T. Djaferis and I. Schick, editors, *System Theory: Modeling, Analysis, and Control*, pages 275–287. Kluwer, Holland, 1999.

[10] S. Angenent, S. Haker, A. Tannenbaum, and R. Kikinis. On the Laplace-Beltrami operator and brain surface flattening. *IEEE Trans. Medical Imaging*, 18:700–711, 1999.

[11] L. Antiga. *Patient-Specific Modeling of Geometry and Blood Flow in Large Arteries.* PhD thesis, Politecnico di Milano. Dipartimento di Bioingegneria, 2002.

[12] L. Antiga, B. Ene-Iordache, and A. Remuzzi. Centerline computation and geometric analysis of branching tubular surfaces with application to blood vessel modeling. In *Proc. Int. Conf. in Central Europe on Computer Graphics, Visualization and Computer Vision*, 2003.

[13] K. S. Arun, T. S. Huang, and S. D. Blostein. Least-squares fitting of two 3-D point sets. *IEEE Transactions on Pattern Analysis and Machine Intelligence*, 9(5):698–700, 1987.

[14] M. A. Audette, F. P. Ferrie, and T. M. Peters. An algorithmic overview of surface registration techniques for medical imaging. *Medical Image Analysis*, 4(3):201–217, 2000.

[15] V. Ayyadevara, D. A. Bourne, K. Shimada, and R. H. Sturges. Interference-free polyhedral configuration for stacking (submitted). *IEEE Transactions on Robotics and Automation*, 2000.

[16] J. A. Bærentzen and H. Aanæs. Computing discrete signed distance fields from triangle meshes. Technical report, Informatics and Mathematical Modelling, Technical University of Denmark, DTU, Richard Petersens Plads, Building 321, DK-2800 Kgs. Lyngby, 2002.

[17] B. B. Ballachanda. *The Human Ear Canal.* Singular Publishing Group, Inc., San Diego, California, 1995.

[18] B. B. Ballachanda. Theoretical and applied external ear accoustics. *J. Am. Acad. Audiol.*, 8:411–420, 1997.

[19] J. A. Batting and C. Grünewaldt. Udvikling af system til scanning af 3D-geometri og generering af cad-model. Master's thesis, Institut for anvendt konstruktion og produktion, DTU, 1997.

[20] J. L. Bentley. Multidimensional binary search trees used for associative searching. *Communications of the ACM*, 18(9):509–517, 1975.

[21] G. van den Bergen. Efficient collision detection of complex deformable models using AABB trees. *Journal of Graphics Tools*, 2(4):1–14, 1997.

[22] J. Besag. Spatial interaction and the statistical analysis of lattice systems. *Journal of the Royal Statistical Society, Series B*, 36:192–236, 1974.

[23] J. Besag. On the statistical analysis of dirty pictures. *Journal of the Royal Statistical Society, Series B*, 48(3):259–302, 1986.

[24] J. Besag. Towards Bayesian image analysis. *Journal of Applied Statistics*, 16(3):395–407, 1989.

[25] P. J. Besl and N.D. McKay. A method of registration of 3D shapes. *IEEE Transactions on Pattern Analysis and Machine Intelligence*, 14(2):239–256, 1992.

[26] M. Betke, H. Hong, D. Thomas, C. Prince, and J. P. Ko. Landmark detection in the chest and registration of lung surfaces with an application to nodule registration. *Medical Image Analysis*, 7(3):265–281, 2003.

[27] A. Blake and M. Isard. *Active Contours.* Springer, 1998.

[28] V. Blanz and T. Vetter. A morphable model for the synthesis of 3D faces. In *Proc. SIGGRAPH*, pages 187–194. ACM, 1999.

[29] F. L. Bookstein. The study of shape transformation after d'arcy thompson. *Math. Biosciences*, pages 177–219, 1977.

[30] F. L. Bookstein. The measurement of biomedical shape and shape change. *Lectures Notes in Biomathematics*, 24, 1978.

[31] F. L. Bookstein. A statistical method for biological shape comparisons. *J. Theoret. Biol.*, 107:475–520, 1984.

[32] F. L. Bookstein. Principal warps: thin-plate splines and the decomposition of deformations. *IEEE Transactions on Pattern Analysis and Machine Intelligence*, 11(6):567–585, 1989.

[33] F. L. Bookstein. Landmark methods for forms without landmarks: localizing group differences in outline shape. *Medical Image Analysis*, 1(3):225–244, 1997.

[34] F. L. Bookstein. Shape and the information in medical images: A decade of the morphometric synthesis. *Computer Vision and Image Understanding*, 66(2):97–118, 1997.

[35] G. Borgefors. Distance transformations in arbitrary dimensions. *Computer Vision, Graphics, and Image Processing*, 27(3):321–345, 1984.

[36] R. Bowden. *Learning non-linear Models of Shape and Motion.* PhD thesis, Dept Systems Engineering, Brunel University, Uxbridge, Middlesex, UB8 3PH, UK., 1999.

[37] C. Brechbühler, G. Gerig, and O. Kübler. Towards representation of 3D shape: Global surface parametrization. In *Proc. Internatinal Workshop on Visual Form*, 1991.

[38] C. Brechbühler, G. Gerig, and O. Kübler. Surface parametrization and shape description. In *Proc. Visualization in Biomedical Computing*, Chapel Hill, North-Carolina, October 1992.

[39] C. Brechbühler, G. Gerig, and O. Kübler. Parametrization of closed surfaces for 3-D shape description. *Computer Vision and Image Understanding*, 61:154–170, 1995.

[40] A. D. Brett and C. J. Taylor. A method of automated landmark generation for automated 3D PDM construction. In *Proc. British Machine Vision Conference*, pages 914–923, 1998.

[41] A. D. Brett and C. J. Taylor. A framework for automated landmark generation for automated 3D statistical model construction. In *Proc. Information Processing in Medical Imaging*, pages 376–381, 1999.

[42] A. D. Brett and C. J. Taylor. Construction of 3D shape models of femoral articular cartilage using harmonic maps. In *Proc. MICCAI*, pages 1205–1214, 2000.

[43] M. de Bruijne, B. van Ginneken, W. J. Niessen, J. B. A. Maintz, and M. A. Viergever. Active shape model based segmentation of abdominal aortic aneurysms in CTA images. In *SPIE*, volume 4684, pages 463–474, 2002.

[44] M. de Bruijne, B. van Ginneken, W. J. Niessen, and M. A. Viergever. Adapting active shape models for 3D segmentation of tubular structures in medical images. In *Proc. Information Processing in Medical Imaging*, volume 2732, pages 136–147. Springer, 2003.

[45] E. K. Burke, P. I. Cowling, and R. Keuthen. New models and heuristics for component placement in printed circuit board assembly. In *Proc. Information Intelligence and Systems*, pages 133–140, 1999.

[46] J. Cagan, D. Degentesh, and S. Yin. A simulated annealing-based algorithm using hierarchical models for general three-dimensional component layout. *Computer Aided Design*, 30(10):781–790, September 1998.

[47] J. Cagan, K. Shimada, and S. Yin. A survey of computational approaches to three-dimensional layout problems (submitted). *Computer-Aided Design*, 2001.

[48] M. I. Campbell, C. H. Amon, and J. Cagan. Optimal Three-Dimensional placement of heat generating electronic component. *Journal of Electronic Packaging*, 119(2):106–113, 1997.

[49] J. C. Carr, R. K. Beatson, J. B. Cherrie, T. J. Mitchell, W. R. Fright, B. C. McCallum, and T. R. Evans. Reconstruction and representation of 3D objects with radial basis functions. In *Proc. SIGGRAPH*, pages 67–76, 2001.

[50] J. C. Carr, R. K. Beatson, B. C. McCallum, W. R. Fright, T. J. McLennan, and T. J. Mitchell. Smooth surface reconstruction from noisy range data. In *Proc. ACM GRAPHITE*, pages 119–126, 2003.

[51] R. B. Cattel. The scree test for the number of factors. *Mult. Behav. Res*, 1:245–276, 1966.

[52] A. Caunce and C. J. Taylor. Building 3D sulcal models using local geometry. *Medical Image Analysis*, 5(1):69–80, 2001.

[53] F. Cazals and M. Pouget. Estimating differential quantities using polynomial fitting of osculating jets. Technical report, Institut National de Recherche en Informatique et en Automatique, 2003.

[54] M. Chasin. The acoustics of CIC hearing aids. In M. Chasin, editor, *CIC Handbook*, pages 69–81. Singular Publishing Group, Inc., 1997.

[55] M. Chasin. *CIC Handbook*. Singular Publishing Group, Inc., San Diego, California, 1997.

[56] C. Cherniak. Component placement optimization in the brain. *Journal of Neuroscience*, 14:2418–2427, 1994.

[57] H. Cohn and M. Fielding. Simulated annealing: searching for an optimal temperature schedule. *SIAM Journal on Optimization*, 9(3):779–802, 1999.

[58] T. F. Cootes. Statistical models of appearance for computer vision. Technical report, Division of Imaging Science and Biomedical Engineering, University of Manchester, March 2004.

[59] T. F. Cootes. Timeline of developments in algorithms for finding correspondences across sets of shapes and images. Technical report, Division of Imaging Science and Biomedical Engineering, University of Manchester, March 2004.

[60] T. F. Cootes, C. Beeston, G. J. Edwards, and C. J. Taylor. A unified framework for atlas matching using active appearance models. In *Proc. Information Processing in Medical Imaging*, pages 322–333. Springer-Verlag, 1999.

[61] T. F. Cootes, D. Cooper, C. J. Taylor, and J. Graham. Active shape models - their training and application. *Computer Vision and Image Understanding*, 61(1):38–59, 1995.

[62] T. F. Cootes, D. H. Cooper, C. J. Taylor, and J. Graham. A trainable method of parametric shape description. *Image and Vision Computing*, 10:289–294, June 1992.

[63] T. F. Cootes, G. Edwards, and C. J. Taylor. A comparative evaluation of active appearance model algorithms. In *Proc. British Machine Vision Conf.*, volume 2, pages 680–689, 1998.

[64] T. F. Cootes, G. J. Edwards, and C. J. Taylor. Active appearance models. In *Proc. European Conf. on Computer Vision*, volume 2, pages 484–498. Springer, 1998.

[65] T. F. Cootes, G. J. Edwards, and C. J. Taylor. Comparing active shape models with active appearance models. In *Proc. British Machine Vision Conf.*, pages 173–182, 1999.

[66] T. F. Cootes and C. J. Taylor. Active shape models – 'smart snakes'. In *Proc. British Machine Vision Conf.*, pages 266–275, 1992.

[67] T. F. Cootes and C. J. Taylor. Combining point distribution models with shape models based on finite element analysis. *Image and Vision Computing*, 13(5):403–409, 1995.

[68] T. F. Cootes and C. J. Taylor. Statistical models of appearance for medical image analysis and computer vision. In *Proc. SPIE Medical Imaging*, volume 1, pages 236–248. SPIE, 2001.

[69] T. F. Cootes, C. J. Taylor, D. H. Cooper, and J. Graham. Training models of shape from sets of examples. In *British Machine Vision Conference: Selected Papers 1992*, pages 9–18, Berlin, 1992. Springer-Verlag.

[70] T. F. Cootes, C. J. Taylor, and A. Lanitis. Active shape models: Evaluation of a multi-resolution method for improved image search. In *Proc. British Machine Vision Conf.*, pages 327–336, 1994.

[71] T. F. Cootes, C. J. Taylor, and A. Lanitis. Multi-resolution search using active shape models. In *Proc. 12th Int. Conf. on Pattern Recognition*, volume 1, pages 610–612, Los Alamitos, USA, 1994.

[72] T. H. Cormen, C. E. Leiserson, R. L. Rivest, and C. Stein. *Introduction to Algorithms.* MIT Press/McGraw-Hill, 1990.

[73] R. H. Davies. *Learning Shape: Optimal Models for Analysing Shape Variability.* PhD thesis, University of Manchester, 2002.

[74] R. H. Davies, T. F. Cootes, and C. J. Taylor. A minimum description length approach to statistical shape modelling. In *Proc. Information Processing in Medical Imaging*, volume 2082, pages 50–63, 2001.

[75] R. H. Davies, T. F. Cootes, C. J. Twining, and C. J. Taylor. An information theoretic approach to statistical shape modelling. In *Proc. British Machine Vision Conference*, pages 3–11, 2001.

[76] R. H. Davies, C. J. Twining, T. F. Cootes, J. C. Waterton, and C. J. Taylor. 3D statistical shape models using direct optimisation of description length. In *Proc. ECCV*, volume 2352, pages 3–20. Springer, 2002.

[77] R. H. Davies, C. J. Twining, T. F. Cootes, J. C. Waterton, and C. J. Taylor. A minimum description length approach to statistical shape modeling. *IEEE Transactions on Medical Imaging*, 21(5):525–537, 2002.

[78] J. Davison. Modelling the human ear. Master's thesis, Department of Computer Science, University of Sheffield, 2003.

[79] H. Delingette. *Modélisation, Déformation et Reconnaissance d'Objets Tridimensionnels á l'Aide de Maillages Simplexes.* PhD thesis, L'École Centrale de Paris, 1994.

[80] E. W. Dijkstra. A note on two problems in connection with graphs. *Numerische Math.*, 1:269–271, 1959.

[81] G. Djupesland and J. J. Zwislocki. Sound pressure distribution in the outer ear. *Scan. Audiol.*, 1(4):197–203, 1972.

[82] M. P. do Carmo. *Differential Geometry of Curves and Surfaces.* Prentice-Hall, Inc, Englewood Cliffs, New Jersey, 1976.

[83] I. L. Dryden and K. V. Mardia. *Statistical Shape Analysis.* Wiley, Chichester, 1997.

[84] A. Dubb, B. Avants, R. Gur, and J. Gee. Shape characterization of the corpus callosum in schizophrenia using template deformation. In *Proc. Medical Image Computing and Computer-Assisted Intervention*, volume 2, pages 381–388, 2002.

[85] N. Duta, M. Sonka, and A. K. Jain. Learning shape models from examples using automatic shape clustering and procrustes analysis. In *Proc. Information Processing in Medical Imaging*, pages 370–375, 1999.

[86] G. J. Edwards, T. F. Cootes, and C. J. Taylor. Advances in active appearance models. In *Proc. Int. Conf. on Computer Vision*, pages 137–142, 1999.

[87] D. W. Eggert, A. Lorusso, and R. B. Fisher. Estimating 3D rigid body transformations: a comparison of four major algorithms. *Mach. Vis. and Applic.*, 9:272–290, 1997.

[88] D. P. Egolf, D. K. Nelson, H. C. Howell III, and V. D. Larson. Quantifying ear-canal geometry with multi computer-assisted tomographic scans. *J. Acoust. Soc. Am.*, 93(5):2809–2819, 1993.

[89] J. Ehrhardt, H. Handels, B. Strathmann, T. Malina, W. Plötz, and S. J. Pöppl. Atlas-based recognition of anatomical structures and landmarks to support the virtual three-dimensional planning of hip operations. In *Proc. of Medical Image Computing and Computer Assisted Intervention*, volume 2878, pages 17–24. Springer-Verlag, 2003.

[90] H. Eiriksson. Shape represenation, alignment and decomposition. Master's thesis, Informatics and Mathematical Modelling, Technical University of Denmark, Lyngby, 2001.

[91] D. Eppstein. Asymptotic speed-ups in constructive solid geometry. Technical Report 92-87, Univ. of California, Irvine, Dept. of Information and Computer Science, Irvine, CA, 92697-3425, USA, 1992.

[92] A. Ericsson. Automatic shape modelling and applications in medical imaging. Licentiate thesis, Centre for Mathematical Sciences, Lund University, 2004.

[93] A. Ericsson and K. Åström. Minimizing the description length using steepest descent. In *Proc. British Machine Vision Conference*, pages 93–102, 2003.

[94] J. Feldmar and N. Ayache. Rigid, affine and locally affine registration of free-form surfaces. *International Journal of Computer Vision*, 18(2):99–119, 1996.

[95] J. Feldmar, J. Declerck, G. Malandain, and N. Ayache. Extension of the ICP algorithm to nonrigid intensity-based registration of 3D volumes. *Computer Vision and Image Understanding*, 66(2):193–206, 1997.

[96] R. Fisker. *Making Deformable Template Models Operational.* PhD thesis, Department of Mathematical Modelling, Technical University of Denmark, Lyngby, 2000.

[97] P. T. Fletcher, S. Joshi, C. Lu, and S. Pizer. Gaussian distributions on Lie groups and their application to statistical shape analysis. In *Proc. Information Processing in Medical Imaging*, volume 2732 of *LNCS*, pages 450–462, 2003.

[98] M. Fleute and S. Lavallee. Building a complete surface model from sparse data using statistical shape models: application to computer assisted knee surgery. In *Proc. Medical Image Computing and Computer-Assisted Intervention*, pages 879–887. Springer-Verlag, 1998.

[99] J. Foley, A. van Dam, S. Feiner, and J. Hughes. *Computer Graphics Principles and Practice.* Addison-Wesley, Reading, Massachusetts, 1990.

[100] M. Forsyth. Shelling and offsetting bodies. In *Proc. ACM Symposium on Solid Modeling*, page 373, 1995.

[101] A. F. Frangi, D. Rueckert, J. A. Schnabel, and W. J. Niessen. Automatic construction of multiple-object three-dimensional statistical shape models: Application to cardiac modeling. *IEEE Transactions on Medical Imaging*, 21(9):1151–1166, 2002.

[102] H. Fuchs, Z. M. Kedem, and B. F. Naylor. On visible surface generation by a priori tree structures. In *Proc. SIGGRAPH*, volume 14, pages 124–133, 1980.

[103] S. Gallot, D. Hulin, and J. Lafontaine. *Riemannian Geometry.* Springer-Verlag, 2 edition, 1993.

[104] H. Garcia. *Peritympanic versus deep or "CIC" positioning.* The Science of Hearing. Philips Hearing Instruments, 1994.

[105] H. Garcia and W. Staab. Solving challenges in deep canal fittings, part I. *The Hearing Review*, 2(1):34–49, 1995.

[106] D. Geman. Random fields and inverse problems in imaging. In *Saint-Flour lectures 1988*, Lecture Notes in Mathematics, pages 113–193. Springer-Verlag, 1990.

[107] S. Geman and D. Geman. Stochastic relaxation, Gibbs distributions, and the Bayesian restoration of images. *IEEE Transactions on Pattern Analysis and Machine Intelligence*, 6(6):721–741, November 1984.

[108] G. Gerig, M. Styner, D. Jones, D. Weinberger, and J. Lieberman. Shape analysis of brain ventricles using SPHARM. In *Proc. Workshop on Mathematical Methods in Biomedical Image Analysis*, pages 171–178, 2001.

[109] G. Gerig, M. Styner, M. E. Shenton, and J. A. Lieberman. Shape verus size: Improved understanding of the morphology of brain structures. In *Proc. MICCAI*, volume 2208 of *LNCS*, pages 24–32, 2001.

[110] B. van Ginneken, A. F. Frangi, J. J. Staal, B. M. Ter Haar Romeny, and M. A. Viergever. Active shape model segmentation with optimal features. *IEEE Transactions on Medical Imaging*, 21(8):924–933, 2002.

[111] C. Goodall. Procrustes methods in the statistical analysis of shape. *Jour. Royal Statistical Society, Series B*, 53:285–339, 1991.

[112] S. Gottschalk, M. C. Lin, and D. Manocha. OBBTree: A hierarchical structure for rapid interference detection. *Computer Graphics*, 30(Annual Conference Series):171–180, 1996.

[113] J. C. Gower. Generalized Procrustes analysis. *Psychometrika*, 40:33–51, 1975.

[114] S. Granger and X. Pennec. Multi-scale EM-ICP: a fast and robust approach for surface registration. In *Proc. European Conference on Computer Vision. Part IV*, volume 2353, pages 418–432. Springer-Verlag, 2002.

[115] P. Graversen. 3-Dimensional shape modelling. With application to human ear canals. Master's thesis, Informatics and Mathematical Modelling, Technical University of Denmark, DTU, Kgs. Lyngby, 2004.

[116] M. J. Grenness, J. Osborn, and W. L. Weller. Mapping ear canal movement using area-based surface matching. *J. Accoust. Soc. Am.*, 111(2):960–971, 2002.

[117] G. I. Gudmundsen. Physical options for custom hearing aids. *Seminars in Hearing*, 24(4):313–321, 2003.

[118] A. Guèziec. "Meshsweeper": Dynamic point-to-polygonal mesh distance and applications. *IEEE Transactions on Visualization and Computer Graphics*, 7(1):47–60, 2001.

[119] S. Haker, S. Angenent, A. Tannenbaum, and R. Kikinis. Nondistorting flattening maps and the 3D visualization of colon CT images. *IEEE Trans. on Medical Imaging*, 19(7):665–670, July 2000.

[120] S. Haker, S. Angenent, A. Tannenbaum, R. Kikinis, G. Sapiro, and M. Halle. Conformal surface parameterization for texture mapping. *IEEE Trans. on Visualization and Computer Graphics*, 6(2):1–9, April–June 2000.

[121] P. Hammond, T. J. Hutton, J. A. Allanson, A. Shaw, and M. A. Patton. 3D digital stereophotogrammetric analysis of Noonan syndrome. In *Proc. British Human Genetics Conference*, 2002.

[122] P. Hammond, T. J. Hutton, J. A. Allanson, and A. C. M. Smith. The 3D face of Smith-Magenis syndrome (SMS): a study using dense surface models. In *Proc. European Human Genetics Conference*, 2003.

[123] T. Hastie, R. Tibshirani, and J. Friedman. *The Elements of Statistical Learning.* Springer-Verlag, 2001.

[124] M. Held, J. T. Klosowski, and J. S. B. Mitchell. Collision detection for fly-throughs in virtual environments. In *Proc. symposium on Computational geometry*, pages 513–514, 1996.

[125] K. B. Hilger. *Exploratory Analysis of Multivariate Data.* PhD thesis, Informatics and Mathematical Modelling, Technical University of Denmark, DTU, Richard Petersens Plads, Building 321, DK-2800 Kgs. Lyngby, 2001.

[126] K. B. Hilger, R. Larsen, and M. Wrobel. Growth modeling of human mandibles using non-Euclidean metrics. *Medical Image Analysis*, 7:425–433, 2003.

[127] K. B. Hilger, R. R. Paulsen, and R. Larsen. Markov random field restoration of point correspondences for active shape modelling. In *Proc. SPIE - Medical Imaging*, 2004.

[128] A. Hill, A. D. Brett, and C. J. Taylor. Automatic landmark identification using a new method of non-rigid correspondence. In *Proc. Information Processing in Medical Imaging*, pages 483–488, 1997.

[129] A. Hill, C. J. Taylor, and A. D. Brett. A framework for automatic landmark identification using a new method of nonrigid correspondence. *IEEE Transactions on Pattern Analysis and Machine Intelligence*, 22(3):241–251, 2000.

[130] D. L. G. Hill, P. G. Batchelor, M. Holden, and D. J. Hawkes. Medical image registration. *Physics in Medicine and Biology*, 46(3):1–45, 2001.

[131] H. Hoppe. *Surface reconstruction from unorganized points.* PhD thesis, University of Washington, Department of Computer Science and Engineering, June 1994.

[132] E. Hopper and B. Turton. Application of genetic algorithms to packing problems — a review. In P. K. Chawdry and R. K. Kant, editors, *Proc. On-line World Conference on Soft Computing in Engineering Design and Manufacturing*, pages 279–288. Springer Verlag, 1997.

[133] B. K. P. Horn. Closed form solution of absolute orientation using unit quaternions. *Journal of the Optical Society A*, 4(4):629–642, 1987.

[134] B. K. P. Horn, H. M. Hilden, and S. Negahdaripour. Closed-form solution of absolute orientation using orthonormal matrices. *Journal of the Optical Society of America A (Optics and Image Science)*, 5(7):1127–1135, 1988.

[135] J. L. Horn. A rationale and test for the number of factors in factor analysis. *Psychometrika*, 30:179–186, 1965.

[136] P. M. Hubbard. Constructive solid geometry for triangulated polyhedra. Technical Report CS-90-07, Brown University, Dept. of Computer Science, Providence, Rhode Island 02912, September 1 1990.

[137] P. M. Hubbard. Collision detection for interactive graphics applications. *IEEE Trans. Visualization and Computer Graphics*, 1(3):218–230, September 1995.

[138] P. M. Hubbard. Approximating polyhedra with spheres for time-critical collision detection. *ACM Transactions on Graphics*, 15(3):179–210, July 1996.

[139] P. M. Hubbard. Improving accuracy in a robust algorithm for three-Dimensional Voronoi diagrams. *Journal of Graphics Tools*, 1(1):33–45, 1996.

[140] T. J. R. Hughes. *The Finite Element Method.* Dover Publications, Inc., New York, USA, 2000.

[141] E. G. Huot, H. M. Yahia, I. Cohen, and I. Herlin. Surface matching with large deformations and arbitrary topology: A geodesic distance evolution scheme on a 3-manifold. In *Proc. ECCV (1)*, pages 769–783, 2000.

[142] M. K. Hurdal, P. L. Bowers, K. Stephenson, D. W. L. Sumners, K. Rehm, K. Schaper, and D. A. Rottenberg. Quasi-conformally flat mapping the human cerebellum. In *Proc. Medical Image Computing and Computer-Assisted Intervention*, LNCS, pages 279–286. Springer, 1999.

[143] T. J. Hutton, B. F. Buxton, and P. Hammond. Dense surface point distribution models of the human face. In *Proc. Workshop on Mathematical Methods in Biomedical Image Analysis*, pages 153–160, 2001.

[144] T. J. Hutton, B. F. Buxton, and P. Hammond. Estimating average growth trajectories in shape-space using kernel smoothing. In *Proc. Int. Workshop on Growth and Motion in 3D Medical Images, European Conference on Computer Vision*, pages 1–7, 2002.

[145] T. J. Hutton, B. F. Buxton, and P. Hammond. Automated registration of 3D faces using dense surface models. In *Proc. British Machine Vision Conference*, pages 439–448, 2003.

[146] T. J. Hutton, B. F. Buxton, P. Hammond, and H. W. W. Potts. Estimating average growth trajectories in shape-space using kernel smoothing. *IEEE Transactions on Medical Imaging*, 22(6):747–753, 2003.

[147] I. Ikonen, W. E. Biles, A. K., J. C. Wissel, and R. K. Ragade. Genetic Algorithm for Packing Three-Dimensional Non-Convex Objects Having Cavities and Holes. In *Proc. Int. Conf. on Genetic Algortithms*, pages 591–598, East Lansing, Michigan, 1997. Morgan Kaufmann Publishers.

[148] Sonic Innovations. Conforma 2 se. redefining what a hearing aid is and who wears them, 2001.

[149] J. E. Jackson. *A User's guide to Principal Components*. Wiley, 1991.

[150] A. K. Jain, Y. Zhong, and M.-P. Dubuisson-Jolly. Deformable template models: A review. *Signal Processing*, 71(2):109–129, 1998.

[151] A. K. Jain., Y. Zhong, and S. Lakshmanan. Object matching using deformable templates. *IEEE Trans. on Pattern Analysis and Machine Intelligence*, 18(3):267–278, 1996.

[152] P. A. Johansen. Measurement of the human ear canal. *Acustica*, 33:349–351, 1975.

[153] C. E. Johnson and J. L. Danhauer. CIC instruments: Cosmetic issues. In M. Chasin, editor, *CIC Handbook*, pages 151–168. Singular Publishing Group, Inc., 1997.

[154] R. A. Johnson and D. W. Wichern. *Applied Multivariate Statistical Analysis*. Prentice-Hall, 1982.

[155] S. Joshi, S. M. Pizer, P. T. Fletcher, A. Thall, and G. Tracton. Multi-scale 3-D deformable model segmentation based on medial description. In *Proc. Information Processing in Medical Imaging*, volume 2082 of *LNCS*, pages 64–77, 2001.

[156] T. Kanai, H. Suzuki, and F. Kimura. Metamorphosis of arbitrary triangular meshes. *IEEE Computer Graphics and Applications*, 20(2):62–75, 2000.

[157] M. Kass, A. Witkin, and D. Terzopoulos. Snakes: Active contour models. *Int. Jour. of Computer Vision*, 8(2):321–331, 1988.

[158] M. R. Kaus, V. Pekar, C. Lorenz, R. Truyen, S. Lobregt, and J. Weese. Automated 3-D PDM construction from segmented images using deformable models. *IEEE Transactions on Medical Imaging*, 22(8):1005–1013, 2003.

[159] A. Kelemen, G. Székely, and G. Gerig. Elastic model-based segmentation of 3D neuroradiological sets. *IEEE Trans. Med. Imaging*, 18:828–839, 1999.

[160] A. R. Kildeby. Building optimal 3D shape models. Master's thesis, Informatics and Mathematical Modelling, Technical University of Denmark, DTU, 2002.

[161] M. C. Killion, L. A. Wilber, and G. I. Gudmundsen. Zwislocki was right...a potential solution for the 'hollow voice' problem (the amplified occlusion effect) with deeply sealed earmolds. *Hearing Instruments*, 39(1):14–18, 1988.

[162] Y. J. Kim, M. A. Otaduy, M. C. Lin, and D. Manocha. Fast penetration depth computation for physically-based animation. In *Proc. ACM Symposium on Computer Animation*, 2002.

[163] R. Kimmel and J. A. Sethian. Computing geodesic paths on manifolds. *Proc. of the National Academy of Sciences of the USA - Paper Edition*, 95(15):8431–8435, 1998.

[164] S. Kirkpatrick, C. D. Gelatt Jr., and M. P. Vecchi. Optimization by simulated annealing. *Science*, 220(4598):671–680, May 1983.

[165] J. T. Klosowski. *Efficient Collision Detection for Interactive 3D Graphics and Virtual Environments.* PhD thesis, State University of New York at Stony Brook, May 1998.

[166] J. T. Klosowski, M. Held, J. S. B. Mitchell, H. Sowizral, and K. Zikan. Real-time collision detection for motion simulation within complex environments. In *Proc. SIGGRAPH*, 1996.

[167] J. T. Klosowski, M. Held, J. S. B. Mitchell, H. Sowizral, and K. Zikan. Efficient collision detection using bounding volume hierarchies of k-DOPs. *IEEE Transactions on Visualization and Computer Graphics*, 4(1), 1998.

[168] M. Kohnen, A. H. Mahnken, J. Kesten, E. Koeppel, R. W. Gunther, and B. B. Wein. A three dimensional knowledge based surface model for segmentation of organic structures. In *Proc. SPIE. Part I*, volume 4684, pages 485–494, 2002.

[169] A. C. W. Kotcheff and C. J. Taylor. Automatic construction of eigenshape models by direct optimization. *Medical Image Analysis*, 2(4):303–314, 1998.

[170] B. Krebs, P. Sieverding, and B. Korn. A fuzzy ICP algorithm for 3D free-form object recognition. *Proc. International Conference on Pattern Recognition. Part 1*, pages 539–543, 1996.

[171] D. H. Laidlaw, W. B. Trumbore, and J. F. Hughes. Constructive solid geometry for polyhedral objects. In *Proc. Siggraph*, pages 161–170, 1986.

[172] J. Lam and J-M. Delosme. Performance of a new annealing schedule. In *Proc. ACM/IEEE Design Automation Conference*, pages 306–311, 1988.

[173] R. Larsen. *Estimation of visual motion in image sequences.* PhD thesis, Department of Mathematical Modelling, Technical University of Denmark, 1994.

[174] R. Larsen. Shape modelling using maximum autocorrelation factors. In *Proc. of the Scandinavian Image Analysis Conference*, pages 98–103, 2001.

[175] R. Larsen. Decomposition using maximum autocorrelation factors. *Journal of Chemometrics*, 16(8–10):427–435, 2002.

[176] R. Larsen, H. Eiriksson, and M. B. Stegmann. Q-MAF shape decomposition. In *Proc. Medical Image Computing and Computer-Assisted Intervention*, volume 2208 of *LNCS*, pages 837–844. Springer, 2001.

[177] R. Larsen and K. B. Hilger. Probabilistic generative modelling. In *Proc. Scandinavian Conference on Image Analysis*, volume 2749 of *Lecture Notes in Computer Science*, pages 861–868. Springer, 2003.

[178] R. Larsen and K. B. Hilger. Statistical 2D and 3D shape analysis using non-Euclidean metrics. *Medical Image Analysis*, 7(4):417–423, 2003.

[179] R. Larsen, K. B. Hilger, K. Skoglund, S. Darkner, R. R. Paulsen, M. B. Stegmann, B. Lading, H. Thodberg, and H. Eiriksson. Some issues of biological shape modelling with applications. In *Proc. Scandinavian Conference on Image Analysis*, volume 2759 of *LNCS*, pages 509–519. Springer, 2003.

[180] R. Larsen, K. B. Hilger, and M. C. Wrobel. Statistical 2D and 3D shape analysis using non-Euclidean metrics. In *Proceedings of Medical Image Computing and Computer-Assisted Intervention*, volume 2489, pages 428–435. Springer-Verlag, 2002.

[181] M. Levoy, K. Pulli, B. Curless, S. Rusinkiewicz, D. Koller, L. Pereira, M. Ginzton, S. Anderson, J. Davis, J. Ginsberg, J. Shade, and D. Fulk. The digital michelangelo project: 3D scanning of large statues. In *Proc. SIGGRAPH*, pages 131–144, 2000.

[182] S. .Z. Li. *Markov Random Field Modeling in Image Analysis.* Springer-Verlag, 2001.

[183] W. E. Lorensen and H. E. Cline. Marching cubes: A high resolution 3D surface construction algorithm. *Computer Graphics (SIGGRAPH '87 Proceedings)*, 21(4):163–169, July 1987.

[184] C. Lorenz and N. Krahnstöver. Generation of point-based 3D statistical shape models for anatomical objects. *Computer Vision and Image Understanding*, 77(2):175–191, 2000.

[185] H. Luo and T. O'Donnell. A 3D statistical shape model for the left ventricle of the heart. In *Proc. Medical Image Computing and Computer-Assisted Intervention*, volume 2208 of *Lecture Notes in Computer Science.* Springer, 2001.

[186] J. B. A. Maintz and M. A. Viergever. A survey of medical image registration. *Medical Image Analysis*, 2(1):1–36, 1998.

[187] T. McInerney and D. Terzopoulos. Deformable models in medical image analysis: a survey. *Medical Image Analysis*, 2(1):91–108, 1996.

[188] D. Meagher. Geometric modeling using octree encoding. *Computer Graphics and Image Processing*, 19(2):129–147, 1982.

[189] V. Milenkovic. Rotational polygon containment and minimum enclosure using only robust 2D constructions. *Computational Geometry*, 13(1):3–19, 1999.

[190] B. Moore, M. Stone, and J. Alcantara. Technical review of the songbird disposable hearing aid. Technical report, University of Cambridge, 2001.

[191] H. G. Mueller. CIC hearing aids: What is their impact on the occlusion effect? *The Hearing Journal*, 47(11):29–35, 1994.

[192] D. Nain. An interactive virtual endoscopy tool with automatic path generation. Master's thesis, MIT AI Lab, May 2002.

[193] D. Nain, S. Haker, R. Kikinis, and E. Grimson. An interactive virtual endoscopy tool. In *Proceedings of Interactive Medical Image Visualization and Analysis at MICCAI*, 2001.

[194] M. Nielsen, P. Johansen, A. D. Jackson, and B. Lautrup. Brownian warps: A least committed prior for non-rigid registration. In *Medical Image Computing and Computer-Assisted Intervention*, volume 2489, pages 557–564. Springer, 2002.

[195] R. J. Oliveira. The active ear canal. *J. Am. Acad. Audiol.*, 8:401–410, 1997.

[196] R. J. Oliveira and G. Hoeker. Ear canal anatomy and activity. *Seminars in Hearing*, 24(4):265–275, 2003.

[197] T. Osogami. Approaches to 3D free-form cutting and packing problems and their applications: A survey.

[198] J. Ousterhout. *Tcl and the Tk Toolkit.* Addison-Wesley, May 1994.

[199] R. R. Paulsen and K. B. Hilger. Shape modelling using Markov random field restoration of point correspondences. In *Proc. Information Processing in Medical Imaging*, volume 2732 of *Lecture Notes in Computer Science*, pages 1–12. Springer-Verlag, 2003.

[200] R. R. Paulsen, R. Larsen, B. K. Ersbøll, C. Nielsen, and S. Laugesen. Testing for gender related size and shape differences of the human ear canal using statistical methods. In *Proc. Eleventh International Workshop on Matrices and Statistics*, Informatics and Mathematical Modelling, Technical University of Denmark, 2002.

[201] R. R. Paulsen, R. Larsen, S. Laugesen, C. Nielsen, and B. K. Ersbøll. Building and testing a statistical shape model of the human ear canal. In *Proc. Medical Image Computing and Computer-Assisted Intervention*, volume 2489 of *Lecture Notes in Computer Science*, pages 373–380. Springer-Verlag, 2002.

[202] R. R. Paulsen, C. Nielsen, S. Laugesen, and R. Larsen. Using a shape model in the design of hearing aids. In *Proc. SPIE - Medical Imaging*, 2004.

[203] B. A. Payne and A. W. Toga. Distance field manipulation of surface models. *Computer Graphics and Applications*, 12(1), 1992.

[204] A. Perrie and H. Arndt. Engineering issues with CIC hearing aids : One manufacturer's view. In M. Chasin, editor, *CIC Handbook*, pages 137–149. Singular Publishing Group, Inc., 1997.

[205] C. Z. Pirzanski. Diminishing the occlusion effect: Clinician/manufacturer-related factors. *Hearing Journal*, 51(4):66–78, 1998.

[206] C. Z. Pirzanski. Ear impressions for the new laser shell technology. *Seminars in Hearing*, 24(4):323–332, 2003.

[207] S. M. Pizer, A. Thall, and D. Chen. M-Reps: A new object representation for graphics. Technical report, University of North Carolina at Chapel Hill, 1999.

[208] W. H. Press, B. P. Flannery, S. A. Teukolsky, and W. T. Vetterling. *Numerical Recipes: The Art of Scientific Computing.* Cambridge University Press, Cambridge (UK) and New York, 2nd edition, 1992.

[209] M. Quicken, C. Brechbühler, J. Hug, H. Blattmann, and G. Székely. Parameterization of closed surfaces for parametric surface description. In *Proc. Computer Vision and Pattern Recognition*, pages 354–360, 2000.

[210] Raindrop Geomagic. eShell, 2002.

[211] M. Rogers and J. Graham. Robust active shape model search. In *Proc. European Conference on Computer Vision. Part IV*, volume 2353 of *LNCS*, pages 517–530. Springer-Verlag, 2002.

[212] S. Romdhani, S. Gong, and A. Psarrou. A multi-view nonlinear active shape model using kernel pca. In *Proc. British Machine Vision Conference. Part 2*, pages 483–492, 1999.

[213] D. Rueckert, A. F. Frangi, and J. A. Schnabel. Automatic construction of 3-D statistical deformation models of the brain using nonrigid registration. *IEEE Transactions on Medical Imaging*, 22(8):1014–1025, 2003.

[214] S. Rusinkiewicz and M. Levoy. Efficient variants of the ICP algorithm. *Proc. Int. Conf. 3-D Digital Imaging and Modeling*, pages 145–152, 2001.

[215] S. Sachdev, C. J. J. Paredis, S. K. Gupta, and S. N. Talukdar. 3D spatial layouts using a-teams. In *Proc. ASME Design Engineering Technical Conference*. ASME, September 1998.

[216] Y. Sakurai, H. Suzuki, T. Kanai, and F. Kimura. Shelling operation for triangular mesh by vertex offsetting. *Journal of the Japan Society of Precision Engineering/Seimitsu Kogaku Kaishi*, 64(6):835–839, June 1998.

[217] F. Salvinelli, M. Maurizi, S. Calamita, L. D'Alatari, A. Capelli, and A. Carbone. The external ear and the tympanic membrane. *Scan. Adiol.*, 20:253–256, 1991.

[218] P. T. Sander and S. W. Zucker. Inferring surface trace and differential structure from 3-D images. *IEEE Transactions on Pattern Analysis and Machine Intelligence*, 12(9):833–854, 1990.

[219] W. J. Schroeder, K. Martin, and W. E. Lorensen. *The Visualization Toolkit: An Object-Oriented Approach to 3D Graphics.* Prentice Hall, December 1997.

[220] W. J. Schroeder, J. A. Zarge, and W. E. Lorensen. Decimation of triangle meshes. *Computer Graphics*, 26(2):65–70, 1992.

[221] M. Sermesant, C. Forest, X. Pennec, H. Delingette, and N. Ayache. Deformable biomechanical models: Application to 4d cardiac image analysis. *Medical Image Analysis*, 7(4):475–488, 2003.

[222] J. A. Sethian. *Level Set Methods and Fast Marching Methods: Evolving Interfaces in Computational Geometry, Fluid Mechanics, Computer Vision, and Materials Science.* Cambridge University Press, 1999.

[223] J. A. Sethian and A. Vladimirsky. Fast methods for the Eikonal and related Hamilton-Jacobi equations on unstructured meshes. *Proc. of the National Academy of Sciences of the USA*, 97(11):5699–5703, 2000.

[224] D. Sheehy, C. Armstrong, and D. Robinson. Shape description by medial axis construction. *IEEE Transactions on Visualization and Computer Graphics*, 2(1):62–72, 1996.

[225] K. Shimada, J. Cagan, and S. Yin. Geometric representations for intersection detection in intelligent packaging. Technical report, Carnegie Mellon University, 1998.

[226] K. Skoglund. Three-Dimensional face modelling and analysis. Master's thesis, Informatics and Mathematical Modelling, Technical University of Denmark, 2003.

[227] G. Smelt, M. Hawke, and D. Proops. Anatomy of the external ear canal: a new technique for making impressions. *The Journal of Otolaryngology*, 17(5):249–253, 1988.

[228] P. D. Sozou, T. F. Cootes, C. J. Taylor, and E. C. Di Mauro. Non-linear generalization of point distribution models using polynomial regression. *Image and Vision Computing*, 13(5):451–457, 1995.

[229] W. J. Staab. Deep canal hearing aids. In M. Chasin, editor, *CIC Handbook*, pages 1–30. Singular Publishing Group, Inc., 1997.

[230] L. H. Staib and J. S. Duncan. Model-based deformable surface finding for medical images. *IEEE Trans. Medical Imaging*, 15(4):720–731, 1996.

[231] M. B. Stegmann. Active appearance models. theory, extensions and cases. Master's thesis, Informatics and Mathematical Modelling. Technical University of Denmark, 2000.

[232] M. B. Stegmann. *Generative Interpretation of Medical Images.* PhD thesis, Informatics and Mathematical Modelling. Technical University of Denmark, 2004.

[233] M. B. Stegmann, B. K. Ersbøll, and R. Larsen. FAME – a flexible appearance modelling environment. *IEEE Trans. on Medical Imaging*, 22(10):1319–1331, 2003.

[234] M. R. Stinson and B. W. Lawton. Specification of the geometry of the human ear canal for the prediction of sound-pressure level distribution. *J. Acoust. Soc. Am.*, 85(6):2492–2503, June 1989.

[235] M. Styner and G. Gerig. Medial models incorporating object variability for 3D shape analysis. In *Proc. Information Processing in Medical Imaging*, volume 2082 of *LNCS*, pages 502–516, 2001.

[236] M. Styner, G. Gerig, J. Lieberman, D. Jones, and D. Weinberger. Statistical shape analysis of neuroanatomical structures based on medial models. *Medical Image Analysis*, 7(3):207–220, 2003.

[237] V. A. Sujan and S. Dubowsky. A model-free algorithm for the packing of highly irregular shaped objects: with application to cz semiconductor manufacture.

[238] P. Switzer. Min/max autocorrelation factors for multivariate spatial imagery. In L. Billard, editor, *Computer Science and Statistics*, pages 13–16. Elsevier Science Publishers B.V. (North Holland), 1985.

[239] S. Szykman, J. Cagan, and P. Weisser. An integrated approach to optimal three dimensional layout and routing. *ASME Journal of Mechanical Design*, 120(3):510–512, January 1999.

[240] C-K. Tang and G. Medioni. Curvature-augmented tensor voting for shape inference from noisy 3D data. *IEEE Transactions on Pattern Analysis and Machine Intelligence*, 24(6):858–864, 2002.

[241] G. Taubin. Estimating the tensor of curvature of a surface from a polyhedral approximation. In *Proc. Int. Conf. Computer Vision*, pages 902–907, 1995.

[242] J-P. Thirion. The extremal mesh and the understanding of 3D surfaces. *International Journal of Computer Vision*, 19(2):115–128, 1996.

[243] H. H. Thodberg. Minimum description length shape and appearance models. In *Proc. Information Processing in Medical Imaging*, volume 2732 of *Lecture Notes In Computer Science*. Springer, 2003.

[244] H. H. Thodberg and H. Olafsdottir. Adding curvature to minimum description length shape models. In *Proc. British Machine Vision Conference*, 2003.

[245] H. H. Thodberg and A. Rosholm. Application of the active shape model in a commercial medical device for bone densitometry. *Image and Vision Computing*, 21(13-14):1155–1161, 2003.

[246] D. W. Thompson. *On Growth and Form.* Cambridge University Press, Cambridge, 1917.

[247] M. Thompson and A. W. Toga. A surface-based technique for warping Three-Dimensional images of the brain. *IEEE Transactions on Medical Imaging*, 15(4):402–417, August 1996.

[248] R. R. V. Vidal. *Applied simulated annealing*, volume 396. Springer Verlag, Berlin, 1993.

[249] T. C. Walden, B. E. Walden, J. A. Cook, and D. A. Preves. Fixed vs. custom prescriptions for precipitous hearing loss. In *Proc. Annual Convention of the American Academy of Audiology*, April 2001.

[250] M. W. Walker, L. Shao, and R. A. Volz. Estimating 3-D location parameters using dual number quaternions. *CVGIP: Image Understanding*, 54(3):358–367, 1991.

[251] Y. Wang, B. S. Peterson, and L. H. Staib. Shape-based 3D surface correspondance using geodesics and local geometry. *Computer Vision and Pattern Recognition*, 2:644–651, June 2000.

[252] B. Welch. *Practical Programming in Tcl and Tk. 3rd Ed.* Prentice Hall, 1999.

[253] G. Winkler. *Image Analysis, Random Fields and Markov Chain Monte Carlo Methods - A Mathematical Introduction*, volume 27 of *Applications of Mathematics*. Springer-Verlag, 2 edition, 2003.

[254] www.3Shape.com. Shelldesigner, 2003.

[255] www.damvig.com. Rapid prototyping, 2003.

[256] H. Yahia, E. Huot, I. Herlin, and I. Cohen. Geodesic distance evolution of surfaces: A new method for matching surfaces. In *Proc. CVPR (1)*, pages 1663–1668, 2000.

[257] S. M. Yamany and A. A. Farag. Free-form surface registration using surface signatures. In *Proc. ICCV (2)*, pages 1098–1104, 1999.

[258] P. Yiu. The uses of homogeneous barycentric coordinates in plane Euclidean geometry. *International Journal of Mathematical Education in Science and Technology*, 31(4):569–578, July 2000.

[259] W. A. Yost and D. W. Nielsen. *Fundamentals of hearing - an introduction.* Holt, Rinehart and Winston, 1977.

[260] P. Yushkevich, S. M. Pizer, S. Joshi, and J. S. Marron. Intuitive, localized analysis of shape variability. In *Proc. Information Processing in Medical Imaging*, volume 2082 of *LNCS*, pages 402–408, 2001.

[261] J. Zemplenyi, S. Gilman, and D. Dirks. Optical method for measurement of ear canal length. *J. Acoust. Soc. Am.*, 78(4):2146–2148, 1985.

[262] Z. Zhang. Iterative point matching for registration of free-form curves and surfaces. *International Journal of Computer Vision*, 13(2):119–152, 1994.

[263] H-K. Zhao, S. Osher, and R. Fedkiw. Fast surface reconstruction using the level set method. In *Proc. IEEE Workshop on Variational and Level Set Methods in Computer Vision*, 2003.